Grid-friendly photovoltaic systems via autonomous power reserve function

by

Silvanus Ashok D'silva

B.E., University of Mumbai, 2014

A THESIS

submitted in partial fulfillment of the requirements for the degree

MASTER OF SCIENCE

Mike Wiegers Department of Electrical and Computer Engineering
Carl R. Ice College of Engineering

KANSAS STATE UNIVERSITY
Manhattan, Kansas

2020

Approved by:

Co-Major Professor
Dr. Haitham Abu-Rub

Approved by:

Co-Major Professor
Dr. Mohammad B. Shadmand

Copyright

Abstract

The ever-increasing energy demand along with the depleting fossil fuel reserves and climate change has compelled the incorporation of renewables-based energy generation in the conventional power systems. Furthermore, the abundant availability of solar energy coupled with the rapid advances in photovoltaic (PV) technology and their low deployment and maintenance costs facilitate the large share of PV generated power amongst the total contribution from renewable generation. However, the intermittent nature of solar irradiation causes stability issues in the high PV penetrated grid. This limits the large-scale integration of PV sources in the power grid. A potential solution to address this issue is mitigation using energy storage systems. However, the downsides are the high cost, low reliability, and short lifetime of the currently available energy storage technologies. Another alternative to address these issues is by the implementation of clusters of PV sources interfaced to the grid and controlling them as a dispatchable generator via a microgrid (MG) framework. This minimizes the need of expensive energy storage systems for the mitigation of the power fluctuations and maintaining the grid stability. This thesis proposes an autonomous power reserve function (APRF) for the PV sources connected in a MG via a cluster architecture that enables grid friendly PV systems. The PV cluster architecture regulated by the APRF enables the mitigation of the source-side and the load side fluctuations experienced by the MG/ grid; thereby ensuring uninterrupted power fed to the local loads and a resilient operation of the entire system. The APRF regulates the operation set-point of the PV sources at a non-maximum power point and thus provides smooth PV power injection along with a dispatchable power reserve. Furthermore, this dispatchable reserve can be leveraged by the grid operator to maintain the voltage and frequency of the MG/grid in the event of a generation-demand imbalance. The proposed APRF functionality has been experimentally

validated in a hardware-in-the-loop environment followed by a hardware implementation on gallium nitrite (GaN) based dc-dc boost converter. Besides, the proposed control scheme has been further modified to ensure injection of PV power into the grid occurs at a regulated ramp rate. This facilitates the regulation of grid frequency in a high PV penetrated grid environment. The proposed APRF functionality for the PV clusters shall enable the transformation of PV sources into a grid –friendly renewable based green and clean power source for the future.

Table of Contents

List of Figures

List of Tables

Acknowledgements

I would like to thank my family and my fiancée whose constant support and unconditional love enabled me to attain this goal. I would also like to express my sincere gratitude to Dr. Mohammad B. Shadmand and Dr. Haitham Abu-Rub who were not only my co-advisors but also my mentors. It was their constant support, patience, wisdom, guidance and encouragement that helped me in the completion of this thesis successfully. Further, I would also like to extend my gratitude to all my friends from Manhattan, Kansas and my lab-mates for their wisdom, courage and positivity that helped me significantly during harsh times. Last but not the least, I would like to thank the Kansas State University's Mike Wiegers Electrical and Computer Engineering department for providing me with the required technical knowledge, lab infrastructure and other facilities and assistance whenever required.

Dedication

I dedicate this work to my beloved parents *Ashok* and *Elma*, my brother *Mac dada* and *Salomie*, and to all my friends. I could never make it this far without your love and support!

Chapter 1 - Introduction

1.1 Motivation

The ever-increasing global warming and climate change experienced around the world has ramped up the frequency and severity of the natural disasters at an alarming rate. In the year 2018, the United States suffered six weather related disasters including 4 severe storms and 2 winter storms, each incurring economic losses exceeding 1 billion dollars [1]. Consequently, the number of massive blackouts per year as experienced in 2000s have also increased ten-fold as compared to 1980-1990s. Fig. 1.1 below shows the ever-increasing trends in the number of natural disasters. These alarming figures have aroused an urgency to improve the resiliency of the conventional electric utility grid to faults. Accordingly, various government agencies around the world including the United States Department of Energy (US-DOE) has been taking keen interest to facilitate this transformation of the grid. Furthermore, the rapidly depleting fossil fuel reserves and ever-increasing energy demands of modern society have obliged the need to search

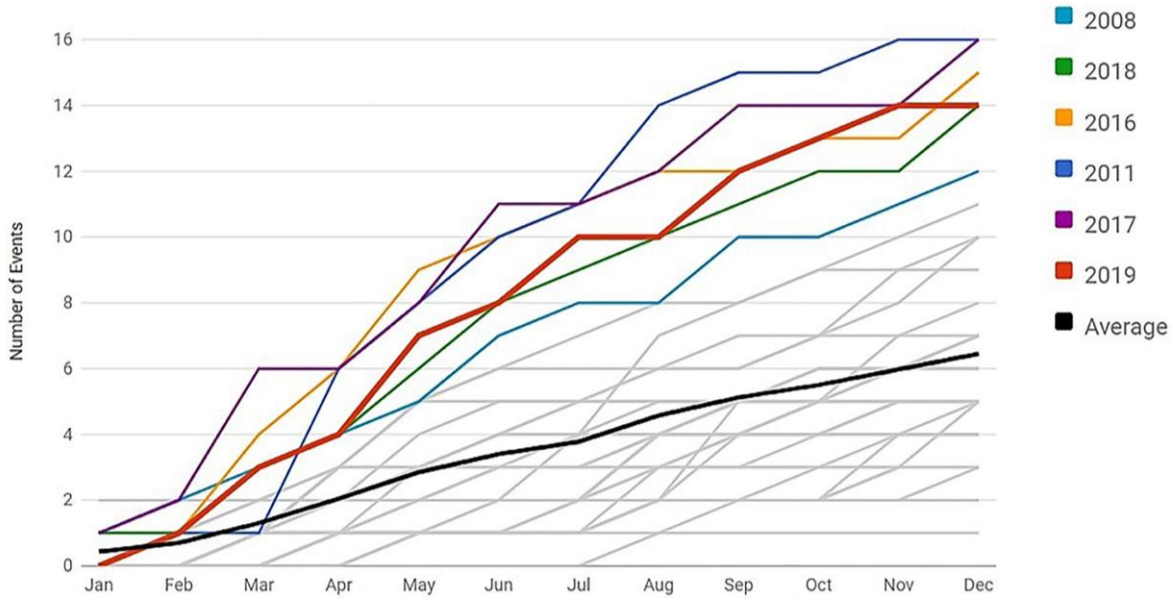

Fig. 1.1. 1980-2019 Year-to-Date U.S. Billion-Dollar disaster event frequency [1]

for non-conventional renewable based energy sources.

The abundant availability of solar energy and the ease in integrating photovoltaic (PV) sources into the utility grid seem to provide an ideal solution to address these crises. Moreover, the rapid enhancements in PV technology and their declining costs have boosted the deployment of PV based generation units in the utility grid. About 55% of the 178 gigawatts (GW) renewable energy installed in 2017 worldwide was generated from solar PV sources [1]. However, the variable PV ambient conditions introduce irregularities and random fluctuations in the PV system output power [2]. This in turn introduces high level of stochasticity in the power fed to the grid [3-5]. In a highly PV dominated grid [6], the intensity of these fluctuations can worsen and can drift the entire power system towards potential instability. A promising solution to minimize the impacts of these fluctuations is to interface the PV sources to the grid via microgrids (MG)s and regulate them as dispatchable generators (DG)s [6-8] as discussed in the later chapters.

1.2 Microgrid

MGs have attracted enormous attention in the past few decades due to their ability to provide uninterrupted power to local loads in the event of a grid fault [9, 10]. Besides, they offer easy integration to distributed energy resources (DER)s and possess the ability to accommodate high penetration of renewable energy sources (RES)s [11-13]. MGs are usually characterized by small energy generation and storage units located in close proximity of the loads [3, 6]. As per the definition adopted by the U.S. Department of Energy and several other European agencies, a MG refers to a cluster of interconnected critical and non-critical loads, DERs, and energy storage systems (ESS)s [14].

Recently, numerous government as well as third-party utility providers have been taking keen interest in the deployment of MGs in the conventional distribution networks due to the plethora of advantages that MGs offer [2, 8, 15, 16]. These include low distribution losses, higher energy utilization efficiencies, isolation of local loads during blackouts arising from grid faults, while also providing secondary features such as reactive power support and voltage-frequency (*V-f*) regulation to the grid [17-19]. MGs permit the inclusion of DERs in power generation under a regulated dispatch environment. The power generated by these DERs can be directly used by the local critical/non-critical loads or stored in ESSs .[20] This ensures the independent operation of the MG; thereby enhancing its resiliency to grid faults and power failures. Moreover, the integration of DERs offers a better economic welfare via demand peak shaving. Here, the generation cost is regulated by generating power from DERs during the peak load hours and maintaining standby generation to provide power support during extreme loading scenarios; thereby enhancing the MG's performance [21, 22].

1.2.1 Microgrid structure

Although the integration of DERs improves the grid resiliency to faults, a direct and unsupervised incorporation of a fleet of inverters into the power grid may compromise the grid stability [23]. This is peculiarly observed when their inverters' operating points fluctuate with the ambient conditions [24-26]. These stability issues can be mitigated by forming a grid of MGs and governing their operation using a hierarchical control and appropriate energy management schemes [26] as elaborated in the following chapters.

A typical MG configuration comprising of solar PV/wind based RESs, ESSs, critical and non-critical loads and a monitoring and control unit is shown in the Fig. 1.2. Here, the DERs have much smaller generation capacities then the conventional centralized power plants [22].

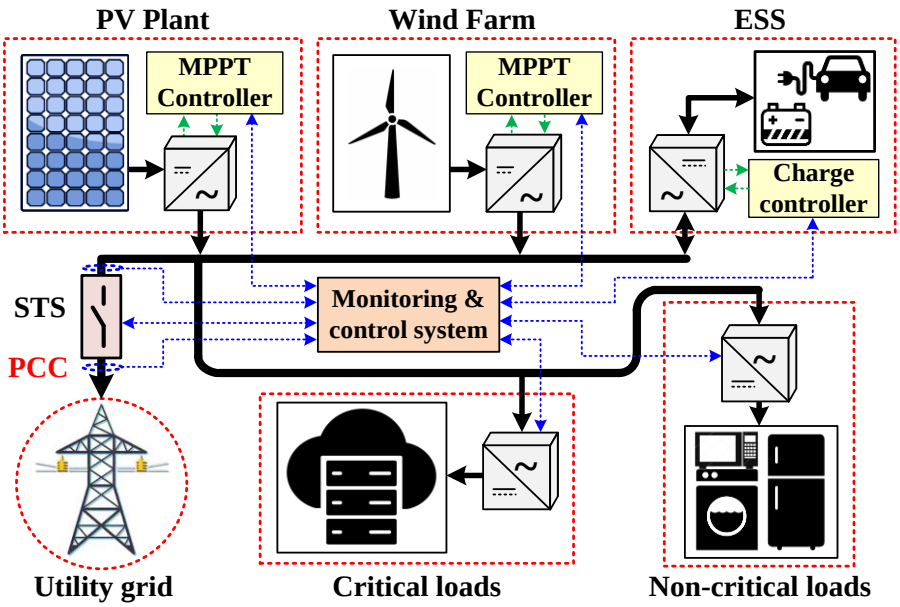

Fig. 1.2. A basic MG topology

The MG is connected to the utility grid through a single point of common coupling (PCC) which is realized by an electro-mechanical static transfer switch (STS) [27]. Under normal operation in the grid connected (GC) mode, the STS is in closed state and the MG is integrated in the utility grid. During a grid fault or intentional islanding scenario, the STS is opened and the MG transitions to islanded (IS) mode of operation. In this mode, the MG controller is solely responsible to ensure uninterrupted power to be available to all the local loads [8]. In the IS mode, if the load demand cannot be met by the total available generation, the MG controller needs to shed the non-critical load to maintain the system stability [28].

1.2.2 Distributed energy resources

Depending on their nature and dispatchability, DERs are usually categorized into two types as discussed below. The power output from ESS such as batteries, fuel cells, etc. can be precisely regulated and dispatched and hence they are categorized as dispatchable sources.

Conversely, the power output from PV and wind based renewable sources is intermittent and difficult to control and hence they are categorized as non-dispatchable sources [19, 26, 29, 30]. However, recent research trends are directed towards modifying the PV-based renewables into dispatchable sources as discussed in Chapter 3 and Chapter 4. These DERs are interfaced to the MG via converters/inverters depending on the dc or ac nature of both the interconnecting entities. The interconnecting converters/ inverters offer advantages such as high energy conversion efficiencies and power densities along with high controllability and assistance in providing ancillary services to the MG/grid [31].

1.2.3 Critical and non-critical loads

Depending on the system's priority, loads are classified as critical and non-critical loads [32]. Loads such as hospitals, data centers, telecommunication networks, essential emergency and backup services, etc. which need to be provided with uninterrupted power at all times are categorized as critical loads. A typical design of a MG is laid out such that the cumulative minimum generation from all the connected DERs should meet the total critical load in the MG at all times [32].

Non-critical loads include home appliances such as oven, washer, lighting etc. which may be disconnected for load shedding purposes in the event of a generation-demand mismatch.

1.3 Microgrid control

The main aim of any MG controller is to ensure that at any point within its physical boundaries, the voltage and frequency is regulated within the permissible limits. Besides it also needs to ensure that uninterrupted and secured power is supplied to its local loads at all times [33, 34]. If surplus power is available even after catering to the needs of all local loads and the

STS is in closed state (utility grid is not faulted), the excess power can then be exported to the grid. The other mandatory features of a MG control scheme are to achieve power balance and economic dispatch within the MG and ensure system stability, especially in the IS mode [33]. Accordingly, various controllers are developed by industrial vendors as per their client requirements. These controllers are typically based on one of the three types of MG control schemes as discussed below. They differ in terms of the topology of their controller implementation.

1.3.1 Decentralized control scheme

The decentralized control schemes are typically characterized by local controller (LC) units equipped with each interfaced DER. They are typically droop based control schemes [35] and the interconnected DERs are programmed to inject set amount of active/reactive power to the MG based on local *V-f* measurements. Their network topology is as shown in Fig. 1.3. Along with providing proportional active-reactive power sharing, these schemes do not require dedicated high bandwidth (BW) communication links for operation (except for synchronization

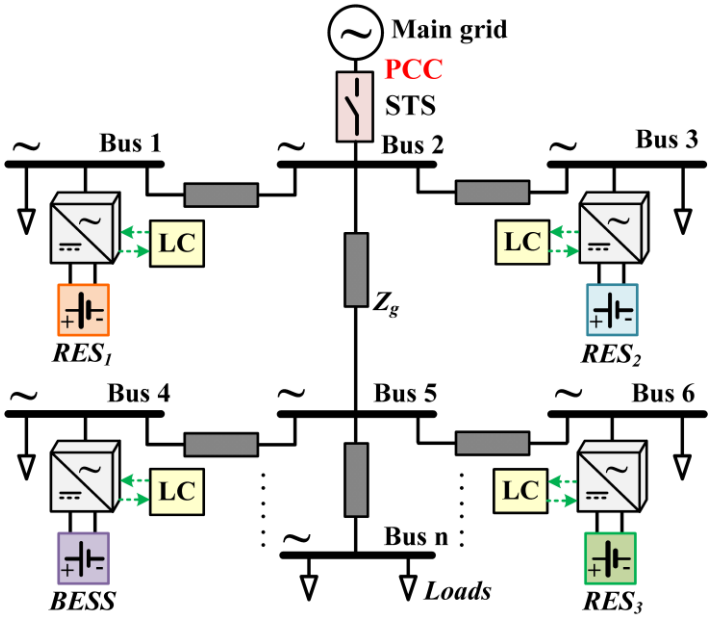

Fig. 1.3. Connection topology of decentralized control scheme for MGs

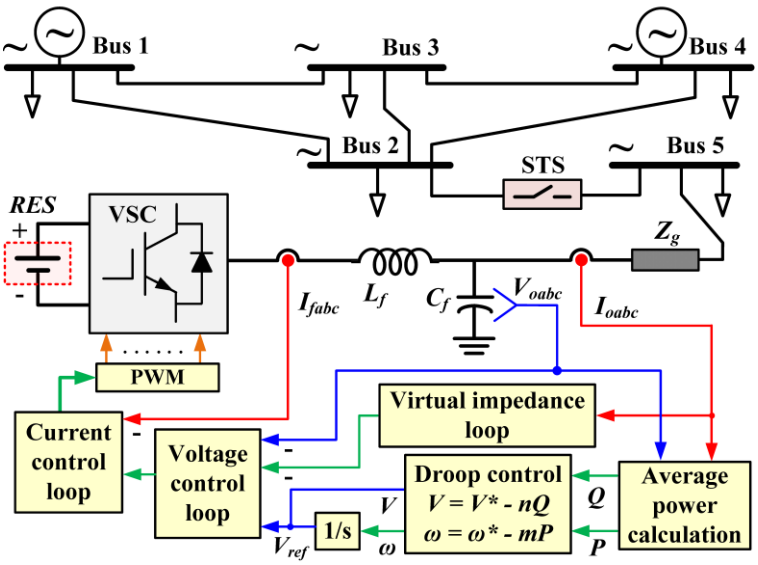

Fig. 1.4. A typical droop-controlled RES interfaced grid tied inverter

purposes) and can control MGs in GC, IS modes and during mode transitions. DERs maintain their operation set-point according to the droop provided power references in order to ensure active-reactive power sharing.

In [36], a decentralized droop-based strategy of two inverters in a MG using low BW communication has been proposed. Here, the MG's *V-f* at the PCC is regulated by adjusting the active and reactive power references for the two inverters. The proposed linear integration method uses minimal communication to exchange the power reference set points between the controllers and attains synchronization with the utility grid. A typical droop-controlled grid-tied inverter is as illustrated in Fig. 1.4. Its control consists of the inner voltage and current control loops and the outer droop (power) control loop. The droop equations that govern the operation of this scheme are discussed in detail in the next chapter.

1.3.2 Centralized control schemes

The centralized type of MG control scheme typically deploys hierarchical control architecture which have recently been standardized for MG control due to their advantages such as accurate power sharing, low voltage ride through capabilities, etc. as discussed in [37-40]. They distribute the control into three layers: primary, secondary and tertiary control. Each control layer is responsible for attaining specific targets and works with different execution rates [41]. The primary layer is implemented in the local controller (LC) as shown in Fig. 1.5. It regulates the voltage and frequency to the reference values and typically employs droop-based control. It is responsible for system reliability and stability, improving the system performance and ensuring efficient power sharing among the DERs [42-52].

Secondary control is centrally located in the microgrid central controller (MGCC) and is responsible for restoring the *V-f* deviations caused by the primary droop control. It also ensures the power quality and reliable operation of the MG and warrants uninterrupted voltage to the

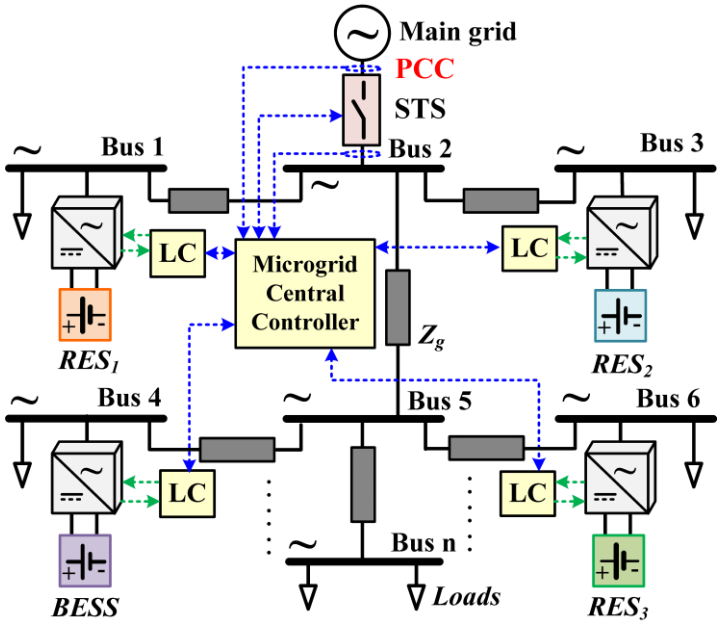

Fig. 1.5. Connection topology of centralized control scheme for MGs

local loads. Various centralized control approaches such as optimal dispatch [38], artificial neural network controllers and/or fuzzy logic controllers [53], model predictive controllers [17, 18] are deployed at this layer depending on the sizing and loading profiles of the MG.

The tertiary layer is the top-most layer and is located in the MGCC. It is responsible for improving the power quality of the high-level system through coordinating the operation of multiple MGs interacting with each other. It also controls the import/export of energy from/to other MGs and the grid. It exchanges information with the distribution system operator to make a feasible decision and optimize the MG operation with respect to the utility grid [54]. The tertiary layer can be implemented in a centralized as well as distributed architecture. The centralized architecture however strongly relies on fast communication between all interconnected units and requires strong coordination between the protection and control; which makes the controller design intricate [55]. This makes the system vulnerable to link failure issues and cyber-physical attacks [18]. In [56], an intrusion detection algorithm is proposed for centralized controller, which not only is capable of detecting possible intrusions, but also enables corrective actions during anomalies across the grid that increases the resiliency of the grid during cyber-physical attacks. To address these issues the distributed control has been proposed as discussed below.

1.3.3 Distributed control schemes

The distributed control schemes harness the advantages of decentralized and centralized control schemes by deploying a multiagent system (MAS) based approach [40, 41, 57, 58]. The MAS considers the DER units as different agents coordinated and synchronized through information exchange among them. The DER units require only peer-to-peer low bandwidth connections realized using sparse communication links as evident in the network topology illustrated in Fig. 1.6. Various distributed control schemes for MG control have been proposed in

literature [40, 57, 58]. In addition to the reduced communication dependency and improved resiliency, distributed control schemes also possess advanced features such as ability to eliminate the static errors that arise in droop based decentralized systems [57, 58].

In [58], a distributed control scheme for a MG is proposed where a distributed secondary control layer using a leader-follower consensus protocol and a tertiary mode supervisory control (MSC) are deployed. The primary control layer (which is droop based) and the secondary control layers are deployed on the LC of each connected DER. The MSC is placed around the STS and transmits compensation signals to only a few leader DERs located near the STS. They exchange these signals with all other connected DERs using the sparse communication network. In case, the power quality of the utility grid does not meet the operation criteria, the STS is opened and the MG transitions to IS mode. Distributed control schemes offer the most optimal performance for MG control in terms of high system reliability, flexibility and plug-and-play functionality for a practical MG. Besides, the distributed secondary control increases the system robustness to

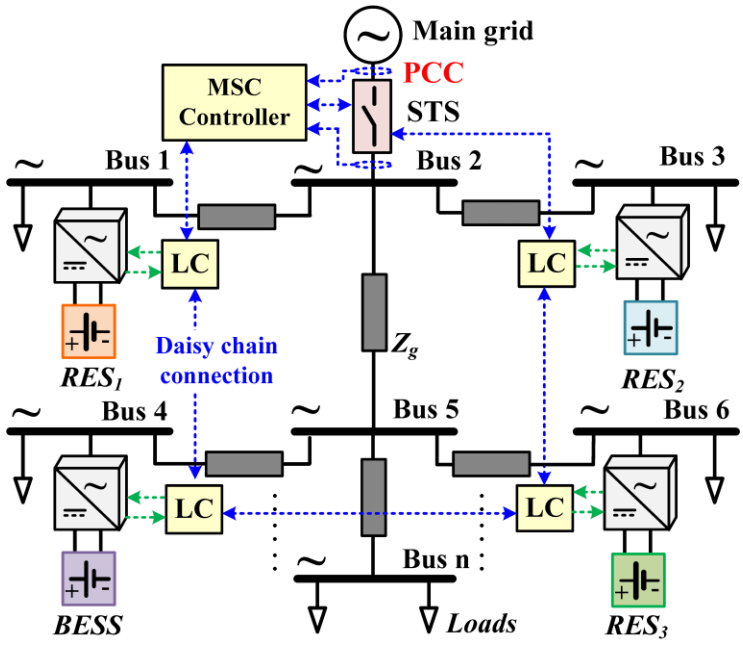

Fig. 1.6. Connection topology of distributed control scheme for MGs

single-point-of-failure issues to some extent. Furthermore, the communication complexity and burden on the higher-level control are also significantly reduced. In recent studies [59], the benefits of both distributed and centralized approaches are being employed to realize a better control bandwidth during anomalies across the grid, while guaranteeing optimal operation of the entire system.

1.4 Need for energy storage in microgrids

As discussed previously, ESSs are primarily deployed in a MG to store the excess power that is generated by the renewable based sources and provide a power backup whenever the renewable generation cannot meet the load demand [60, 61]. Moreover, ESSs also enhance the performance and stability of the MG by catering to the fluctuating load demands and enabling the DERs to run at constant power output [22]. Furthermore, they act as temporary power storage to yield and compensate for the power loss/abundance in the MG under intermittent solar irradiation conditions. Thus, integrating ESSs such as Battery energy storage systems (BESS)s, fuel cells (FC)s, super conducting magnetic energy storages (SMES) and ultra-capacitors (UC)s in the PV systems can mitigate the power fluctuations caused by the solar irradiation variations or load transients [62-64].

However, this is not an optimal economical solution considering the associated high operation and maintenance costs. Furthermore, mitigating all categories of short- and long-term transients via ESSs causes repetitive charge/discharge cycles and a significant reduction in the capacity as well as lifespan of the ESS [65]. Therefore, it is necessary to prevent the ESSs from these fast charge/discharge cycles that are caused by the sudden PV power and load transients [20]. Accordingly, the central ESS is typically utilized only for handling the long-term transients

[66]. This results in a reduced stress on the ESSs, leading to an extended lifetime [2]. An alternative solution to mitigate the short-term power transients is to regulate the PV sources as dispatchable generators as discussed below.

1.5 Photovoltaic clustering and power reserve

Clustering the PV sources within the MG is a potential solution to improve the controllability and situational awareness of a high PV penetrated grid [26, 67]. The short-term transients in the PV generated power can be mitigated using the PV power reserve implemented at the converter level in the PV clusters [15, 26]. Using the concept of constant power generation (CPG) [2], the neighboring PV sources within a PV cluster can harvest additional power and compensate for the power loss if required. Thus, using the PV power reserve, CPG enables harvesting and injection of regulated power into the grid, even under highly fluctuating PV ambient conditions. Consequently, the source side power fluctuations are mitigated successfully [16].

Moreover, this PV power reserve can be adaptively adjusted; based on grid operator command or other factors to provide voltage and frequency support to the MG/grid. These include dc bus voltage regulation in dc MGs and frequency regulation in ac MGs via power ramp rate control (PRRC) which are discussed later. The adjustable PV power reserve feature also plays a vital role in facilitating seamless transition of MG by providing the additional power required to maintain the voltage at PCC while transiting from GC to IS modes of operation. Thus, by leveraging the benefits of autonomous power reserve function (APRF), the PV systems can be made more grid-friendly while limiting the need of costly ESSs, which is the primary objective of this thesis.

1.6 Outline of thesis

This thesis is comprised of five chapters. Apart from this introductory chapter where the broad overview of MGs and its various components has been presented, Chapter 2 will provide an overview of the various MG control strategies proposed in literature for attaining seamless transition between GC and IS modes of operation. Further, it will present a proposed model predictive control (MPC) based inverter control strategy that is capable of attaining seamless transition between GC and IS modes. The discussion will be supported by results obtained through simulations of various test scenarios. This proposed inverter control will be later used for integrating the PV clusters to the MG/grid.

Chapter 3 will provide an in-depth explanation of the proposed power reserve control for PV clusters to mitigate the source side PV fluctuations. It will discuss the proposed PV cluster architecture, the control algorithm as well as the Typhoon hardware in the loop (HIL) based experimental results for various case scenarios. This will be followed by the experimental results that validate the practical implementation of the proposed APRF on a gallium nitrite (GaN) switch-based dc-dc converter.

Chapter 4 will further extend the idea of APRF to incorporate ramp rate control for PV clusters in a dc MG. The modified PV cluster architecture along with the control algorithm and the MATLAB simulation results that validate the system performance will also be discussed in this chapter.

Finally, Chapter 5 will present the concluding remarks about the proposed grid friendly PV cluster-MG architecture. It will also discuss the future work directed towards the implementation of a multi-tiered autonomous voltage-frequency control for a fleet of inverters in a power electronics dominated grid.

Chapter 2 - Seamless Transition in Microgrids

2.1 Inverters in microgrids

As mentioned previously, a MG consists of local loads and DERs placed in close proximity and regulated by a controller. Typically, the renewables based DER units are interfaced to the MG via power electronic converters (PEC)s. These PECs realized as inverters, interface the dc-natured renewable sources to the ac-natured MG [38, 68]. Under normal MG operations in GC mode, the inverters deliver maximum available power to the grid along with other ancillary services such as reactive power support [8]. Here, these inverters are configured to operate in current controlled mode (CCM) and they follow the voltage references at the point of common coupling (PCC). The MG's stability in this case is cohesively regulated by the various sources in the distribution network [69, 70].

2.2 Need for seamless transition

In the event of a grid fault, the fleet of inverters in the MG should disconnect as soon as the fault is detected. The fault detection intervals for inverters (and MG) corresponding to abnormal grid *V-f* conditions as discussed in [69] have been laid out by the IEEE 1547 [71] and IEC 61727 [72] standards. These times are documented in the Table 2.1 below. However, during these faults, the critical loads in the MG will also be disconnected from the utility grid. This will lead to interruption in their supplied power and thereby loss of load which is undesirable especially for critical loads. Hence, the main purpose of attaining seamless transition can be paraphrased as related to securing the critical loads with uninterruptible power which is typically drawn from the neighboring inverters during the transition process.

Table 2.1. *V-f* trip times specified in the IEEE 1547 and IEC 61727 standards [71, 72].

IEEE 1547		IEC 61727	
Voltage Range (% of base voltage)	Trip Time (sec)	Voltage Range (% of base voltage)	Trip time (sec)
V < 50	0.16	V < 50	0.10
50 ≤ V < 88	2.00	50 ≤ V < 85	2.00
110 < V < 120	1.00	110 < V < 135	2.00
V ≥ 120	0.16	V ≥ 135	0.05
Frequency Range (Hz)	Trip Time (sec)	Frequency Range (Hz)	Trip time (sec)
f < 59.3 or f > 60.5	0.16	f < 49 or f > 51	0.20

A potential solution to ensure uninterrupted energy services to critical loads in MGs during a grid fault is to seamlessly transit between GC and IS modes of operation while ensuring regulation of the PCC *V-f* by the inverters as discussed in [73]. In IS mode, the power converters transit to the grid forming voltage-controlled mode (VCM) and participate in catering the needs of the loads to maintain the *V-f* stability, when the STS is opened. This enables the connected MG to smoothly disconnect from the utility grid at the PCC and transit to IS mode of operation. This power support ensures immunity of the critical loads to power interruptions and grid faults caused during the event of natural disasters [74, 75].

2.3 Challenges in attaining seamless transition

The major challenges that arise in transition of a MG between GC and IS modes as discussed in [58, 76] include:

1. Frequency fluctuations leading to disturbance in the DER's power angle which affects the MG stability.

2. Large deviations in the DER interfaced inverter output voltage/current due to switching of its operation modes.

2.4 Classification of control schemes

To address these voltage and frequency fluctuations/deviations and thereby facilitate seamless transition, various control schemes have been proposed in literature. These schemes can be broadly classified into two types as:

1. Control schemes for individual inverters.
2. Control schemes for MGs.

For both applications, droop control-based control strategies are the most commonly used due to their advantages such as plug-n-play feature, communication-free power sharing and improved reliability. However, the traditional droop-based control schemes have some inherent limitations [58], such as:

1. *V-f* deviations observed in IS mode of operation.
2. Unregulated power injection in GC mode.
3. Inaccurate reactive power sharing in IS mode due to line impedance mismatch.
4. Need of a central synchronization unit before reconnection.

Various modified droop based and other ESS based and non-linear control schemes are proposed in literature to address these issues [11, 15, 35, 77-83].

2.5 Schemes for dual mode operation of inverters

Early research on seamless transition were done with the intention of seamlessly isolating individual inverters during a fault. A seamless transition control for a voltage controlled voltage

source inverter (VC-VSI) was introduced by Gao *et al.* in [84] where voltage and frequency regulation loops are implemented in the primary control that can operate in GC and IS modes and switch between these modes smoothly. This scheme however causes stability issues when implemented on multiple inverters due to lack of co-ordination between the neighboring units. In [85], a hysteresis-voltage control has been proposed which has been further enhanced by a sag-compensator based approach [86]. Here, the line interactive inverters provide uninterrupted power to local loads in the event of a grid fault. The proposed algorithm turns off the STS upon fault detection and monitors the load voltage's magnitude and phase to switch the inverter to VC-VSI mode as the switch current drops to zero. The drawback of this scheme is the large load voltage deviations observed due to current and load dependence, in addition to requirement of multiple sensors. A transition strategy involving load shedding to recover the inverter voltage was suggested by Balaguer *et al.* in [28]. However, it is found that the load voltage and grid current still have significant oscillations during the transition operation. Besides, this technique requires the disconnection of non-critical loads, which degrades the overall system capacity and reliability. In [76], a *dq*-based modified phase locked loop (PLL) is used to synchronize the load voltage's phase with that of the grid in the reconnection mode and to generate a phase of desired frequency in IS mode. Upon detection of a grid voltage sag, an operating sequence involving the PLL operation is initiated which enables the smooth transfer of the three phase GC inverter to IS mode. However, this technique suffers from sluggish response in addition to the need of two distinct controllers for each operation mode.

Another seamless transition strategy for a single phase grid interactive inverter has been proposed by Kim *et al.* in [87] where the voltage and current transients encountered during change of controller are reduced by regulating the inverter output current's peak value using the

inner voltage loop. The drawback of this method is that since the peak value of the filter inductor current determines the grid current reference, this reference can have inaccurate instantaneous value during the transition process. To address these drawbacks, Li *et al.* in [88] have proposed a controller with inner voltage-current control loops and external active-reactive power control loops along with additional synchronization control to attain smooth transition. Synchronization is achieved by adding two separate synchronization compensators to the real and reactive power control loops. The main drawback of this control scheme though, is that the dynamics of the power control are fixed by droop control and are not easily changeable. Besides, this system is highly susceptible to output short circuit and other network faults.

2.5.1 Using non-linear controllers

Recent trends in MG control with respect to seamless transition have been towards developing faster, advanced PLL or PLL-less solutions to attain grid synchronization. Also, special emphasis has been given on moving away from the conventional droop-based power sharing controls in the multi-agent DER environment. These include deployment of non-linear control schemes based on concepts such as self-synchronizing synchronverter [89], virtual synchronous generator [90], virtual oscillator control [57], etc. In [89], a self-synchronizing synchronverter has been proposed which does not need a dedicated synchronization unit. Synchronverters are inverters that mimic the response of synchronous generators and provide a mechanism for power systems to regulate renewable energy integration in the grid. They automatically synchronize with the grid prior to reconnection and track the grid frequency after transitioning to GC mode. However, this scheme requires an additional operation mode detection mechanism and has slower response due to synchronization delay. Besides, it has reactive power

imbalance issues when implemented on parallel inverters and hence does not support truly plug-n-play feature.

To address the above drawbacks, Ramezani *et al.* in [90] have modified the synchronverter control in [89] and proposed a hybrid controller for virtual synchronous generators. Here, an integrated virtual torque (VT) and virtual flux (VFL) linkage-based synchronization technique has been proposed that enables seamless transition between islanded and GC modes to provide a true plug-n-play functionality to the synchronverters. The VT term in the proposed control, minimizes the frequency/phase difference between the inverter output voltage and the ac bus/grid voltage by providing a synchronizing torque command 'T_{sync}' to the frequency control loop. This reduces the overshoots in the inverter output power during the transition process. Similarly, the load voltage amplitude is matched to the ac bus or the grid voltage amplitude by providing a synchronizing virtual flux command 'Ψ_{sync}' to the voltage control loop; thereby minimizing the overshoot in the output reactive powers. The set of VT and VFL relations for the transition from GC to IS mode of operation are given by (2.1) and (2.2).

$$T_{sync} = K_{\varphi}(\upsilon_{o_d}\upsilon_{b_q} - \upsilon_{b_d}\upsilon_{o_q}) = K_{\varphi}\left[-V_o V_b \sin(\delta_o - \delta_b)\right] \quad (2.1)$$

$$\psi_{\text{sync}} = K_{\psi}(\upsilon_{o_q} - \upsilon_{b_q}) = K_{\psi}\left[V_b - V_o \cos(\delta_o - \delta_b)\right] \quad (2.2)$$

Here, 'K_{φ}' and 'K_{Ψ}' represents the positive synchronizing VT and VFL gains respectively; while 'V_O' and 'V_b' are the inverter output voltage and ac bus voltage amplitudes. 'δ_O' and 'δ_b' are the ac-bus voltage phase and inverter output voltage phase respectively. The same set of synchronizing torque command 'T_{sync}' and flux command 'Ψ_{sync}' relations are applicable for the synchronverters' transition from IS to GC mode and given by (2.3) and (2.4).

$$T_{sync} = K_{\varphi}(\upsilon_{b_d}\upsilon_{g_q} - \upsilon_{b_q}\upsilon_{g_d}) = K_{\varphi}\left[-V_b V_g \sin(\delta_b - \delta_g)\right] \quad (2.3)$$

$$\psi_{\text{sync}} = K_{\psi}(\upsilon_{b_q} - \upsilon_{g_q}) = K_{\psi}\left[V_g - V_b \cos(\delta_b - \delta_g)\right] \quad (2.4)$$

Again here, 'K_φ' and 'K_Ψ' are the positive synchronizing VT and VFL gains respectively; while 'V_b' and 'V_g' are the ac bus voltage and grid voltage amplitudes respectively. 'δ_b' and 'δ_g' are the ac-bus voltage phase and grid phase respectively. The use of same set of governing relations for GC as well as IS operation modes eliminates the need of controller reconfiguration; thereby reducing the controller complexity.

2.5.2 Energy storage systems for assisting in seamless transition

Seamless transition techniques that use ESSs are also impressive alternatives and have gained popularity due to their ability to provide improved power backup, reliability and exceptional performance in MG operation [77-79]. These schemes typically follow a master-slave configuration. During GC operation, the inverters operate in CCM, regulating the grid injected current. In IS mode, the ESS interfaced inverter takes over as the master and operates in grid forming VCM while all other inverters are configured as slaves. This master unit is responsible for regulating the *V-f* at the PCC; while the other DER interfaced inverters continue to operate in grid feeding CCM thereby supplying constant P-Q with new *V-f* operating points obtained from the MG master [79, 91]. The drawbacks of these control schemes are that the master DER typically comprising of an ESS, should have higher capacity and power rating which increases its implementation and maintenance cost. Furthermore, all the transients observed in the MG need to be compensated by the master DER which increases its stresses thereby degrading its operational lifetime. Besides, a system failure of the master DER can cause the entire MG to shutdown [77].

Okui *et al*. in [78], has proposed a scheme for line-interactive uninterrupted power supply (UPS) systems to attain seamless transition using ESS. Here, the ESS interfaced converter along with a momentary abnormal voltage detection (MAVD) circuit helps in regulating the *V-f*

deviations across the local loads during a grid fault. Under a fault condition, the voltage and current control systems along with the MAVD and power failure detection circuit ensure that the power fed to the critical load remain regulated. In the initial stage, the power to the load is provided by the dc side capacitor in the power converter as far as the power fluctuations lie within the tolerance band. If the grid fault continues, the ESS's dc-dc converter will move into discharge mode and start feeding power to the load. Also, the voltage and current controllers detect the grid as soon as it becomes available and the input current is increased gradually so that the UPS system does not affect the dynamics of the diesel generator. However, here the UPS units are not analyzed for autonomous operation under parallel connection of multiple units.

The control schemes discussed so far consider the seamless transition only for an individual inverter level. However, in practice, MGs typically consist of multiple inverters connected at various buses. Hence, it is crucial to consider the interactions of the different inverter controllers to investigate seamless transition in MGs [80, 92, 93]. Besides, in a multi-agent environment of connected DERs, the *V-f* set-points of the MG are agreed upon by all the participating inverters following the droop control norms [69, 92]. During the transition of a MG, the voltage magnitude, frequency and power angle; defined by the power sharing between various DERs; undergo deviations. Thus, the seamless transition objectives cannot be achieved unless these magnitude and phase deviations are regulated within tolerable limits. The control schemes that offer seamless transition on a MG level are discussed in the following section.

2.6 Control schemes for dual mode operation of microgrids

Based on the classification of MG control schemes discussed in the previous chapter, the seamless transition strategies proposed in literature are also categorized as follows:

2.6.1 Decentralized control schemes

In [82], a decentralized control based approach is proposed where seamless transition is attained by regulating the '$V_i - \omega_i$' operating point for the i^{th} DER by adjusting its active power 'P_O' and reactive power 'Q_O' set point values in the droop relations given by (2.5) and (2.6) below.

$$\omega_i = \omega_O - m_i(P - P_O) \tag{2.5}$$

$$V_i = V_O - n_i(Q - Q_O) \tag{2.6}$$

Here, 'ω_O', 'V_O', 'P' and 'Q' represent the nominal frequency, nominal voltage, average active and reactive powers of the VSI based i^{th} DER respectively, while 'm_i' and 'n_i' are the droop co-efficients. Fig. 2.1(a). illustrates the deviation in 'ω' as the active power demand 'P_i' changes. Similarly, Fig. 2.1(b). illustrates deviation in grid voltage 'V' from 'V_1' (at no load) to 'V_2' with variations in reactive power 'Q_i' demand. However, to restore the MG V-f to attain seamless reconnection at other than the rated load conditions, this scheme has to drift the P and Q operating points from their nominal values; thereby resulting in power mismatches during reconnection [77]. This issue is addressed by various modified versions of droop control which

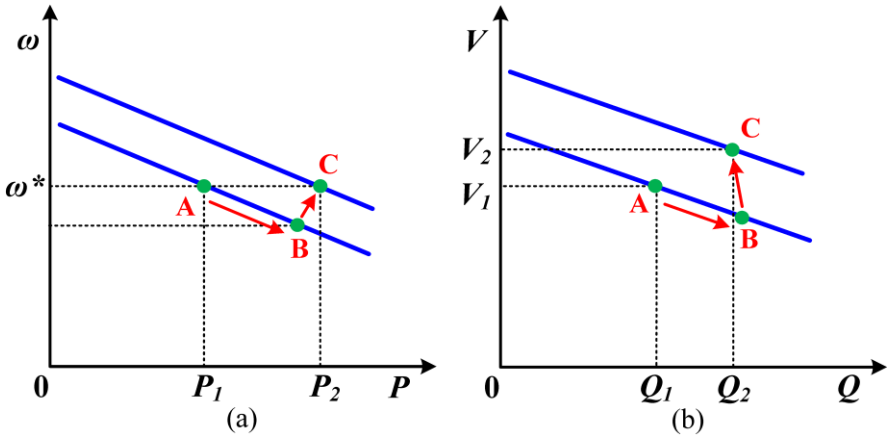

Fig. 2.1. (a) Increase in P causes drop in ω and (b) increase in Q causes drop in V; both compensated by droop control (operation at point C)

include electing one DER as a dispatch unit [11], implementing a double loop droop control [94] and a hybrid vector-control based scheme [36].

The highlighting feature of droop-based control lies in their low reliance on communication for synchronization which helps to mitigate the single point of failure issue. However, these schemes struggle to maintain a constant power flow in GC mode due to strong coupling between '$\omega - P$' and '$V - Q$' along with the grid *V-f* fluctuations. Besides, the droop control '$\omega - P$' and '$V - Q$' relations work efficiently in GC mode only when the X/R ratio of the distribution lines is much larger than 1. As the MG transits to IS mode, the X/R ratio of the interconnecting lines approaches less than or equal to unity. This significantly impacts the droop power sharing relations and increases the coupling between active and reactive power; thus degrading the performance of the droop based controllers. The authors of [80] have attempted to address these issues by proposing an enhanced power flow control (EPFC) scheme where the feedforward of grid frequency and voltage magnitude is used to mitigate the impacts of grid fluctuations on power flow. Also, a voltage magnitude control is proposed to improve the control accuracy. If the *V-f* magnitude exceeds the specified limits, the reference points obtained from the synchronous reference frame PLL are reverted to the original rated values 'ω_O' and 'E_O'; thus ensuring a smooth transition between the GC and IS modes. Another modified droop-based linear voltage compensator for power converters forming the MG, has been proposed in [30]. Here, the scheme includes (a) a voltage controller with capacitor current feedback input to the voltage controller and output current feedforward to input current control; (b) a modified droop control that emulates the inertia response of a synchronous generator. The additional capacitor current feedback in the voltage control loop provides additional damping needed to mitigate the

voltage deviations. Similarly, the output current feed-forward as input to the current controller helps to minimize the disturbances on the output voltage.

Despite all the above modifications, the droop control still needs time-scale separation from the voltage controllers by at least an order of magnitude; so as to maintain the system stability [57]. This makes the droop control inherently slow in response. Various control schemes for MG control that use non-linear control such as virtual oscillator control (VOC) [57] or those using dispatch units such as ESS [37, 77] provide solution to this problem and are discussed below. The authors of [77] have proposed a decentralized modified power control technique which uses an ESS to attain seamless transition. Here, the DER consisting of PV and battery ESS (BESS) acts as the MG master and controls the STS. Each residence has local loads and slave DERs consisting of local batteries interfaced via voltage source converters (VSC). When a grid fault occurs, the BESS governing master controller opens the STS and switches itself from power control mode (PCM) to VCM mode. In this mode, the master controller regulates the MG voltage at a reference amplitude and the grid reference frequency. The instantaneous reference phase angle value is obtained from the previous estimated value obtained in GC mode. Upon clearing the grid fault, the master controller resynchronizes the MG voltage with the grid voltage using the grid reference voltage. The reference voltage used by the master controller here is passed through a rate limiter to ensure a smooth transition. Finally, the master controller switches back to PCM and closes the STS to move the MG to GC mode. The limitation of this control scheme is that the capacity of the BESS interfaced to the master converter needs to be at least 150% of the average power demand of the MG [77] and thus leads to relatively expensive implementation. Besides, the batteries' limited lifecycles demand periodic replacements.

Another seamless non-linear scheme using a windowing factor-based approach for a

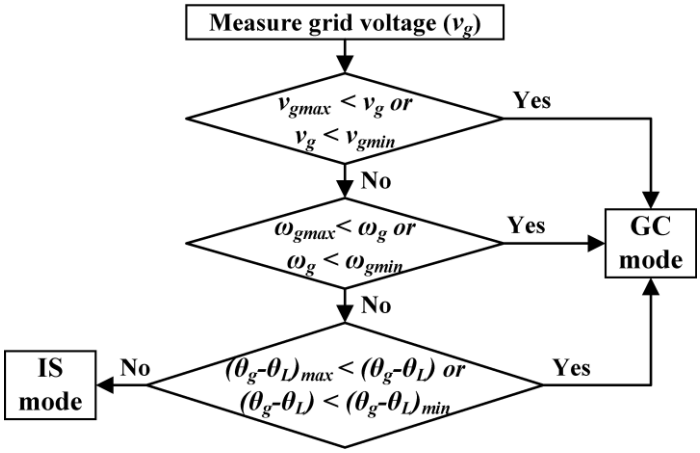

Fig. 2.2. Windowing factor-based grid synchronization control [37]

PV-BESS based MG has been proposed in [37]. It is used to estimate the phase and frequency of the utility grid. The windowing factor-based synchronization control estimates the values of load voltage phase 'θ_L' and grid voltage phase 'θ_g' simultaneously. Upon detection of grid fault, the STS is opened and the control of VSC switches from GC mode to IS mode. The process for re-synchronization involves detection of voltage amplitude, frequency and phase at the PCC to check if they lie in the desired operating range as illustrated in the flowchart in Fig. 2.2. The corresponding VSC parameters are then matched with that of the grid until the conditions are satisfied and the STS is closed. The VSC's controller then switches back to GC mode. The transfer function for voltage, frequency and phase estimation of sensed signal is given by (2.7) and (2.8).

$$\frac{\upsilon_{s\alpha}}{v_s} = \frac{[\omega_1(s)G_1 i_{L2}]/s}{1+[\omega_1(s)G_1 i_{L2}]/s} \tag{2.7}$$

$$\frac{\theta_g}{Input\ of\ \omega\ \text{sec}tion} = \frac{[\omega_2(s)G_2\omega_{r1}]/s + [\omega_3(s)G_3\omega_{r2}]/s}{1+[\omega_2(s)G_2\omega_{r1}]/s + [\omega_3(s)G_3\omega_{r2}]/s} \tag{2.8}$$

Here, '$\upsilon_{s\alpha}$' and 'v_s' are the estimated and the actual values of PCC voltage respectively. 'ω' and 'θ_g' are the estimated grid frequency and phase angle values while 'G_1', 'G_2' and 'G_3' are the set

gain values. '$\omega_1(s)$' is the window factor for voltage magnitude estimation while '$\omega_2(s)$' and '$\omega_3(s)$' are window factors for estimating the grid frequency and phase values. Appropriate values for window lengths and gains provide accurate estimation of grid *V-f* and phase. This scheme does not use PLL for synchronization and hence the frequency transients and phase jump issues dominant in PLL-based estimators are avoided [37]. However, the controller design is highly sensitive to the values of window factors and gains.

2.6.2 Centralized control schemes

In [69], a centralized control based seamless transfer strategy for a single-phase MG is presented. The MG consists of voltage controlled VSI (VC-VSI) and current controlled VSI (CC-VSI) working together; for both GC and IS modes of operation. The GC and IS operation mode control loops are combined into one droop-based control which forms the primary controller for each VC-VSI. This facilitates seamless transition since there is no need of changing the primary controllers. The secondary control is implemented on the MG central controller (MGCC) unit which acts as the central controller and has direct communication access to each inverter and STS. The STS monitors the *V-f* of the MG PCC voltage and the grid voltage and opens the switch if it finds irregularities in the grid voltage. It also transmits magnitude and frequency updates to MGCC periodically. Using these signals, the MGCC sends updated P-Q set points to all the inverters to regulate the MG's PCC voltage. The droop control functions that are used to realize this voltage regulation and to enable the inverter to operate in either modes of operation are given by (2.9) and (2.10) below.

$$\theta = \theta^* - (m_d + (m/s))(P - P^*) \tag{2.9}$$

$$V = V^* - (sn_d + n + (n_i / s))(Q - Q^*) \quad (2.10)$$

Where, $\theta^* = \omega^*/s$ is the output voltage phase angle, 'm' and 'n' are the $P-\omega$ and $Q-V$ droop gains respectively. 'P^*' and 'Q^*' are the inverter's real and reactive output power demands in GC mode. As the grid recovers, the STS updates the MGCC which in turns triggers the voltage and modified frequency restoration loops (including the grid synch block) to synchronize the MG voltage at the PCC with the grid voltage. A PLL is used to determine the *V-f* at the PCC. The grid synch block adds a frequency deviation term 'ω_{synch}' to the MG frequency to minimize the phase error between the grid voltage and the MG voltage and thereby facilitating a seamless reconnection to the grid. However, as discussed in the previous chapter the centralized control schemes suffers from the single point of failure issue, since the failure of the MGCC or any of the communication link(s) can cause the entire MG to collapse. Also, this scheme lays large computational burden on the MGCC which makes the design complex [39]. These issues are addressed by using distributed control schemes discussed below.

2.6.3 Distributed control schemes

Hou *et al*. in [58] proposed a distributed hierarchical control scheme that can provide seamless transition feature in ac MGs using a distributed secondary control layer based on a leader-follower consensus protocol and a tertiary mode supervisory control (MSC). The control of this scheme is discussed earlier in Chapter 1, Section 1.3.3. Here, when the grid fault is cleared, the MG *V-f* and phase need to be synced with that of the utility grid. Frequency synchronization is achieved using the '*P-ω*' droop relation given by (2.11).

$$\omega_i = \omega^* - m_i P_i + \Delta\omega_i \quad (2.11)$$

$$k_{\omega}\frac{d\,\Delta\omega_i}{dt} = \sum_{j\in N, j\neq i} a_{ij}(\Delta\omega_j - \Delta\omega_i) + \gamma_i(\Delta\omega^* - \Delta\omega_i) \tag{2.12}$$

The term '$\Delta\omega_i$' is the secondary control's frequency regulation term contributed to the primary droop control and is defined by (2.12). 'a_{ij}' indicates the existence of a data link connection between i^{th} and j^{th} DER and will be set to '1' if the link actually exists. If the link fails or the j^{th} DER is shut down, 'a_{ij}' will be set to '0' thereby making the contribution of the j^{th} DER in the frequency regulation process equal to zero. The term 'γ_i' is set to '1' if i^{th} DER is a leader; for all other i^{th} non-leader DERs this parameter is set to '0'. 'k_{ω}' is a positive control gain. The $P-\omega$ droop characteristics curve for the i^{th} DER is illustrated in Fig. 2.3(a). Similarly, the voltage synchronization is achieved using the $Q-V$ droop relation given by (2.13). The $Q-V$ droop characteristics curve is illustrated in Fig. 2.3(b).

$$V_i = V^* - n_i Q_i + \Delta V_i + \beta_i \Delta V^* \tag{2.13}$$

$$k_v\frac{d\,\Delta V_i}{dt} = \sum_{j\in N, j\neq i} b_{ij}(k_{Qj}Q_j - k_{Qi}Q_i) \tag{2.14}$$

Here, 'ΔV_i' is the secondary control's voltage regulation term defined in (2.14). Similar to (2.12), here 'b_{ij}' indicates the existence of a data link connection between the i^{th} and j^{th} DER

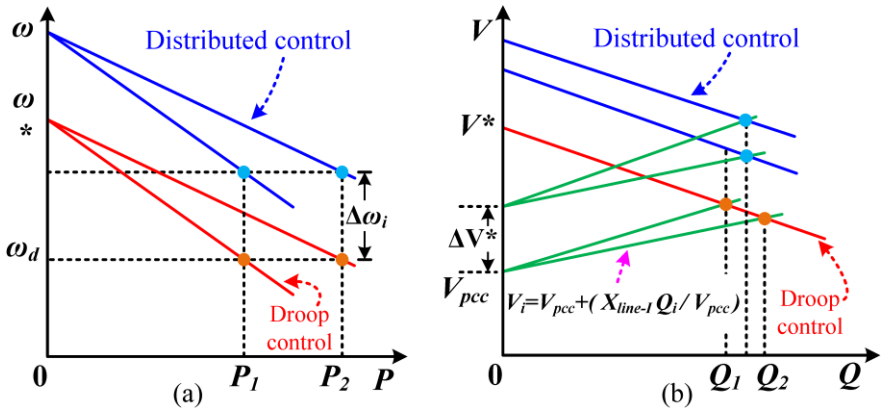

Fig. 2.3. Droop characteristics with *V-f* restoration loops (a) $P-\omega$ restoration and (b) Reactive power sharing with PCC voltage ($Q-V$) restoration

and will be set to '1' if the connection exists. If the link fails or the j^{th} DER is shut down, 'b_{ij}' will be set to '0' thereby neglecting the contribution of the j^{th} DER in the voltage regulation process. The term 'β_i' represents leader mode and is set to '1' if i^{th} DER is a leader and for all other non-leader DERs, this parameter is set to '0'. The terms 'ΔV^*' and '$\Delta\omega^*$' in (2.13) and (2.11) are the active synchronization compensation signals for the MG's PCC voltage amplitude and frequency respectively and are transmitted by the MSC to all the DERs. These compensation signals steer the *V*-ω operating point of all the connected DERs so as to match the MG's *V*-*f* with that of the utility grid. Once synchronization is successfully achieved, the STS is closed and the MG smoothly transitions into GC mode. The main advantage of using the MSC with spare communication is that the single point of failure issue is mitigated and features such as plug-n-play and link failure resiliency are appended in the MG control [38, 39].

In [79], a hierarchical distributed control-based scheme for a MG interfaced to a line interactive UPS system has been proposed. Under normal operation the STS is closed, and the UPS can export or import power from the grid to charge the batteries. The MSC that controls the STS, measures the power at PCC, gets updates about the batteries' State of charge (SoC) from the UPS system and sends droop regulated active-reactive power update commands to other DER units via a low bandwidth communication. When a grid fault occurs, the embedded anti-islanding control in each DER's controller sets their PCC *V*-*f* to an upper or lower limit. The MSC detects this operating point adjustment as a fault and opens the STS to transit into IS mode. It also sends a status update to all interconnected DER units. The UPS system regulates the MG voltage at the PCC according to the power references received from the MSC using the modified droop relations given by (2.15) and (2.16) below.

$$\omega = \omega_O^* - [k_\omega + k_{\omega\_I}/s](P - P^*) \tag{2.15}$$

$$V = V_O^* - [k_\alpha + k_{\alpha\_I}/s](Q - Q^*) \quad (2.16)$$

Here, '$\omega_O{}^*$', '$V_O{}^*$', 'k_ω' and 'k_α' are the nominal frequency and nominal voltage reference values, proportional frequency coefficient and proportional voltage drooping coefficients respectively. 'P^*' and 'Q^*'are the power flow controller active and reactive power references that are adjusted to ensure '$\omega - V$' regulation. Also, 'k_{ω_I}' and 'k_{α_I}' are the integral frequency and voltage drooping coefficient set to zero in IS mode and are used to ensure accurate power tracking in the GC mode. Finally, a hierarchical distributed control schemes for non-linear VOC based MG has been proposed in [57]. This VOC based control offers improved MG operation due to the fast convergence of the non-linear VOC based primary layer control. However, the fast variations in the local primary control can impact the overall stability of MG.

2.7 Proposed control for photovoltaic cluster interfacing inverter

Based on the above discussion, distributed control schemes seem to offer the most optimal performance for MG control due to their advantages such as improved *V-f* regulation, reduced computational burden and communication dependency, enhanced power sharing ability and improved resiliency to grid failures. Furthermore, the coordinated control between the primary-secondary layer and the centrally located tertiary layer facilitate the incorporation of advanced features such as seamless transition ability in the MG.

Accordingly, a distributed control architecture for the inverter that facilitates the realization of a PV cluster dominated MG is proposed in this chapter. Here, we focus on developing the lower layer controller for the PV cluster interfacing inverter. Consequently, a non-linear model predictive control (MPC) based approach has been chosen to design the

primary control layer of the inverter interfacing the PV cluster and the MG/grid. The secondary and tertiary layer controllers shall be discussed in the later chapters.

2.7.1 System description

The block diagram of the dual mode inverter with the MPC based controller is as shown in Fig. 2.4. The dc side of the inverter is connected to the dc bus of a PV cluster, modelled as a dc source. The ac side is connected to local load via a simple L filter and then to the ac grid via the STS at the PCC. Under normal operations when the STS is in closed state, the inverter is supposed to regulate the PV cluster active - reactive powers injected in or drawn from the grid.

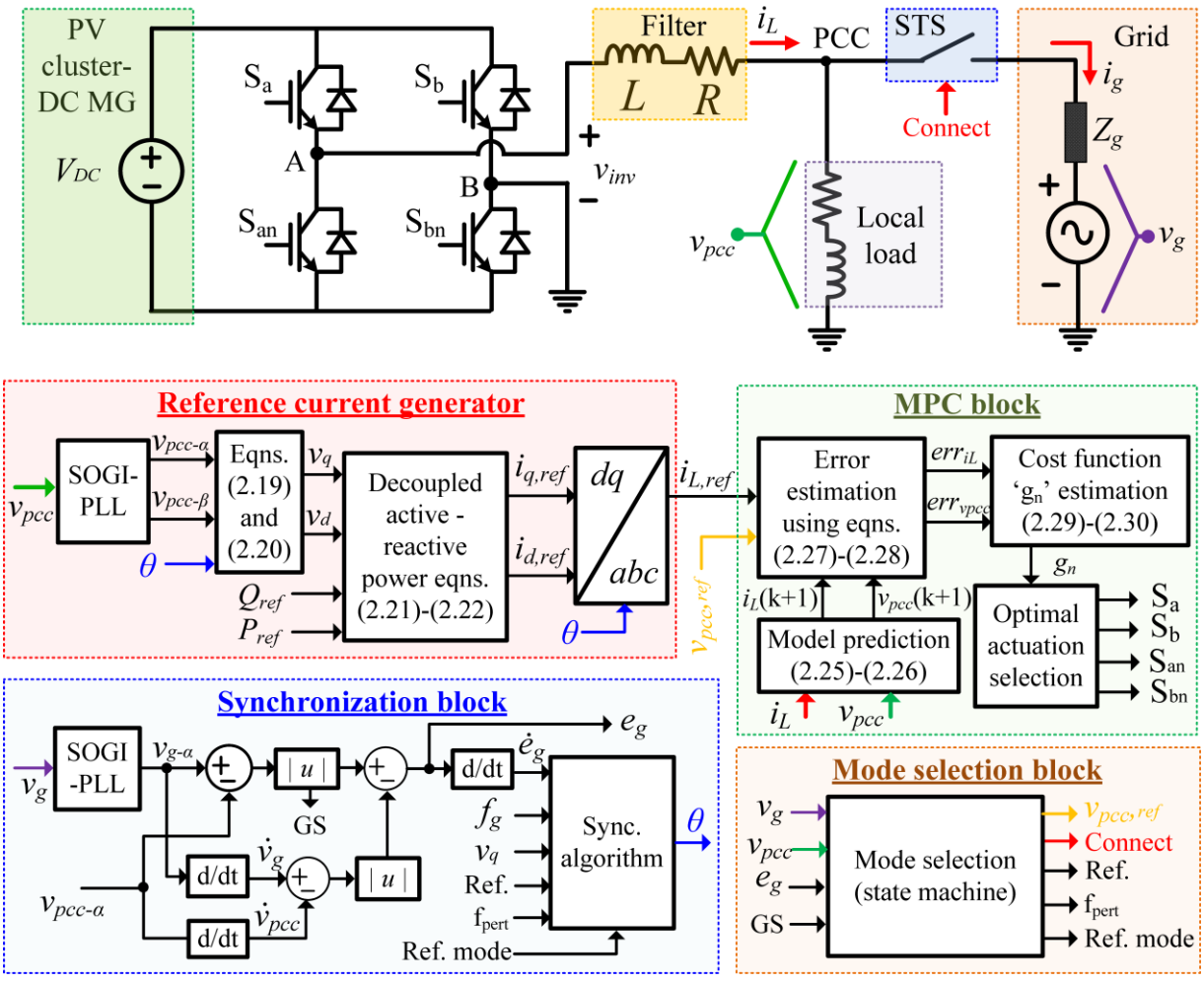

Fig. 2.4. Proposed MPC-based inverter control architecture

In the event of grid failure, the inverter should maintain the voltage across the local load. A second order generalized integrator (SOGI) based orthogonal signal generator (OSG) is used as a PLL to detect the phase and create orthogonal signals from the grid voltage 'v_g'. Due to the proven harmonic filtering capability of the SOGI PLL, the reference current obtained is robust to distorted grid condition which is typically the case in a highly PV penetrated grid [95].

2.7.2 Model predictive control formulation

The inverter reference current is constructed from the active and reactive power equations given by (2.17) and (2.18).

$$P[k] = \frac{1}{2}\{v_d[k]i_d[k]\} + \frac{1}{2}\{v_q[k]i_q[k]\} \tag{2.17}$$

$$Q[k] = \frac{1}{2}\{v_q[k]i_d[k]\} - \frac{1}{2}\{v_d[k]i_q[k]\} \tag{2.18}$$

Here, 'v_d' and 'v_q' are the *dq*-components of the inverter output voltage obtained from their respective $\alpha\beta$-components as (2.19) and (2.20). These orthogonal $\alpha\beta$-components of inverter output voltage 'v_{pcc}' are generated by the voltage SOGI block in the reference current generation block as shown in Fig. 2.4 above.

$$v_d[k] = v_{pcc-\alpha}\sin\theta - v_{pcc-\beta}\cos\theta \tag{2.19}$$

$$v_q[k] = v_{pcc-\alpha}\cos\theta + v_{pcc-\beta}\sin\theta \tag{2.20}$$

Further, the reference active power 'P_{ref}' and reactive power 'Q_{ref}' are coupled with these voltage components to obtain the inverter output reference current in the *dq*-frame; for each next sampling instance as (2.21) and (2.22) below.

$$i_{d,ref}[k+1] = \frac{2\left(P_{ref}v_d[k] + Q_{ref}v_q[k]\right)}{v_d[k]^2 + v_q[k]^2} \tag{2.21}$$

$$i_{q,ref}[k+1]=\frac{2\left(P_{ref}v_q[k]-Q_{ref}v_d[k]\right)}{v_d[k]^2+v_q[k]^2} \tag{2.22}$$

Here, 'i_{d_ref}' and 'i_{q_ref}' represent the *dq*-components of the inverter reference current. The current reference terms are then transformed using the inverse Park transformation to obtain (2.23).

$$i_{L,ref}[k] = i_{d,ref}[k]\sin\theta + i_{q,ref}[k]\cos\theta \tag{2.23}$$

In the GC mode, the grid reference current '$i_{L,ref}$' allows both active and reactive power to be regulated with a single term. In the above discussion, 'θ' is the reference phase angle obtained from the synchronization block. In IS mode, the synchronization block keeps monitoring the grid status 'GS' signal. As soon as the grid becomes available and its *V-f* are within the grid code limits ('GS' becomes high), the synchronization block initiates the synchronization process. Once the synchronization is successful, the synchronization block commands the STS to close and the inverter starts operating in GC mode, regulating the injected active and reactive powers. The 'P_{ref}' and 'Q_{ref}' power references can be adaptively adjusted by the grid operator depending on the severity of the voltage sags, inverter current ratings, local grid code demands, etc. [96].

The predictive model for the system is developed by applying Kirchoff's voltage law (KVL) in the output loop of the inverter consisting of the filter inductor 'L' with 'R' as its dc resistance and is given by (2.24).

$$v_{inv}[k] = R\,i_L[k] + L\frac{d}{dt}i_L[k] + v_{pcc}[k] \tag{2.24}$$

Now, using the Euler's forward approximation for differential terms, (2.24) can be used to determine the next state current at each sampling interval given by (2.25).

$$i_L[k+1] = \left[1 - \frac{R}{L}T_s\right] i_L[k] + \frac{T_s}{L}\left[v_{inv}[k] - v_{pcc}[k]\right] \quad (2.25)$$

Similarly, the next state output voltage is predicted using (2.25) and is given by (2.26).

$$v_{pcc}[k+1] = \frac{T_s}{C}\left[i_L[k+1] - i_L[k]\right] + v_{pcc}[k] \quad (2.26)$$

These predicted values of voltage and current are then used in minimization of the system cost function as discussed in the subsection 2.7.3.1.

2.7.3 Control strategy

The proposed control strategy for the PV cluster interfacing inverter consists of three main blocks: the MPC block responsible for generating the switching signals, the mode selection block that governs the inverter operation and the synchronization block that enables seamless reconnection with the grid. These blocks are discussed below.

2.7.3.1 Model predictive block

In this block, the MPC algorithm determines the most optimal switching configuration for minimizing the system cost function. The system cost function consists of various control objectives that need to be attained and are prioritized by corresponding weight factors. This formulated cost function is then subjected to minimization to determine the optimal switch actuation. The MPC algorithm determines the values of the system states namely, inductor current 'i_L' and output voltage 'v_{pcc}' using relations (2.23) and (2.24). Next, using (2.23) - (2.26), the state error functions 'err_{iL}' and 'err_{vpcc}' are determined as (2.27) and (2.28).

$$err_{iL}\left[k+1\right] = \left| i_{L,ref}[k+1] - i_L[k] \right| \quad (2.27)$$

$$err_{vpcc}\left[k+1\right] = \left| v_{inv,ref}[k+1] - v_{pcc}[k] \right| \quad (2.28)$$

The cost function 'g_n' subject to minimization is obtained as a linear summation of the state error functions scaled by their respective weight factors and is given by (2.29). The weight factors ('λ_{vO}' and 'λ_{iL}') take binary values as given by (2.30), depending on presence of the grid.

$$\min g_n = \lambda_{vpcc}\, err_{vpcc} + \lambda_{iL}\, err_{iL} \tag{2.29}$$

$$\lambda_{vpcc} = \begin{Bmatrix} 1 \;;\; \text{IS mode} \\ 0 \;;\; \text{GC mode} \end{Bmatrix} \quad \text{and} \quad \lambda_{iL} = \begin{Bmatrix} 0 \;;\; \text{IS mode} \\ 1 \;;\; \text{GC mode} \end{Bmatrix} \tag{2.30}$$

Accordingly, at each sampling instance the MPC algorithm estimates three vectors of cost 'g_n' namely, 'g_1', 'g_2' and 'g_3'. These vectors correspond to the three possible output voltage levels of the inverter's H-bridge, namely '$+V_{dc}$', '0', '$-V_{dc}$'. The actuation sequence corresponding to lowest cost vector as described in Table 2.2 below is applied to the gates of each switch in the H-bridge inverter.

2.7.3.2 Mode selection block

The proposed control scheme operates the single-phase dual mode H-bridge inverter in four operation modes; two steady state modes (GC and IS modes) and two transition modes (GC to IS mode and IS to GC mode). The modes of operation are observed by $\chi \in \{1-4\}$ where $\chi \in \{1\}$ and $\chi \in \{2\}$ represent the transition from GC to IS modes and IS to GC modes respectively. Further, $\chi \in \{3\}$ and $\chi \in \{4\}$ represent the GC mode and IS mode respectively.

In order to facilitate this transition, a state machine has been implemented with status indicators to indicate the operation state of the inverter. The flag 'χ' indicates the mode of the

Table 2.2. Switching sequence applied to inverter for optimum actuation

Condition	Switching sequence $[S_a\ S_{an}\ S_b\ S_{bn}]$
$g_1 < g_2$ and $g_1 < g_3$	[0 1 1 0]
$g_2 < g_1$ and $g_2 < g_3$	[0 0 0 0]
$g_3 < g_1$ and $g_3 < g_2$	[1 0 0 1]

inverter. Depending on the grid status 'GS',the '*Connect*' signal status and the value of the synchronization block error 'e_g', the system transits into one of the four states as illustrated in flowchart shown in Fig. 2.5. Here, under normal scenarios the grid *V-f* are within desired limits, synchronization error is within tolerance limit and hence STS is in closed state. So here $\chi \epsilon \{3\}$ and the inverter operates in GC mode thereby regulating injected active and reactive powers; set by the grid operator. In the event of a grid *V-f* imbalance the grid status signal 'GS' drops to 0, and inverter goes in the GC to IS transition mode ($\chi \epsilon \{1\}$) as the STS is opened. The inverter now transits into IS mode ($\chi \epsilon \{4\}$) and starts regulating the voltage across the local load. In this mode, the synchronization block keeps observing the grid status.

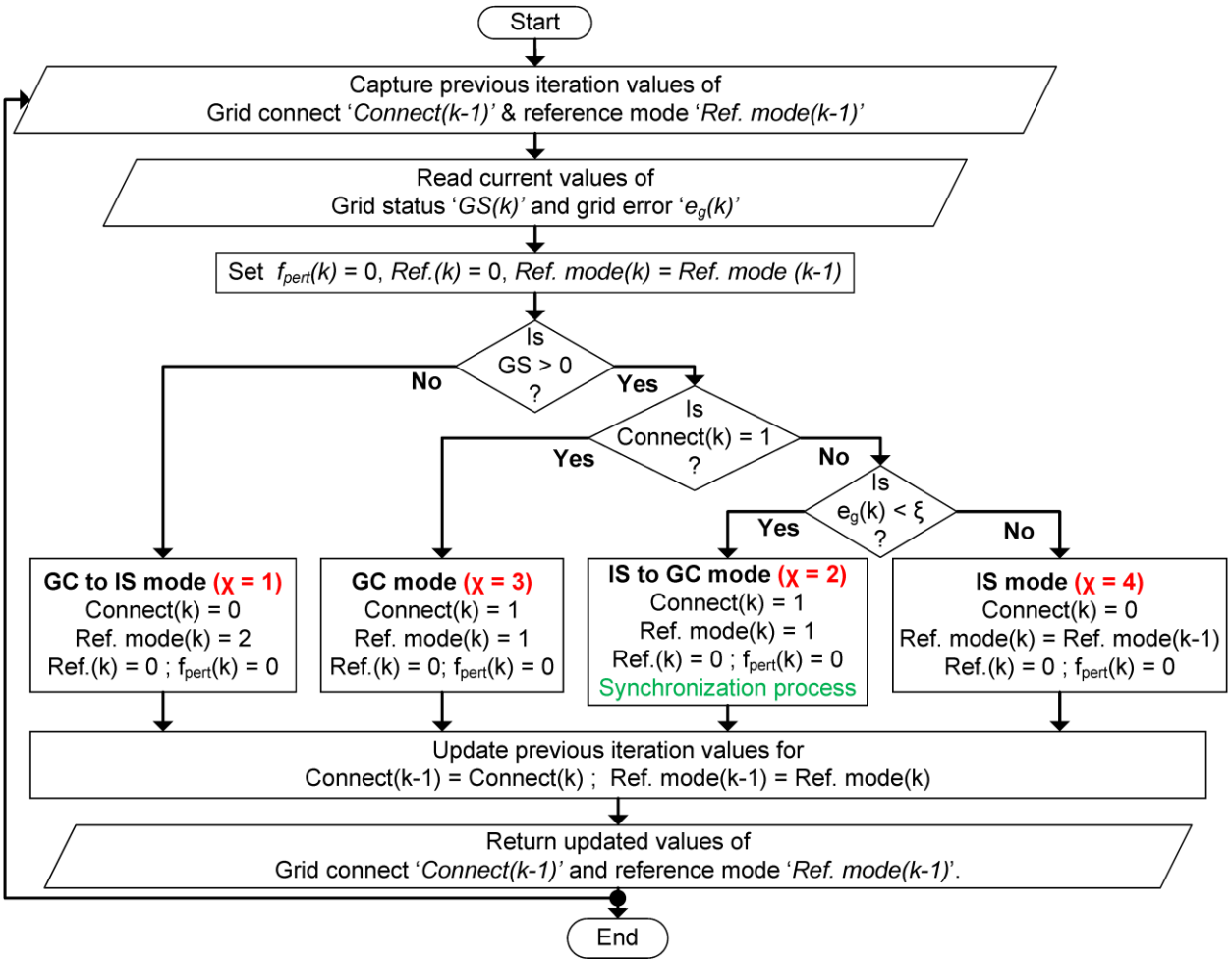

Fig. 2.5. Flowchart illustrating the mode transition of the MPC based inverter

As soon as the grid is restored and 'GS' becomes 1, the synchronization block starts tracking the grid error signal 'e_g' and synchronization is initiated. Now, $\chi \epsilon \{2\}$ and the synchronization block start adjusting the inverter output *V-f* to match with the grid and minimize the synchronization error. Once the error drops within the threshold value 'ξ', synchronization is achieved effectively, and the mode selection block makes the '*Connect*' signal high indicating the STS to close. Furthermore, it also commands the MPC block to transition the inverter operation to GC mode by changing the status of '*Ref. mode*' signal. Once the transition to GC mode is complete ($\chi \epsilon \{3\}$), the controller primarily emphasizes on tracking the reference active and reactive powers. As the inductor current error function given by (2.27) is driven towards zero, 'P_{ref}' and 'Q_{ref}' are tracked successfully by the inverter.

2.7.3.3 Synchronization block

As mentioned previously, the synchronization block keeps monitoring the grid status 'GS' signal. After the grid fault is cleared and as soon as 'GS' becomes high, the synchronization block starts dynamically adjusting the inverter output frequency around the nominal grid frequency 'f_g' to match its phase 'θ' with the grid phase 'θ_g'. The synchronization block uses the error 'e_g' between the grid voltage and inverter voltage along with its time derivative '$\dot{e}_g$' to determine the required shift in the inverter frequency.

During IS mode of operation, the inverter frequency is set to the desired nominal frequency of 60 Hz. Once 'GS' is high, if the synchronization block finds the error 'e_g' to be greater than the threshold 'ξ', it scales the current instance value of inverter output voltage's frequency by a factor of 0.95. This process is continued until '$\|e_g\| < \xi$' becomes true, where the threshold 'ξ' can be set by the system operator depending on the grid requirements. Further, if the time derivative of the error '$\dot{e}_g$' exceeds 'σ' which is the threshold set for the error time

derivative, the synchronization algorithm changes the direction of the frequency perturbation. In such a case, the synchronization algorithm starts scaling the current instance inverter frequency by a factor of 1.05. This makes the error 'e_g' to decrease gradually at each sampling instance, until it falls below the threshold limit. Once the magnitude and frequency of the inverter output voltage match with the grid voltage, the synchronization block makes the '$Connect$' signal high indicating the STS to close and the inverter transits to GC mode. The synchronization algorithm that enables the transition from GC to IS mode of operation is illustrated in Fig. 2.6.

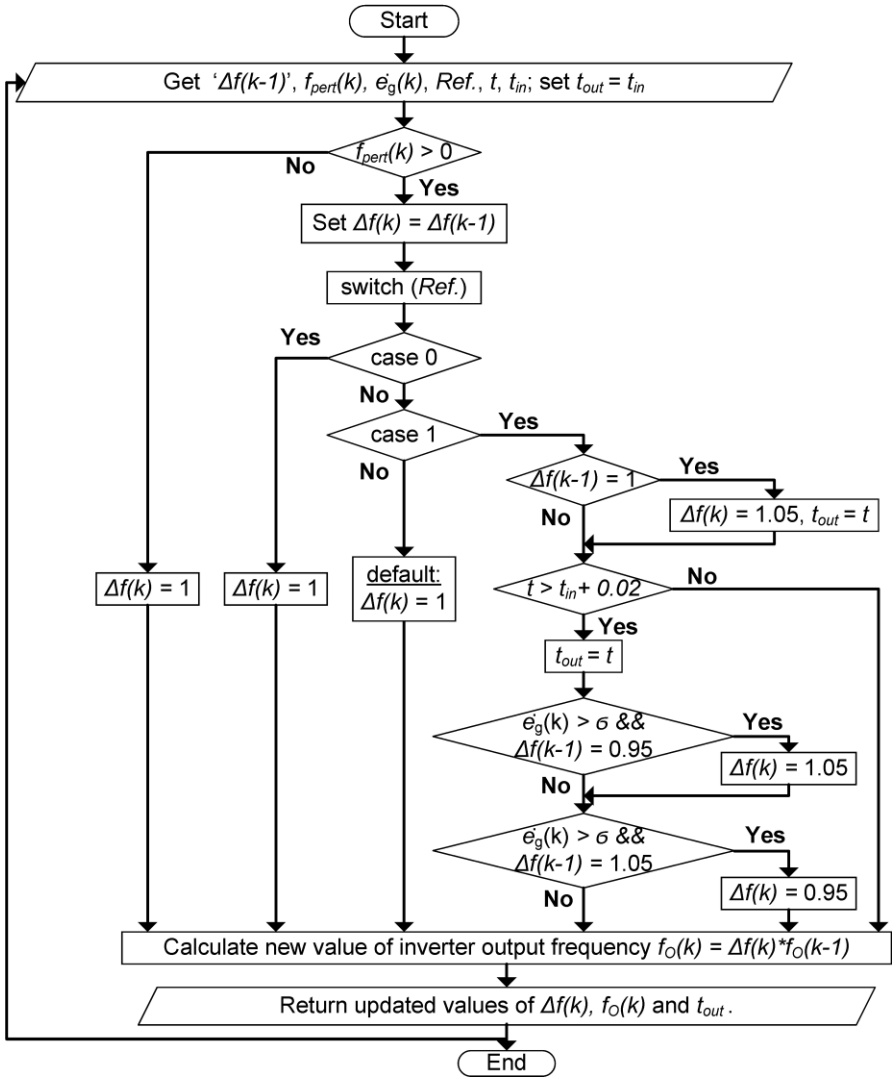

Fig. 2.6. Flowchart illustrating the operation of synchronization block

2.7.4 Simulation results

In order to validate the performance of the proposed MPC based controller, a low power grid tied inverter is simulated in MATLAB Simulink environment. Here, the PV cluster connected to the inverter's dc side is modelled as a dc source, since this chapter focuses on developing the inverter control. The pole 'A' of the inverter as shown in Fig. 2.4 is connected to the ac grid via a simple inductive 'L' filter and a STS; while the pole 'B' is connected to ground. A resistive local load is also connected at the inverter's output. The MPC based control scheme provides the switching signals to the gates of each of the four switches in the H-bridge. It also provides the '$Connect$' command to the STS to connect/disconnect the inverter from the grid. Grid status 'GS', inductor current 'i_L', grid voltage 'v_g', inverter voltage 'v_0' and active-reactive reference powers ('P_{ref}' and 'Q_{ref}') are the controller inputs sampled at every instance 'k'. The ratings of the inverter components used in the simulated inverter are mentioned in Table 2.3.

To verify the functionality of the proposed control, the inverter system is subjected to

Table 2.3. MPC based inverter parameters.

Symbol	Description	Value
v_g	AC grid nominal voltage	100 V_{p-p}
v_{pcc}	Inverter nominal output voltage	100 V_{p-p}
f_g, f_O	Nominal grid/ inverter output frequency	60 Hz
V_{DC}	DC source voltage	100 V
P_{ref}	Inverter's reference active power	600 W
Q_{ref}	Inverter's reference reactive power	50 VAR
R_g	Grid resistance	0.01 Ω
L_g	Grid inductance	0.1 mH
L	Filter inductance	5 mH
R_L	Load impedance	16.67 Ω
ξ	Grid error (e_g) threshold	5
σ	Differential grid error ($\dot{e}_g$) threshold	100

three different test scenarios. In Case Study 1, the transition of the MPC inverter from GC to IS mode of operation is evaluated. Furthermore, the reconnection of the inverter (transition from IS to GC mode) and the performance of the synchronization algorithm is analyzed in Case Study 2. Finally, the regulated active and reactive power injection capabilities of the proposed inverter control scheme in the GC mode of operation are validated in the Case Study 3. The results obtained from the simulations substantiate the functionality of the proposed MPC-based inverter control scheme.

2.7.4.1 Case Study 1:

Here, initially the grid status 'GS' input is high and the '$Connect$' output signal from the inverter's synchronization block is also held high as shown in Fig. 2.7(a). Thus, the MPC controlled inverter is operating in the GC mode ($\chi \epsilon \{3\}$). Here, the reference voltage level of 100 V_{p-p} is obtained from the grid and hence inverter does not regulate the output voltage 'v_{pcc}'shown by red plot in Fig. 2.7(b). The inverter phase angle 'θ' is perfectly synchronized with the grid voltage phase angle 'θ_g'. In this operation mode, the inverter operates in current controlled mode regulating the inverter output current 'i_L' to about 7.5A as shown by the green plot in Fig. 2.7(c). About 2.5A is absorbed to the local load and the remaining 5A is injected into the grid shown by the brown plot.

At about t = 0.853 sec, an intentional islanding is requested by the system operator, by making the 'GS' signal low. In response, the inverter almost instantaneously switches to IS operation mode ($\chi \epsilon \{4\}$) by making the '$Connect$' signal low. Accordingly, the STS is opened, and the inverter is disconnected from the grid. This can be observed from the grid current 'i_g' becoming zero, while the inverter output current 'i_L' drops to 2.5A as seen in Fig. 2.7(c). Beyond t = 0.853 sec, the inverter starts operating in output voltage control mode thereby regulating the

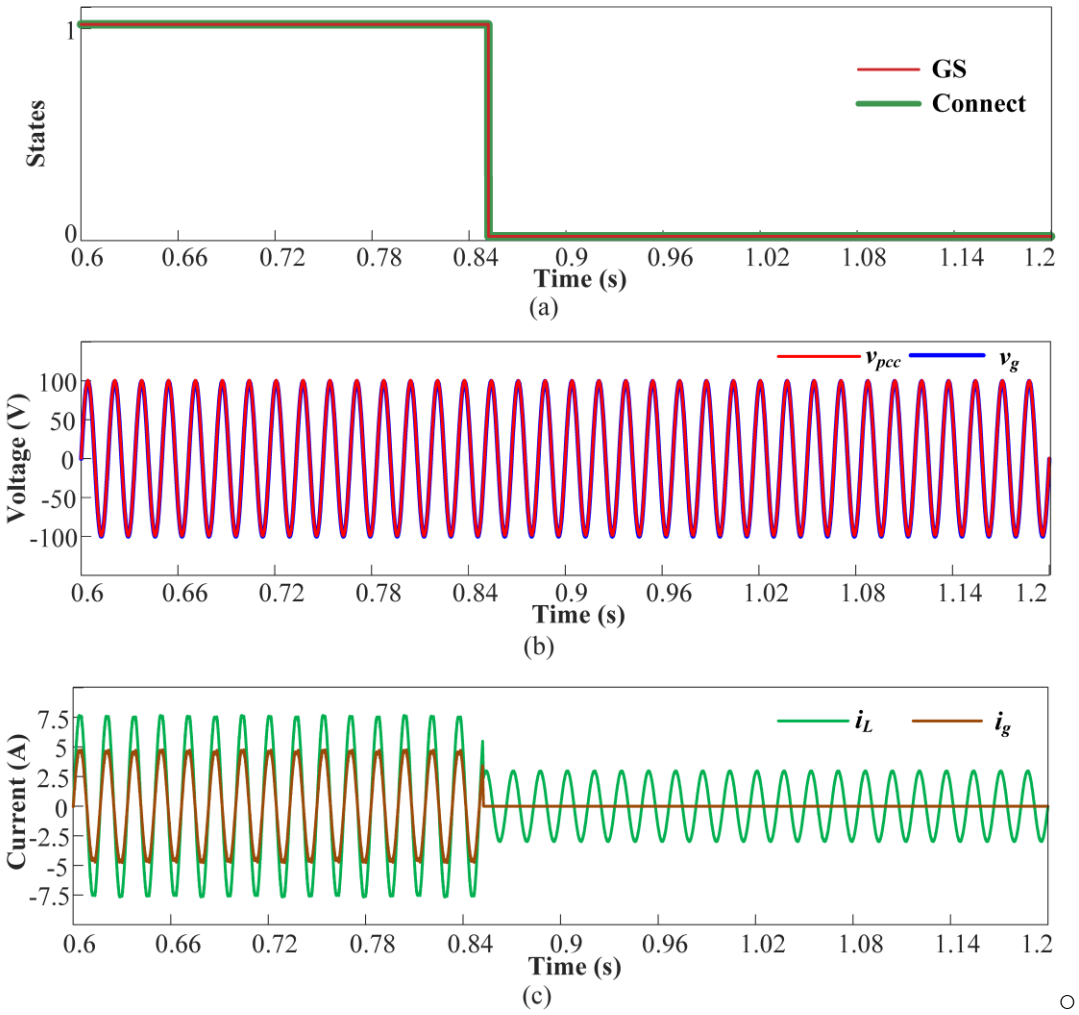

Fig. 2.7. Transition of the MPC controlled inverter from GC to IS mode of operation shown by (a) status signals, (b) inverter and grid voltages and (c) inverter and grid currents

voltage at PCC to 100 V_{p-p}. The inverter output voltage as well as inverter currents are bounded and does not show any transients. Thus, a smooth transition from GC to IS mode of operation is observed.

2.7.4.2 Case Study 2:

In the Case Study 2, the MPC driven inverter is initially operating in the IS mode with $\chi \in \{4\}$. In this mode, the inverter regulates its output voltage 'v_{pcc}' at 100 V_{p-p} indicated

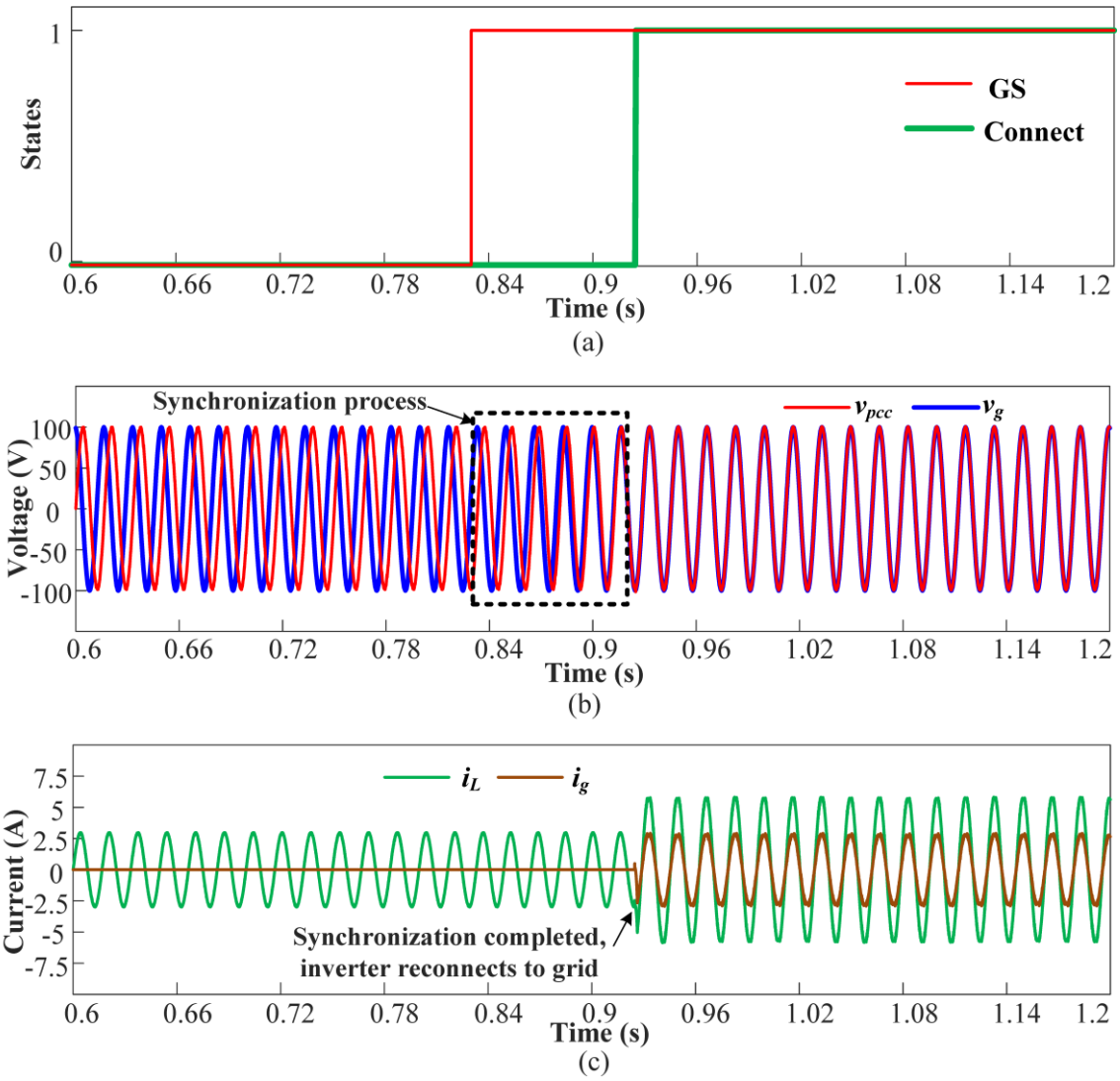

Fig. 2.8. Transition of the MPC controlled inverter from IS to GC mode of operation shown by (a) status signals, (b) inverter and grid voltages and (c) inverter and grid currents

by the red plot in Fig. 2.8(b). The inverter output current 'i_o' is equal to the current absorbed by the local load indicated by green plot, while the current fed to the grid is zero indicated by brown plot in Fig. 2.8(c). The grid voltage is not aligned with the inverter output voltage as noticed in Fig. 2.8(b).

Now at about t = 0.818 sec, the grid operator requests the inverter to reconnect by making the 'GS' signal high. In response, the inverter's controller initiates the synchronization process

by perturbing the inverter output frequency 'f_o' so that the inverter output phase 'θ' and the grid voltage's phase 'θ_g'are perfectly aligned. This operation is illustrated in Fig. 2.8(b) where the inverter output voltage's frequency is perturbed around the grid frequency 'f_g' until a perfect synchronization between the two voltages is achieved. At about t = 0.93 sec, synchronization between 'v_O' and 'v_g' is complete and the inverter can now safely reconnect to the grid. Accordingly, the '$Connect$' signal is made high by the synchronization block and the STS is closed. The inverter now transits into GC mode ($\chi \in \{3\}$) and starts regulating the grid injected current. This seamless reconnection of the inverter is evident from the smooth rise in inverter current 'i_L' (green plot) as well as the grid current 'i_g' (brown plot) in Fig. 2.8(c). The bounded and transient-free nature of the inverter output voltage and current validate the smooth transition of the inverter from GC to IS mode of operation.

2.7.4.3 Case Study 3:

The performance of the proposed MPC based inverter controller to variations in PQ operation set-points is tested in this case study. Here, the inverter continues to operate in GC mode for the entire duration of this case study. Initially, the inverter is feeding a total active power of about 300 W to the local load and the grid combined; as shown by the red plot in Fig. 2.9(a). The reactive power injection is regulated to 0 VAR indicated by the green plot. Here, the inverter output voltage (shown by red plot in Fig. 2.9(b)) is set by the grid while the inverter operates in current controlled mode regulating the grid injected current to about 2.5A.

Now at about t = 0.795 sec, the active power reference 'P_{ref}' indicated by blue dotted line in Fig. 2.9(a) is increased to 500 W; while the reactive power reference 'Q_{ref}' still maintained at 0 VAR. Accordingly, the inverter starts tracking the new active power reference (red plot); by increasing its output current to about 10 A as shown in Fig. 2.9(c). Further, at

about t = 0.95 sec, 'Q_{ref}' indicated by orange dotted line in Fig. 2.9(a) is increased to 50 VAR. The inverter tracks the new value of 'Q_{ref}' in less than about 0.02 sec (green plot in Fig. 2.9(a)) which is evident from the deviation observed in the inverter and gid current in Fig. 2.9(c).

The inverter's ability to track the new power references almost instantaneously validates the accordance of the proposed MPC based inverter controller to PQ operation set-point

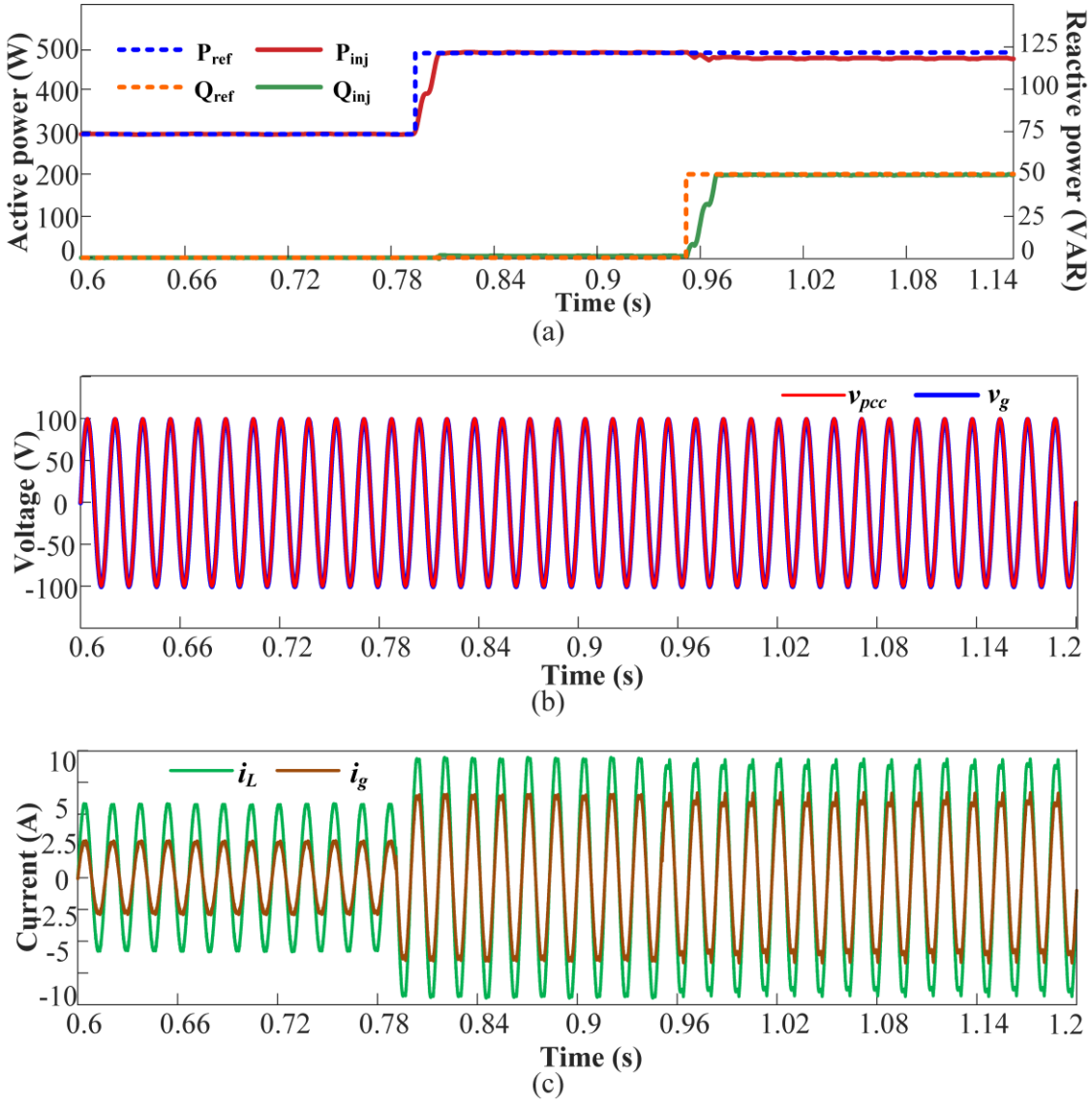

Fig. 2.9. Controller performance to PQ setpoint variations shown by (a) reference and injected active-reactive powers, (b) inverter and grid voltages and (c) inverter and grid currents

adjustments as dictated by the grid operator. This enables the grid operator to control the amount of PV power injected in the grid in a dispatched manner and thereby maintain the demand-supply balance. This helps improve the grid stability as well as the situational awareness of the PV cluster dominated grid as discussed in the next chapter.

2.7.5 Conclusion and remarks

This chapter provides a brief overview of the existing control strategies in literature that support seamless transition in MGs. Based on the analysis, it has been concluded that distributed control schemes offer the most optimal performance for MG control in terms of computational burden, communication dependency, power sharing ability and resiliency to grid failures.

Accordingly, a MPC based distributed control has been proposed for the inverter interconnecting the PV clusters and the power grid. The proposed MPC based inverter controller exhibits excellent active and reactive power tracking capabilities. Furthermore, it provides the ability to seamlessly transit from GC to IS modes of operation and vice versa without introducing fluctuations in the grid. The inherent nature of the model predictive control provides the controller with fast responses to state transitions. The proposed inverter control architecture shall be employed in interconnecting the PV clusters to the grid in the later chapters.

Chapter 3 - PV Clusters and Distributed Power Reserve

In a highly PV penetrated grid, the primary concerns related to intermittency and low inertia can be addressed through deploying an interconnected network of MGs. Typically, in such MG systems, the intermittency and low inertia related issues are mitigated by deploying energy storage units such as BESSs at specific locations. The BESSs provide the power reserve needed to mitigate the source side power fluctuations [62, 97, 98]. However, the downside of using the BESS is the supplementary costs and rapid charge/ discharge cycles resulting in significant reduction in their capacity and lifespan [99, 100]. Hence, BESS is recommended to be utilized for handling only the long-term transients [101].

3.1 Flexible power generation

A promising solution to mitigate the short-term power transients that may arise on the generation side is to deploy PV sources as clusters in a MG and autonomously adjust their operation set-points – realizing flexible PV power generation. This also refers to the regulating the PV output power based on the demand [102-104]. The existing flexible PV power generation mechanisms include constant power generation [102, 105], absolute active power control [99], power reserve control [106], delta power control [103] and ramp-rate control [107]. All these control approaches indicate that the PV units should be equipped with flexible power point tracking feature along with the maximum power point tracking (MPPT) algorithm [108, 109]. Furthermore, numerous standards and grid codes have been developed recommending flexible PV power generation to provide ancillary services for the high PV penetrated grid [110-113]. For instance, the German BDEW standard suggests PV operation set-points' adjustment to enable grid frequency regulation by PV units during grid's faulty conditions [113].

Furthermore, clustering of PV sources within the MG improves the controllability and situational awareness of a high PV penetrated utility grid while minimizing the communication requirements to the contours of the PV cluster [26, 67]. Power set-point regulation at the converter level by implementing PV clusters enables flexible power generation [26]. This PV operation set-point regulation feature can be leveraged for mitigating short-term transients in PV power generation at no additional hardware costs.

3.2 Literature review

Operation of PV systems at non-maximum power point (MPP) is well-established in literature and has already been used in fault-ride through and other grid ancillary services [114-118]. In particular, the distributed power reserve in each PV cluster can be utilized to mitigate the power fluctuations and imbalances observed in the MG. However, the main challenge with the power reserve control is estimating the maximum available PV power [119, 120]. In [107, 108], the converter level power reserve is explained assuming that all PV sources are under uniform irradiance level, which isn't the case in practical scenarios. Besides, the control scheme discussed in [105, 119], includes communication between the master and slave PV sources to estimate the total available power from the PV system. One of the solutions proposed in [99] uses the measurement from the field for the available irradiance along with the PV panel model. An alternative approach that uses curve-fitting algorithms for MPP estimation has been suggested in [121, 122]. This eliminates the reliance on temperature or irradiance sensors. In [123], another power reserve control approach has been proposed that uses a Lambert-W function for MPP estimation also does not require any additional hardware. However, in all the works proposed so far, the PV source is modeled as a controlled dc current source and the

impacts of source side fluctuations arising due to the solar irradiation variations are not taken into consideration.

Consequently, this chapter proposes an adjustable constant power generation control scheme for PV clusters connected in a MG. By utilizing the PV cluster architecture, the PV power reserve is distributed among all the interconnected PV sources in the cluster, which was otherwise realized by connecting a BESS in the MG. This PV power reserve is maintained in each PV source by operating them at a sub-optimal power level which is lower than their maximum output power level on their P-V curves. The dynamic and fast response of the dc-dc converters is leveraged to compensate for the power loss arising from the shaded PV source which is subjected to the fluctuating solar irradiation. Using the concept of constant power generation (CPG) [26], the neighboring PV sources within the cluster can harvest additional demanded power and compensate for the power loss. Thus, the short term transients in PV power due to solar irradiance fluctuations can be mitigating by utilizing the distributed PV power reserve. This facilitates significant reduction in the sizing of the BESS needed in the MG. Furthermore, this distributed power reserve can be dynamically adjusted by the grid operator to regulate the amount of PV power injection into the grid. This dispatchable power injection facilitates the operator to maintain the voltage and frequency of the MG/grid in events of sudden load variations. Thus, the proposed distributed power reserve enables mitigation of source side power fluctuations as well as *V-f* deviations arising in the grid during extreme loading scenarios.

3.3 System description

The proposed system architecture integrates PV sources into the MG/grid as PV clusters which are capable of supplying the dc MG with adjustable PV output power; according to the

limits dictated by the grid operator. As shown in Fig. 3.1, the dc bus is connected to the 5th bus of an IEEE 5-bus system through the bi-directional MPC based inverter as discussed in the previous chapter. The dc MG being considered is made up of multiple PV clusters and can operate in IS mode, if needed. The various PV clusters in the dc MG facilitate the realization of the distributed power reserve on the PV sources. Each cluster consists of multiple parallel connected PV strings

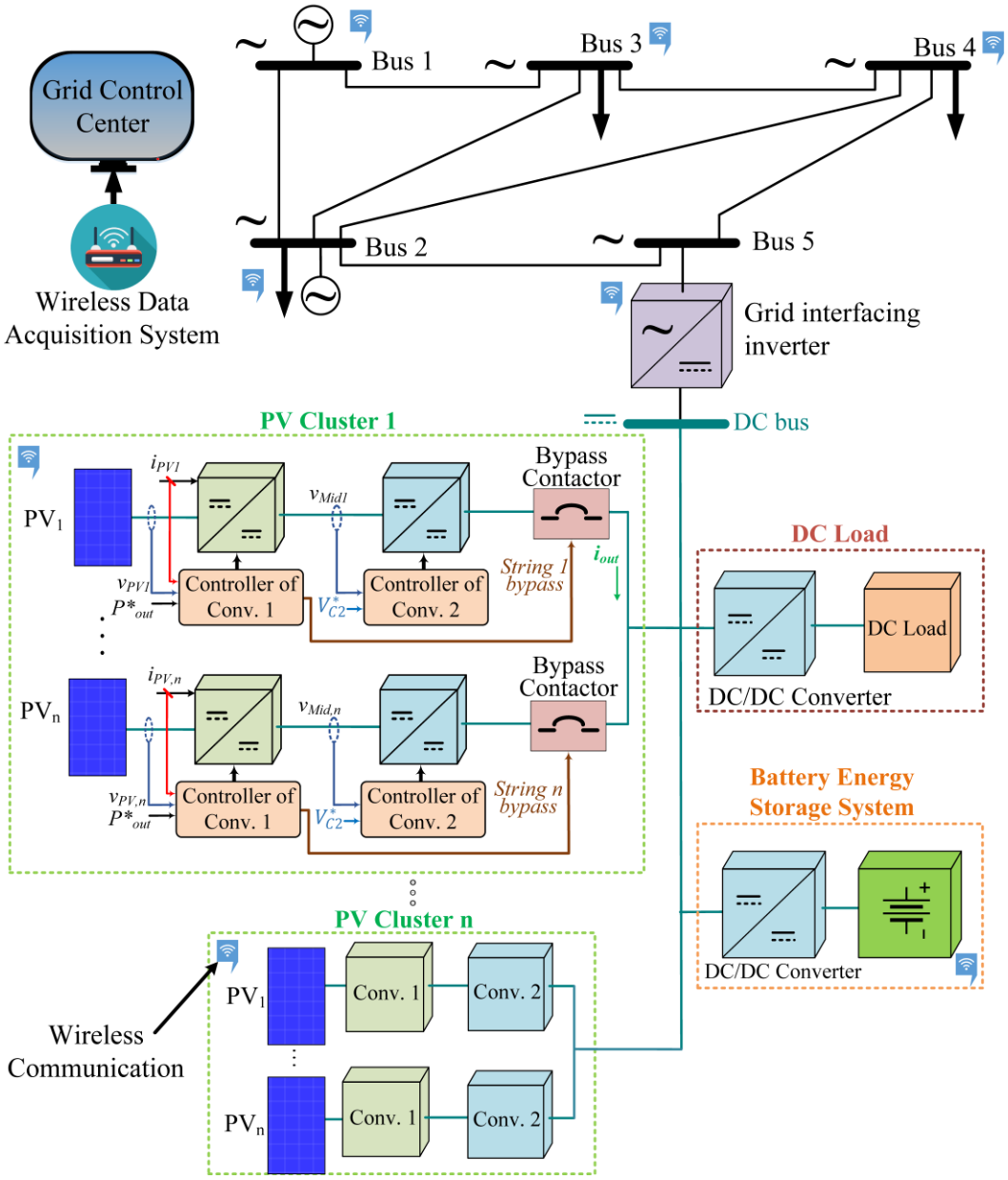

Fig. 3.1. PV cluster architecture connected to the IEEE 5-bus system

where each string is made up of a PV source followed by a cascaded configuration of two dc-dc boost converters. The cascaded dc-dc converter architecture is commonly utilized in dc MGs [124] to enhance the operation of islanded dc MGs such as dc bus voltage regulation. As depicted in Fig. 3.1, the two cascaded dc-dc boost converters with independent controllers are connected in each of the 'n' PV strings of a cluster.

The source side converter (SSC) or the converter 1 connected to PV sources is governed by the proposed modified incremental conductance – constant power generation (mINC-CPG) algorithm and extracts the set amount of constant power from the connected PV source; thereby maintaining a power reserve 'ΔP'. The grid side converter (GSC) or the converter 2 connected to dc bus is responsible for mitigating the mismatches among the PV strings under output power mismatch conditions. The grid controller communicates with each PV cluster periodically via the wireless communication system. A bypass contactor placed at the end of each PV string and controlled by the SSC's controller disconnects the specific PV string to protect the rest of the system in cases of short circuit failures in on the source side. Local loads are also interfaced to the dc bus via appropriate converters. In order to mitigate the long-term power transients that arise on the source side as well as to maintain the generation-load balance in the long-time duration, a BESS is incorporated in the system.

Table 3.1. Modes of operation of individual PV string in each PV cluster.

PV power	**Reserve power (ΔP)**	**Low voltage ac grid**	**PV operating mode**
$P_{PV} > P_{out}^{*}$	$P_{PV} - P_{out}^{*}$	Grid-stand-by mode maintaining dc bus voltage	$P_{out}^{*} < P_{MPP}$; CPG mode
$P_{PV} = P_{out}^{*}$	0	Grid-stand-by mode maintaining dc bus voltage	MPPT mode
$P_{PV} < P_{out}^{*}$	0	Grid supplies power to dc bus ($P_{out}^{*} - P_{PV}$); if required.	MPPT mode

3.4 Photovoltaic cluster control strategy

The proposed distributed control for PV clusters supplies the dc MG with adjustable PV output power, irrespective of variations in the solar irradiation. As expressed in Table 3.1, if the total output power from each PV cluster 'P_{PV}' exceeds the adjustable limit of 'P^*_{out}', the power generation is limited to 'P^*_{out}'; by the proposed mINC-CPG algorithm. This ensures a regulated power generation such that a reserve power 'ΔP' equal to '$P_{PV} - P^*_{out}$' is available to the grid operator as a dispatchable reserve; for use in the event of power imbalance or stability issues. Initially, it is assumed that the incident solar irradiation on each PV string in a cluster is uniform and hence the power limit is distributed evenly among the 'n' strings as '$P^*_{out,n}$' by using the relation (3.1).

$$P^*_{out,n} = \frac{P^*_{out}}{n} \quad ; \quad n = \text{number of strings in PV cluster} \tag{3.1}$$

However, when the power output of one or more PV strings drops below their preset limit '$P^*_{out,n}$', the neighboring PV strings will increase their allotted power limit and move into MPPT mode to harvest additional power required to maintain the total power fed by the PV cluster. In case, the total available power from the PV cluster 'P_{PV}' is less than the set limit 'P^*_{out}', all the 'n' strings will move into MPPT mode and start harvesting the maximum available power. In this mode, the operation set-points of each PV string will be shifted towards their respective MPPs. The amount of power injected by the PV cluster is governed by the relation (3.2). Furthermore, the amount of dispatchable power reserve 'ΔP' available in each PV cluster at any time instance is given by (3.3).

$$P_{out} = \begin{cases} P_{out} & when \quad P_{out} < P^*_{out} \\ P^*_{out} & when \quad P_{out} > P^*_{out} \end{cases} \tag{3.2}$$

$$\Delta P = P_{out} - P^*_{out} \tag{3.3}$$

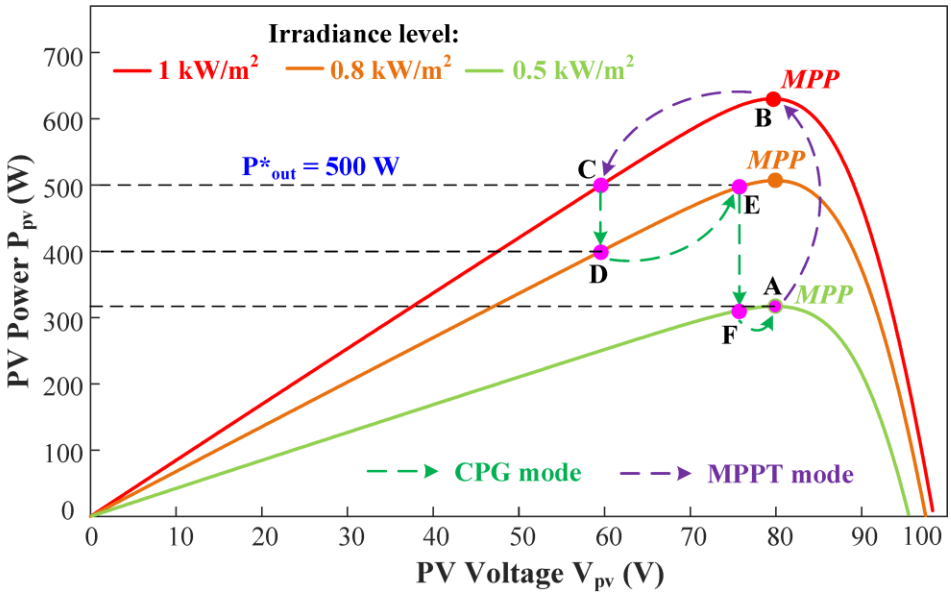

Fig. 3.2. Operation concept of mINC-CPG scheme to extract constant power and maintain power reserve

The concept of the adjustable power reserve using CPG is illustrated in Fig. 3.2. Here, each PV string generates output power '$P_{PV,n}$' less than or equal to the limit '$P^*_{out,n}$', irrespective of the solar irradiation variations. As the solar irradiation increases from 500 W/m^2 to 1000 W/m^2, the SSC encounters a sudden increase in the available power from 310 W at point A to 610 W at point B. Since the PV power limit '$P^*_{out,n}$' is set by the grid operator as 500 W, the mINC-CPG configured SSC of each PV string shifts its operating point to the left of the MPP at point C; where the PV string output power is regulated down to within the limit.

Under normal conditions when the incident solar irradiation is at 1000 W/m^2, the PV string will continue to operate at point C thereby generating constant power of 500 W and maintaining a power reserve of about 110 W. Even if the solar irradiation further increases, the PV operation set-point will be adjusted by the SSC to generate output power less than or equal to the set limit. Furthermore, at the instance the solar irradiation drops to 800 W/m^2, the PV

string's operation point drifts to point D and the output power drops to 400 W. Now, in response to the drop in the output power, the PV string's SSC shifts its operation set-point to the right towards the MPP to point E. At point E, the PV power output is restored back to 500 W by utilizing the maintained power reserve 'ΔP'. However, any further decrease in the solar irradiation (point F) causes the power reserve 'ΔP' on that string to be depleted and hence this string transits into MPPT mode and harvests the maximum available power. This is shown by the transition back to point A (which is the MPP at 300 W/m^2). In such situation where no power reserve is available on that particular PV string, the neighboring PV strings will start increasing their individual harvested power by shifting their operation set-point towards the MPP. This process is continued until the output power of the PV cluster does not match the grid operator specified limit 'P^*_{out}'. Thus, despite the drop in the power output of 'm' PV strings in a cluster of total 'n' PV strings, the neighboring '$n - m$' PV strings will compensate for the loss of power and ensure a constant amount of PV cluster power fed to the dc MG/grid.

The above discussed operation of the mINC-CPG algorithm for one of the 'n' PV strings in a cluster is illustrated in time domain in Fig. 3.3. The profile of PV string's available power is illustrated by the red curve, while the PV string's output power is represented by the green curve. The total time duration is split into three intervals where intervals 'T_1', 'T_2' and 'T_3'. 'T_1' and 'T_3' represent early morning hours and late evening hours respectively with the weak solar irradiation levels; while interval 'T_2' represents most of the day duration when the solar irradiation is sufficiently strong. It is observed that during the time interval 'T_2' the available power 'P_{PV}' from the PV cluster is greater than the limit 'P^*_{out}' and hence the PV string operates in the CPG mode. Here, the output power of each PV string is capped to '$P^*_{out,n}$' which is 500 W.

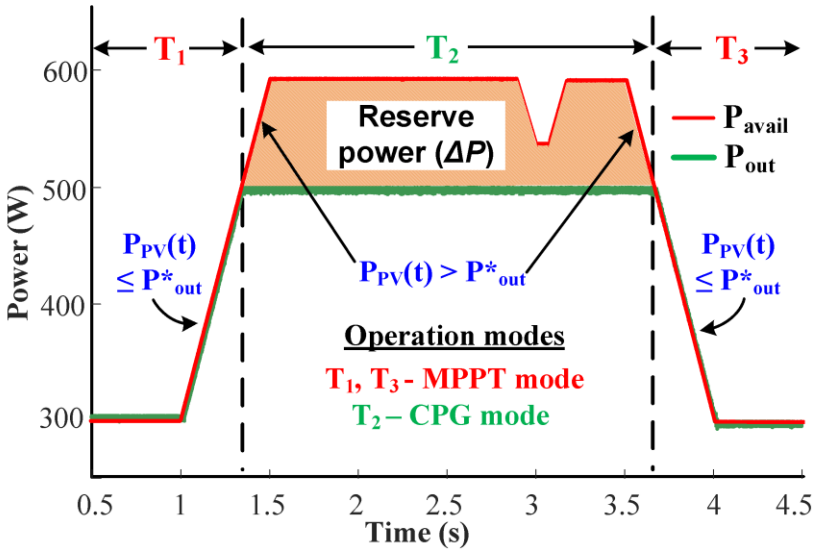

Fig. 3.3. PV output power is regulated within the limit P^*_{out}; set by MG/grid operator

This ensures a constant power fed by the PV cluster to the dc MG even if the incident solar irradiation profile has fluctuations. Furthermore, a dispatchable power reserve 'ΔP' (of about 100 W) in each PV string is available to the grid operator for most time of the day. During the time intervals 'T_1' and 'T_3', the total power output of the PV cluster is less than the 'P^*_{out}' and hence the PV strings operate in MPPT to harvest the maximum available power. Thus, during the peak hours of the day, the power fed to the dc MG/grid by the PV cluster is maintained constant despite the variation in the incident solar irradiation. Hence, the proposed mINC-CPG algorithm helps to mitigate the source side power fluctuations.

Moreover, the grid operator can dynamically adjust the value of 'P^*_{out}' and extract additional power from the PV strings for grid support functions by leveraging the distributed PV power reserve. In other words, the proposed algorithm provides flexibility for grid operator to autonomously adjust the PV clusters' power generation to facilitate the implementation of a more resilient grid, considering the high penetration of PV sources. This further limit the

implementation of costly energy storage in the MG. The choice of optimal 'P_{out}^{*}' and consequently 'ΔP' selection is still a currently trending open research question and depends on multiple factors such as nature and pattern of incident solar irradiation profile, loading profile of the MG/grid, size of the PV system, etc. [26]. The complete CPG control strategy of the proposed algorithm can be summarized in the flow chart shown in Fig. 3.4 and can be divided into 3 regions: region 1, region 2 and region 3. The detailed explanation about each region and the criteria for transition to another region is mentioned below:

3.4.1 Region 1:

A PV string operates in this region when power output of each PV string '$P_{PV,n}$' is less than 'P_{limit_n}' that is '$P_{PV,n} < P_{limit_n}$'. This region tries to track the MPP but the control will go out of this region as soon as the output power exceeds the limit which is $P_{PV,n} > P_{limit_n}$.

3.4.2 Region 2:

When PV cluster output 'P_{out}' is less than operator set limit 'P_{out}^{*}' that is '$P_{out} < P_{out}^{*}$', 'P_{limit_n}' for each PV string is increased so as to make sure that 'P_{out}' is equal to 'P_{out}^{*}'. The maximum value 'P_{limit_n}' can be assigned is the PV string power at its maximum power point 'P_{MPP}', since it is the maximum available power.

3.4.3 Region 3:

When the PV cluster output 'P_{out}' is greater than the operator set limit 'P_{out}^{*}' that is '$P_{out} > P_{out}^{*}$', 'P_{limit_n}' is decreased so as to make sure that 'P_{out}' is equal to 'P_{out}^{*}'. 'P_{limit_n}' is not decreased beyond the initial assigned value '$P_{limit_n}(initial)$' given by (3.1). The primary reason being that CPG operation is not required when 'P_{PV_n}' is less than '$P_{limit_n}(initial)$' and that particular PV string can operate in MPPT mode.

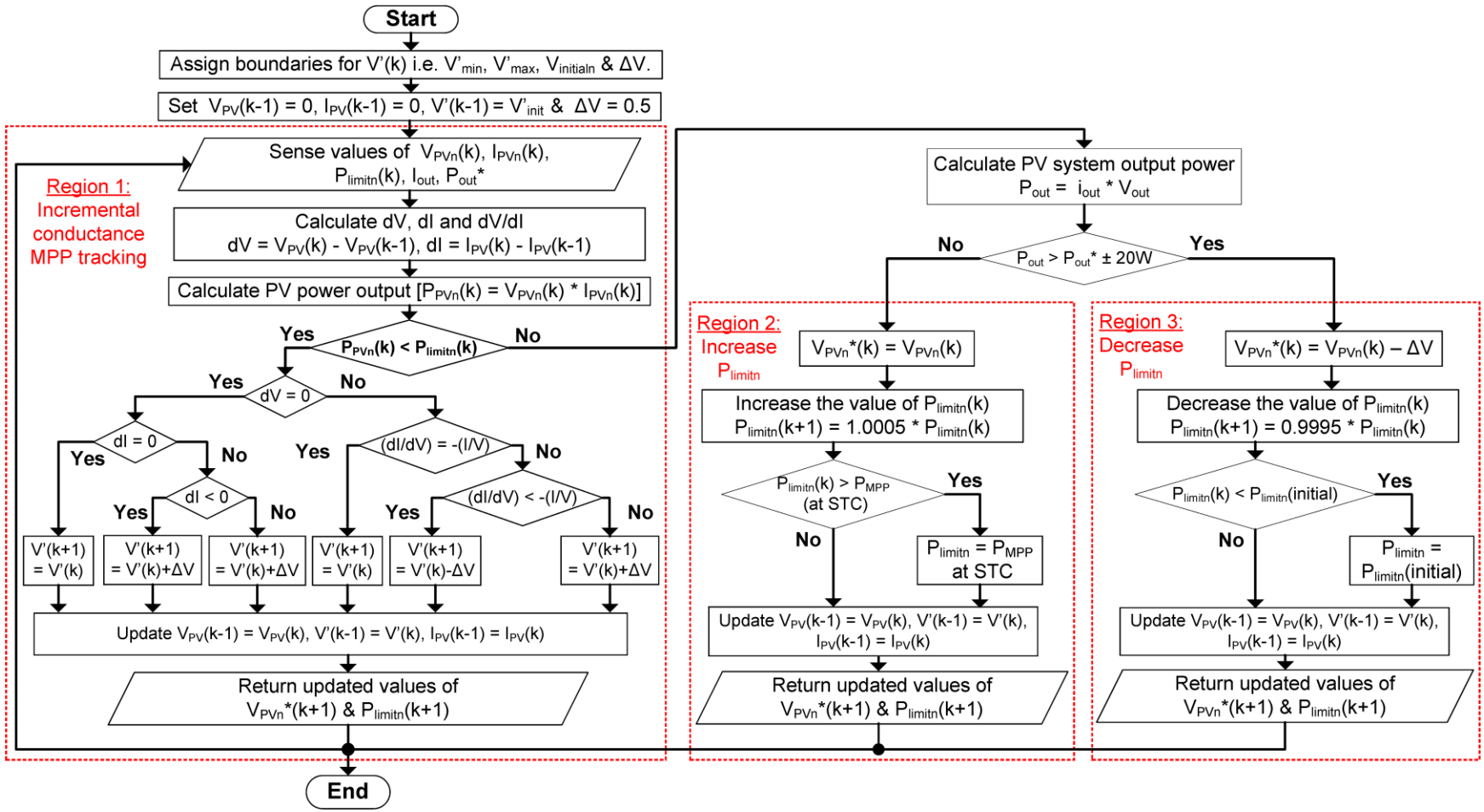

Fig. 3.4. Flowchart demonstrating operation of adjustable autonomous power reserve control.

3.5 Hardware-in-the-loop validation

To validate the performance of the proposed autonomous power reserve control and the PV cluster architecture in real-time hardware in the loop setup, the Typhoon HIL 402 emulator depicted in Fig. 3.5 is utilized. Here, three PV strings rated at 458.06 W P_{MPP} at 56.51V V_{MPP} and standard test conditions (STC) of 1000 W/m^2 and 25°C are considered in one cluster which feeds a total power 'P^*_{out}' of 900 ± 10 W to the dc MG. This dc MG is connected to bus number 5 in the IEEE 5-bus system through a bi-directional inverter. Besides, this dc bus has the capability to operate as an islanded dc MG if necessary. The individual PV string detailed ratings are depicted in Table 3.2 while the PV cluster ratings are mentioned in Table 3.3. For the sake of validation, three case studies with adjustable PV power reserve are considered. Case Study 1 tests the system response for steep variations in solar irradiations as a worst-case scenario or grid operator command to adjust the power reserve set-point. In Case Study 2, the impacts of gradual change in the solar irradiation simulating a cloudy day are investigated.

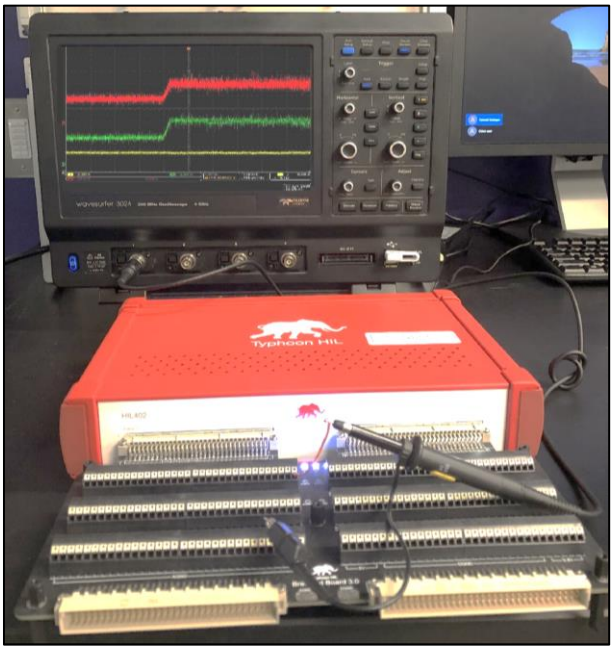

Fig. 3.5. Typhoon HIL 402 emulator used to implement HIL testing.

Finally, the effect of short circuit fault on a PV string in the cluster is discussed in Case Study 3.

Table 3.2. PV string parameters

Symbol	Description	Value
$R_{PV_{MPP}}$	PV string output impedance at MPP (STC)	10.45 Ω
$R_{PV_{MPP}}$	Nominal input voltage of SSC (STC)	56 V
D_1	Average duty cycle of SSC	0.41
L_1	Input inductor of SSC	5 mH
C_1	Output capacitor of SSC	960 µF
V_{dcl}	Nominal input voltage of GSC	95 V
D_2	Average duty cycle of GSC	0.26
V_g	Output voltage of GSC	130 V
L_2	Input inductor of GSC	5 mH
C_2	Output capacitor of GSC	800 µF
f_{c_1}, f_{c_2}	Switching frequency	20 kHz
f_{MPPT}	MPPT sampling frequency	10 kHz
V_{dc}	DC bus voltage	390 V
$P_{PVn_{out}}$	Power rating of each PV string	300 W

Table 3.3. MPPT-CPG governed PV cluster parameters.

Symbol	Description	Value
N_s	No. of strings	3
P_{MPP}	Maximum power for each string	458.06 W
V_{OC}	Open circuit voltage for each string	70.00 V
V_{MPP}	Voltage at MPP for each string (STC)	56.51 V
I_{SC}	Short circuit current for each string	9 A
I_{MPP}	Current at MPP for each string	8.11 A
P_{out}	PV cluster output power rating	900 W

3.5.1 Case Study 1:

Here, the solar irradiance on PV_2 and PV_3 are maintained constant at 1000 W/m^2. However, the solar irradiation on PV_1 is dropped from 1000 W/m^2 to 400 W/m^2 steeply at t = 1.1 sec and again suddenly returned to 1000 W/m^2 at t = 4.9 sec. The Fig. 3.6 - Fig. 3.9 demonstrate the entire scenario graphically. It can be observed from Fig. 3.6 that the output power 'P_{out}' is maintained almost constant at 'P^*_{out}' which is 900 W irrespective of changes in irradiance. In Fig. 3.6, at t = 1.1 sec, a sudden decrease in 'P_{PV_1}' can be observed which is represented by the orange plot. At this instance, PV_1 moves its operating point and start operating in MPPT mode (region 1) of the flowchart, since the available power from PV_1 is lower than the '$P_{limit,n}$' which is equal to 300 W. During this period, in order to compensate for the power drop of about 150 W in PV_1, the SSC's of PV_2 and PV_3 shift their operating points towards MPP to harvest additional power from their power reserves.

At t = 4.9 sec, the incident solar irradiation on PV_1 is restored back to 1000 W/m^2. At this instance, the system starts returning to the initial state. The PV strings PV_2 and PV_3 reduce their output powers as evident from Fig. 3.6. The change in the operating point of PV_1 is illustrated by the large increase in the operating voltage of PV_1; represented by the yellow plot in Fig. 3.7. Furthermore, Fig. 3.8 demonstrates that the PV cluster current 'I_{out}' stays constant at 2.3 A irrespective of the PV_1 current (I_{PV1}) dropping from 9 A to 2.8 A and back to 9 A. As $P_{PV1reserve}$ approaches zero (indicated by yellow plot in Fig. 3.9), the adjustable power reserves $P_{PV2reserve}$ and $P_{PV3reserve}$ maintained by PV_2 and PV_3 decrease proportionately so as to regulate the output power of the PV cluster at 900 W.

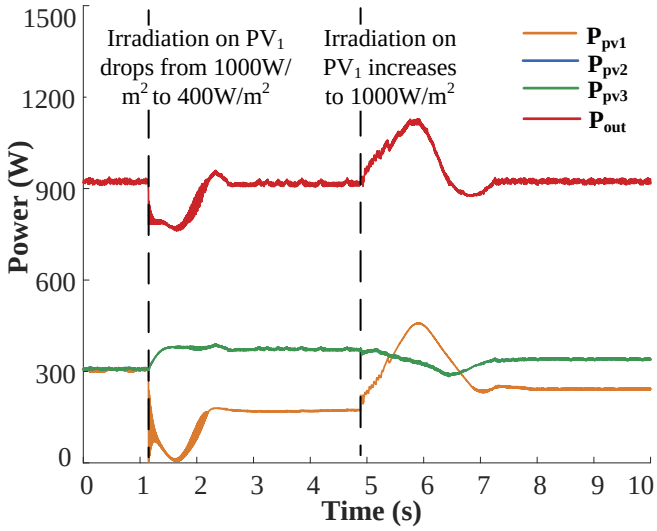

Fig. 3.6. PV_2 and PV_3 increase their output power to keep P_{OUT} constant when PV_1 drops from 300 W to 150 W and goes back to 300 W in Case Study 1

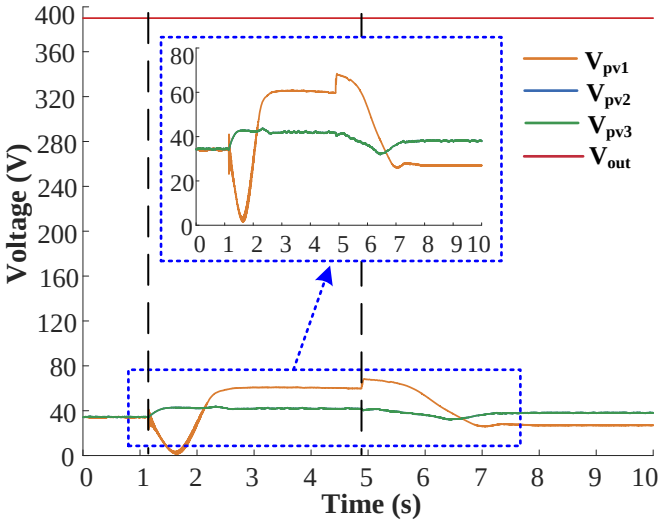

Fig. 3.7. DC bus voltage 'V_{out}' held constant at 390 V when PV voltages V_{PV1}, V_{PV2} and V_{PV3} vary as irradiation of PV_1 varies in Case Study 1

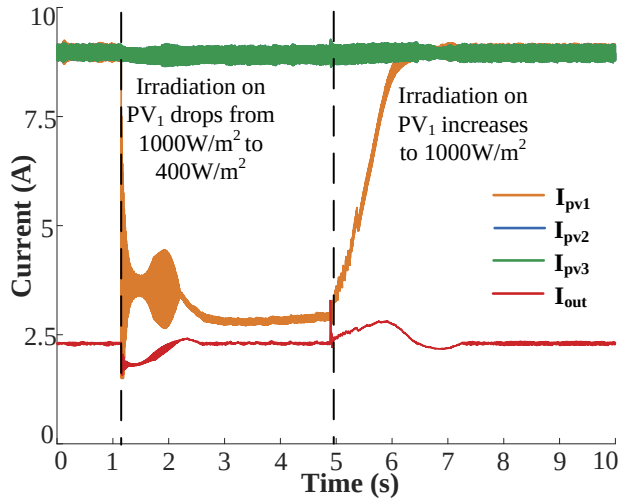

Fig. 3.8. DC bus current 'I_{out}' remains constant irrespective of variation in PV_1 current in Case Study 1

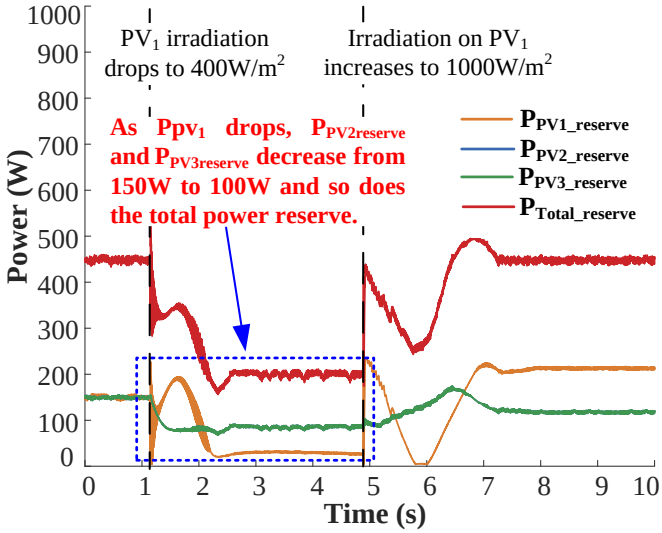

Fig. 3.9. '$P_{PV2\_reserve}$' and '$P_{PV3\_reserve}$' decrease as 'P_{PV1}' drops and hence '$P_{Total\_reserve}$' also decreases to compensate the power drop in Case Study 1

3.5.2 Case Study 2:

In Case Study 2, the irradiation on one of the PV strings varies gradually. At t = 0.5 sec, the solar irradiation on PV_2 is dropped from 1000 $W/m^2$to 800 W/m^2, then to 600 W/m^2 at t = 2.5 sec and finally to 400 W/m^2 at t = 6.5 sec. Further, the irradiation on PV_2 is increased back to 600 W/m^2 at t = 9.8 sec, then to 800 W/m^2 at t = 14.5 sec and finally to 1000 W/m^2 at t = 17.5 sec. This entire sequence can be observed in Fig. 3.10 which shows that the PV cluster output power 'P_{out}' remains almost constant at 900 W, irrespective of the decrease in power output of PV_2. During this entire duration, the drop in PV_2 output power 'P_{PV_2}' is compensated by P_{PV1} and P_{PV3}. Fig. 3.11 shows the shift in the operating voltage of PV_2 with decrease in the incident solar irradiation. Additionally, Fig. 3.12 shows a decrease in the output current from PV_2 while the PV cluster output current 'I_{out}' stays constant at 2.4 A. As the irradiation on PV_2 goes on increasing again, the operating point of PV_2 gradually moves back to the original position. The power reserve profiles for each PV panel as well as the varying total power reserve for the entire duration are showcased in Fig. 3.13.

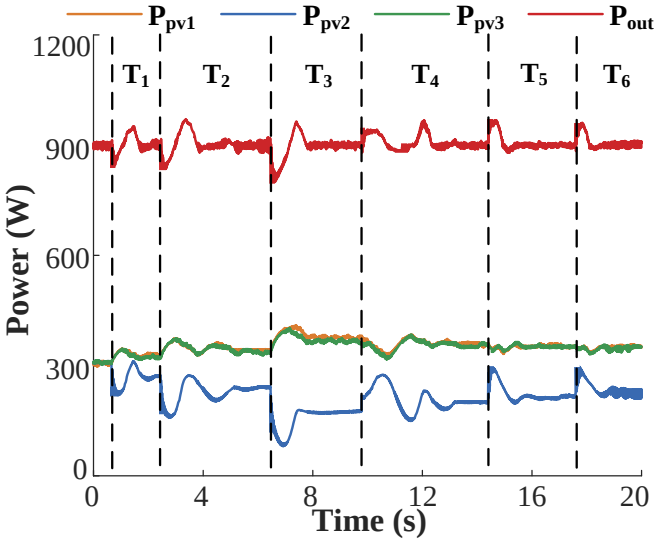

Fig. 3.10. Total power 'P_{out}' with irradiation variations (T_1, T_5: 800 W/m^2; T_2, T_4: 600 W/m^2; T_3: 400 W/m^2; T_6: 1000 W/m^2) in Case Study 2

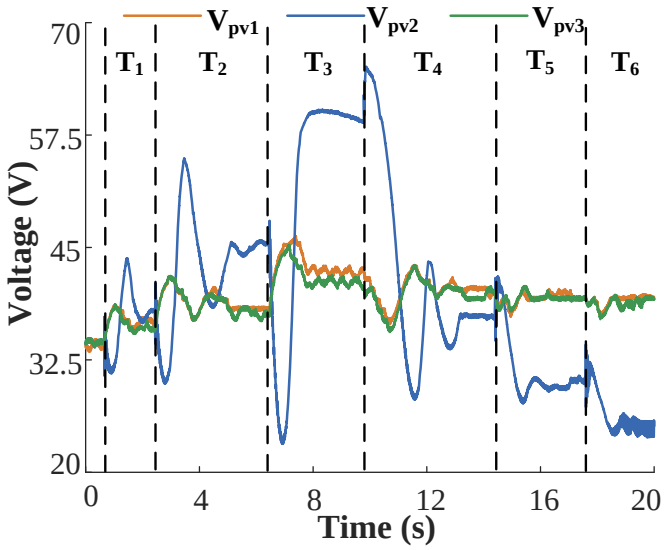

Fig. 3.11. V_{PV2} is increased with irradiation changes (T_1, T_5: 800 W/m^2; T2, T4: 600 W/m^2; T3: 400 W/m^2; T6: 1000 W/m^2) in Case Study 2

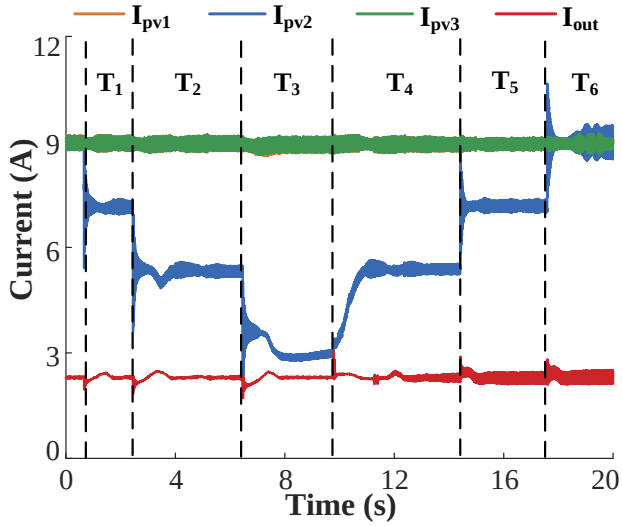

Fig. 3.12. I_{out} stays constant irrespective of irradiation variations (T_1, T_5: 800 W/m^2; T_2, T_4: 600 W/m^2; T_3: 400 W/m^2; T_6: 1000W/m^2) in Case Study 2

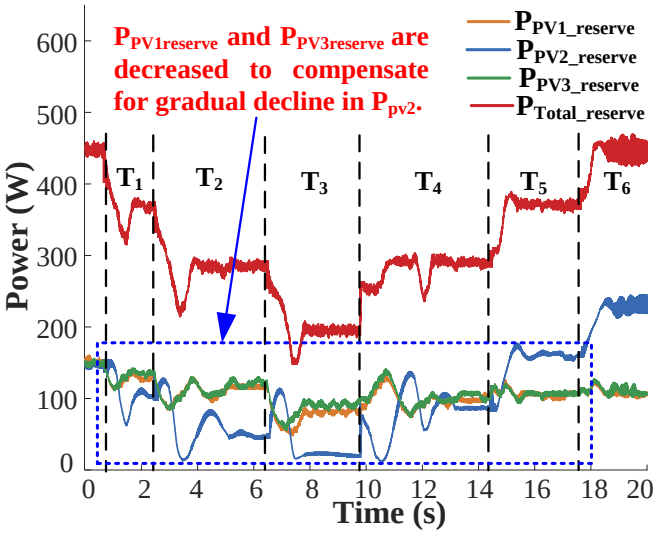

Fig. 3.13. As P_{PV2} goes on decreasing gradually, $P_{PV1\_reserve}$ and $P_{PV3\_reserve}$ decrease to compensate for the drop in output power in Case Study 2

3.5.3 Case Study 3:

Case study 3 demonstrates the response of the system to short circuit faults evident in Fig. 3.14 - Fig. 3.17. As seen in Fig. 3.14, the system continues to provide constant power output P_{out}, even in the event of a short circuit fault that occurs at the output of PV_2 at t = 2.4 sec. As P_{PV_2} drops, PV_1 and PV_3 move their operating set-points to increase their output powers; hence utilizing the available power reserve from the non-faulty PV sources. The drift in the operating set-points for PV_1 and PV_3 is evident in Fig. 3.15. The cluster current remains constant irrespective of the short circuit fault (see Fig. 3.16). Note that, in this case study the short circuit impedance is considered to be 4Ω. The power reserve profiles for each PV panel as well as the total power reserve for the entire duration of the case study are shown in Fig. 3.17.

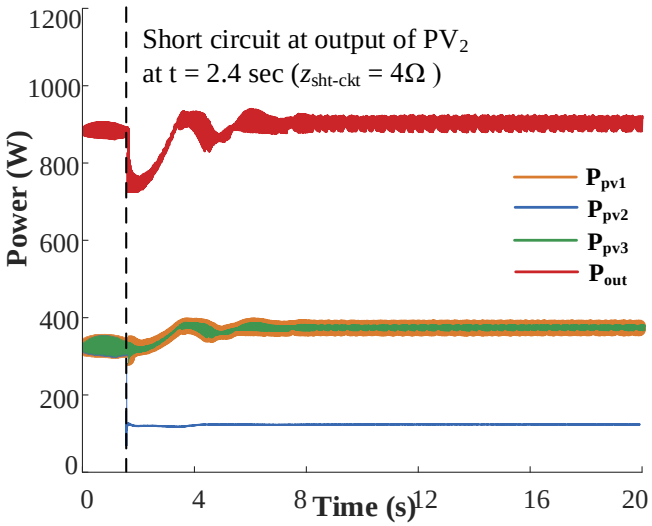

Fig. 3.14. Total power 'P_{out}' is maintained constant irrespective of short circuit fault that occurs in PV_2 at t = 2.4 sec in Case Study 3

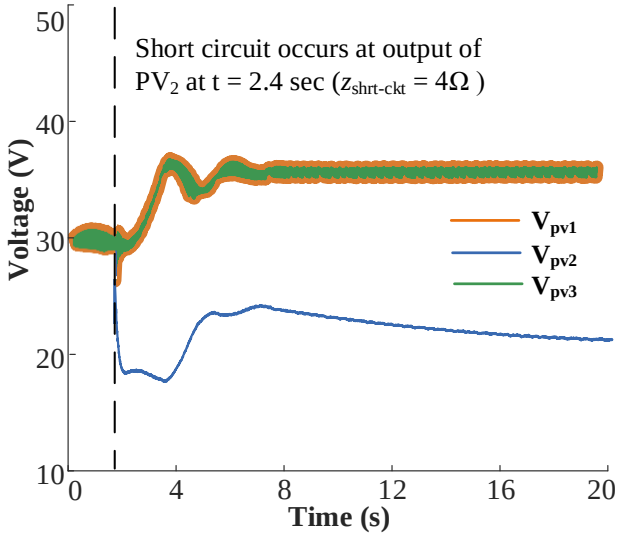

Fig. 3.15. V_{PV2} drops while V_{PV1} and V_{PV3} increase at the instant the short circuit fault occurs in PV_2 output at about t = 2.4 sec in Case Study 3

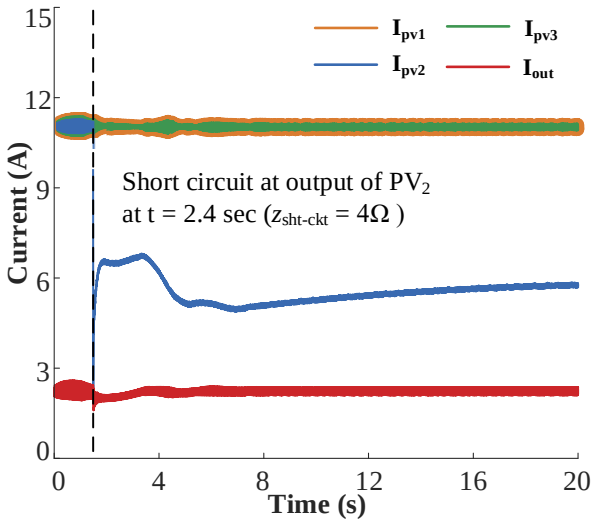

Fig. 3.16. I_{out} is maintained constant irrespective of short circuit fault that causes I_{PV2} to drop at about t = 2.4 sec in Case Study 3

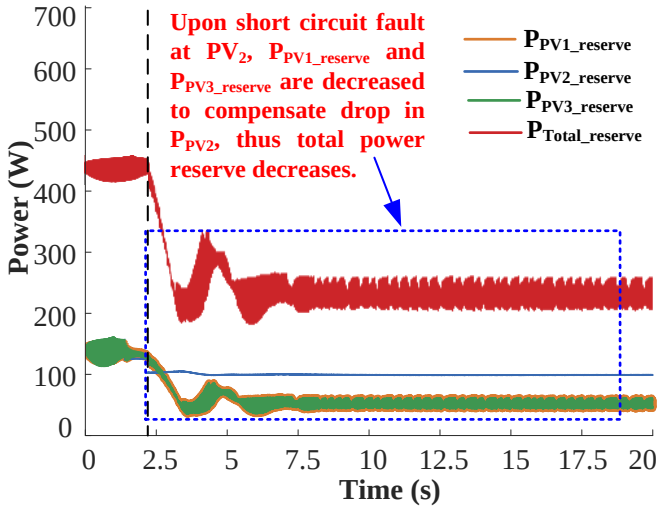

Fig. 3.17. $P_{PV1\_reserve}$ and $P_{PV3\_reserve}$ are utilized to compensate for the power drop arising from the short circuit fault in PV_2 output in Case Study 3

In summary, the above discussed case studies collectively validate the performance of the implemented system with respect to stability and restorability when subjected to intentional PV

power setpoint change, solar irradiation variations, as well as short term power transients such as short circuit faults.

3.6 Hardware experimental evaluation

In order to verify the feasibility of the proposed adjustable power reserve function in the proposed control scheme, the SSC of a single PV string was implemented in hardware. A GaN-switch based dc-dc boost converter was used in the experimental setup. The experimental setup includes: the GaN based boost converters, measurement boards, the mINC-CPG controller implemented on a dSPACE 1104, a filter board, a MagnaPower PV emulator, and measurement tools. The experimental setup is shown in Fig. 3.18. The PV system was tested to verify the controller response to changes in the power reference in real hardware experiments. The PV curve used by the PV emulator has its maximum power point (MPP) at about 56 V (V_{MPP}) and about 3.3 A (I_{MPP}) and the maximum power drawn from the PV panel is around 180 W (P_{MPP}) at solar irradiation of 1000 W/m^2.

Initially, according to the mINC-CPG control scheme, the SSC operation set-point is

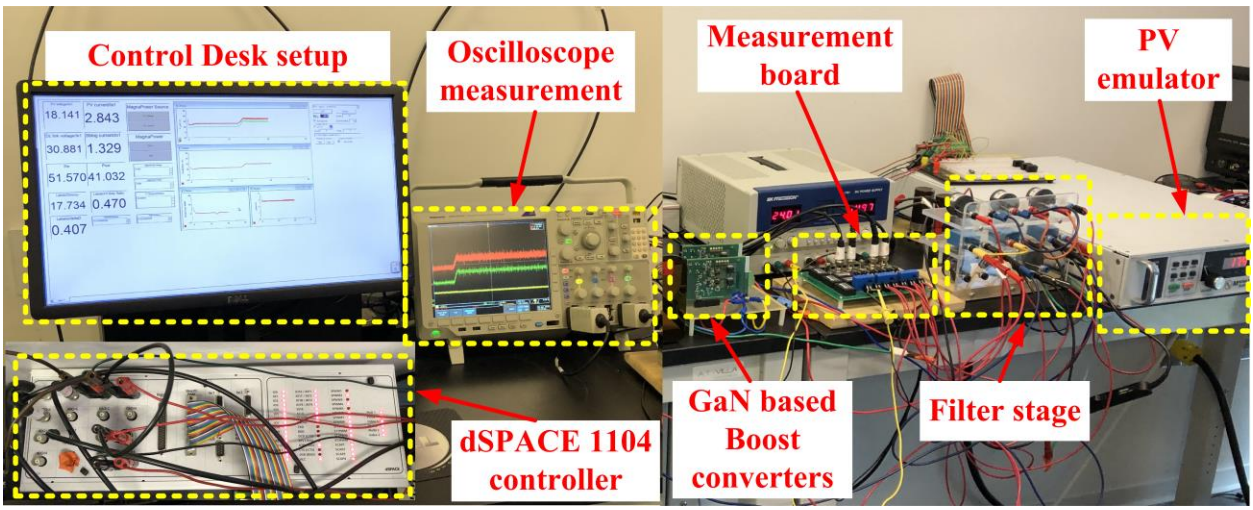

Fig. 3.18. Setup for mINC-CPG algorithm hardware implementation on GaN boost converter

regulated at about 32 V (which is the non-MPP voltage). During this time, the PV output is regulated at about 110 W with a power reserve 'ΔP' of about 70 W as shown in Fig. 3.19. At t = 8 sec, the operation set-points are adjusted to utilize the reserve power and operate at 170 W. This new set-point is considered based on a power mismatch in PV strings. The shift in the operation point is seen from the increase in the PV operating voltage at t = 8 sec in Fig. 3.20. Thus, the PV string output power is increased from 110 W to 170 W as illustrated in Fig. 3.19.

Furthermore, it can be seen from Fig. 3.21 that the PV string output current remains unchanged in the entire duration of the operation, thereby validating the operation of the PV source in constant current region. The large fluctuations in the output power and string current are due to the noise that gets coupled in the measurement circuitry.

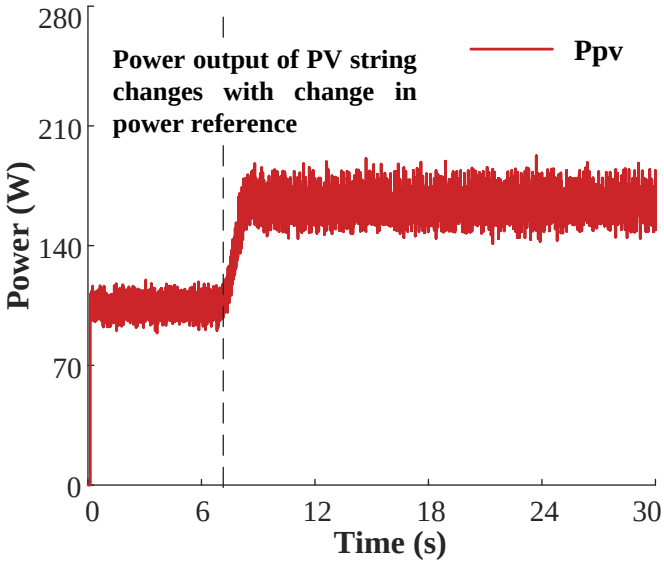

Fig. 3.19. PV string output power profile showing increase at t = 8 sec due to drop in power fed by neighboring PV strings

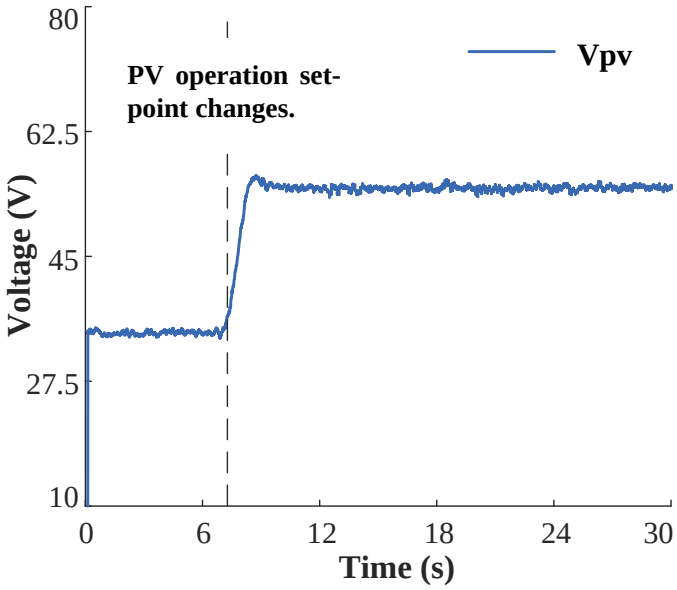

Fig. 3.20. PV string output voltage profile showing increase in PV voltage as operating point moves towards MPP at t = 8 sec

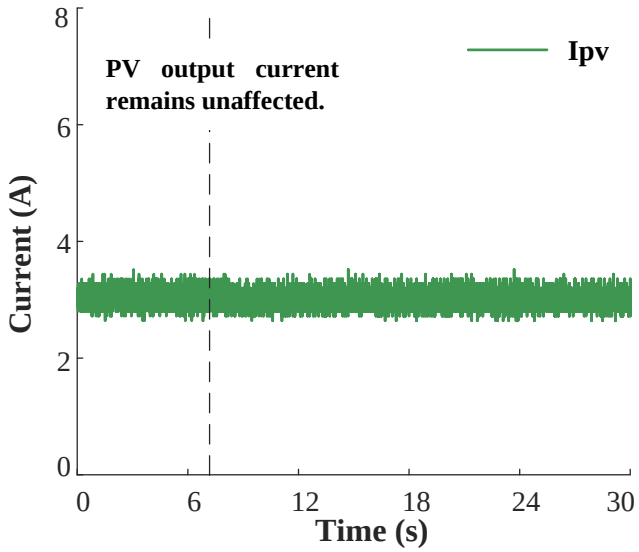

Fig. 3.21. PV string output current stays constant during output power being increased after about t = 8 sec due to operation in constant current region of the P-V curve

3.7 Conclusion and remarks

This chapter discusses a distributed adjustable power reserve control for a cluster of PV sources to enhance grid resiliency towards source and load side fluctuations. The proposed control ensures a constant PV power fed to the grid irrespective of fluctuations observed in the solar irradiation profiles. The PV power fluctuations are mitigated by utilizing the distributed power reserve within the PV cluster. This minimizes the size of expensive ESS required in the MG and also increases its service lifetime.

Furthermore, the adjustable power reserve can be dynamically adjusted by the grid operator to mitigate voltage or frequency fluctuations arising in the grid due to sudden load variations. Thus, the implemented algorithm provides flexibility for grid operator to autonomously adjust the PV clusters power generation. This facilitates the evolution of the conventional grid towards a more resilient grid considering high penetration of PV sources with limited requirement of costly energy storage. Results obtained from the HIL implementations on Typhoon HIL 402 emulator as well as a hardware validation on GaN based dc-dc boost converter authenticate the practical implementation of the proposed adjustable power reserve control.

Chapter 4 - Hybrid Power Ramp Rate Control

4.1 Motivation

In the previous chapter, an adjustable distributed power reserve control for a cluster of PV sources is discussed. This scheme enables the mitigation of source side fluctuations by feeding a set amount of PV power to the grid, irrespective of the fluctuations in the solar irradiation. Furthermore, it has been investigated in literature [125-129] that the rate of change of PV injected power, termed as ramp-rate; plays a vital role in voltage and frequency regulation in a high PV penetrated grid. For a high PV dominated grid, there is a risk of large ramp rates which can damage the grid frequency balance [130]; thereby drifting the MG/grid towards potentially instability [125, 128, 129]. In small power systems such as islands, the intermittent PV power can cause harmonic distortion and even blackouts [131]. Hence power ramp rate control (PRRC) schemes are crucial in maintaining the MG/grid stability for a high level of PV penetration [126]. In fact, various countries including Denmark [112], Germany [132], Puerto Rico [133] and United States [134] have recommended PRRC in their grid codes and have imposed strict bounds on the ramp-rates of PV power injection in their grid [125].Typically, a maximum ramp-rate of 10% of the PV system rated power per minute is deemed permissible by these codes [132, 133]. To cope with the PRRC constraints for PV systems, various control methods have been discussed in literature. These include control schemes using energy storages [127, 129] or via active power curtailment (APC) [107, 125].

4.2 Ramp rate control using energy storage systems

ESS based control strategies are the most commonly deployed PRRC methods where the excess PV energy is stored in a storage device to regulate the power ramp rate [129]. Various

ESS technologies including the electric double-layer capacitor [127], superconducting magnetic energy storage [135], fuel cells [136], and battery energy storage [137] have been proposed for smoothing the PV power. However, their costly deployment and maintenance coupled with the limited life-span and frequent replacement requirements make them not so economically viable. Besides, these ESSs need to be equipped with additional state of charge (SoC) controllers for efficient operation during the ramp-up as well as ramp-down fluctuations. This increases the computational complexity of the system [128]. Several works have also been proposed to simplify these controls and optimize the ESS capacity for efficient PRRC operation [128, 129, 137].

In [128], the authors propose a short-term forecasting-based scheme that minimizes the ESS's size to a quarter of the energy capacity, but at the cost of additional sensors and complex computations. Various other advanced techniques using cloud motion vector detection (CMVD) and cloud shadow motion vector detection (CSMVD) have also been proposed to deduce the solar irradiation profile on ground level [138, 139]. This vector information can be used for smoothing the PV output power as discussed in [140]. An alternative technique using ground-based sensor forecasting system (GBSFS) has also been discussed in [141]. In contrast to the above techniques, a much simpler approach to regulate the ramp-rate involving disconnecting some of the PV panels to reduce the generated power and regulate ramp-rate has been proposed in [125]. However, this approach is not feasible for low power residential installations with limited rooftop PV capabilities. Besides, a sudden disconnection of PV panels might rather introduce additional spikes in the output power. Furthermore, this scheme requires a centralized control with communication link to each PV inverter thereby increasing the overall system complexity.

4.3 Ramp rate control using active power curtailment techniques

On the contrary, active power curtailment (APC) is a cost-effective, conventional PRRC technique where the power fluctuations are suppressed by regulating the PV operation set-point away from the MPP [125, 142, 143]. Here, the PV sources track the power reference dictated to them by a ramp-rate measurement (RRM) block. In [127], an APC based PRRC scheme is proposed where the PV operating set-point is obtained from a gradient-descent optimizer. However, this scheme suffers from large power fluctuations and high computational burden due to the optimization process. Further, the authors of [142] propose an APC based scheme where the PV power ramp-rate is controlled by regulating the operation point away from the MPP. A similar work has been proposed in [125], where the PV operation point is always maintained on the left side of the MPP; so as to avoid open circuit (OC) conditions arising from steep solar irradiation variations. However, this scheme is effective only for power ramp-up scenarios and proves ineffective for steep drops in the PV power level. This occurs due to the absence of external energy source to feed the deficit power and maintain the ramp-rate; in the grid–tied inverter setup considered. This issue can be addressed by connecting the PV sources in clusters as discussed in Chapter 3. Furthermore, a distributed hybrid control strategy implemented on these PV clusters can enable PRRC functionality; even during ramp-down scenarios.

4.4 Proposed power ramp rate control technique

Here, the adjustable power reserve control strategy suggested in the Chapter 3 has been modified in order to regulate the ramp-rate of the PV power injected into the dc MG. Hence, a hybrid constant power generation - power ramp rate control (CPG-PRRC) strategy is proposed here which can regulate the rate of change of PV power during steep variations in the incident

solar irradiation. The proposed control scheme can maintain the ramp-rate dictated by the system operator during power ramp-up as well as power ramp-down scenarios. During the ramp-up condition, the MPPT-PRRC configured PV strings curtail the PV cluster power by following the APC principle and operating in PRRC mode. During the ramp-down condition, the deficient power needed to maintain the desired ramp-rate is extracted from the MPPT-CPG configured PV strings highlighted in the purple box of PV cluster 1 in the Fig. 4.1. The proposed PV system

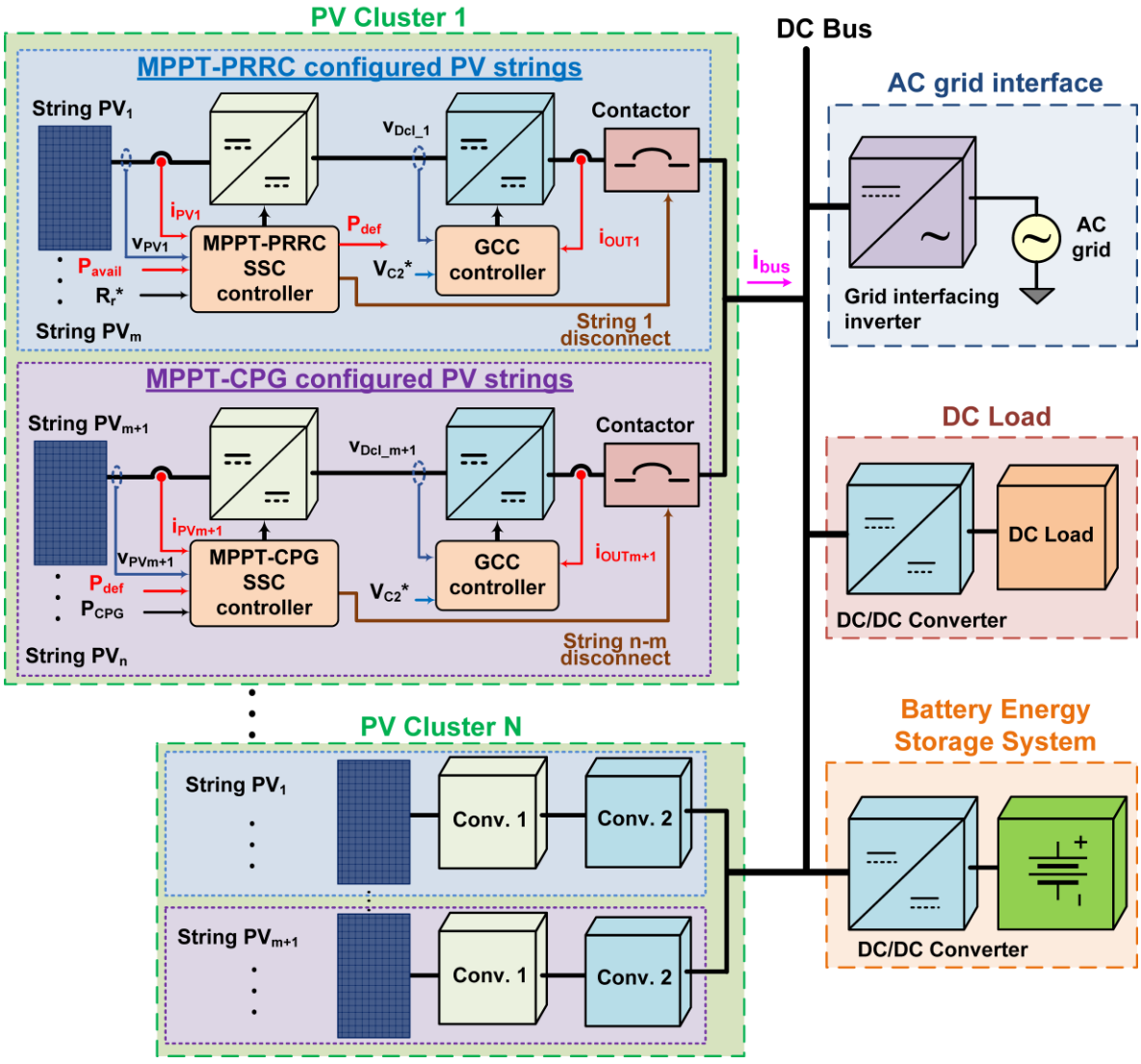

Fig. 4.1. Candidate architecture of '*N* ' PV clusters incorporating the proposed CPG-PRRC control scheme

architecture and control can be implemented on any existing PV system and does not require any extra hardware. Besides, it eliminates the need of an ESS to maintain the ramp-rate during the ramp-down scenarios as far as the PV cluster power reserve bounds are maintained.

4.5 System description

The discussed control scheme supplies the dc MG with ramp-rate limited PV power, irrespective of the steep variations in the incident solar irradiation. Fig. 4.1 illustrates the overall system and the proposed hybrid MPPT-CPG and MPPT-PRRC controllers implemented in each PV cluster. Each PV cluster consists of 'N' shunt connected PV strings. A PV string is made up of two cascaded dc-dc converters namely: source-connected converter (SCC) and grid-connected converter (GCC); each equipped with their independent control strategies. The SCC is connected to the PV panels and is responsible for extracting PV power as per the hybrid CPG-PRRC strategy. The second dc-dc converter connected to the dc bus mitigates any current mismatches that may arise among the 'N' shunt connected PV strings; especially during the solar irradiation mismatch conditions. Besides, it also boosts the PV string voltage to match the dc bus voltage. The GCC's design is adapted from [26]. A bi-directional MPC based inverter (discussed in Chapter 2) interconnects the dc bus to the ac grid. The grid operator dictates the ramp-rate limit 'R_r^*' as well as the 'P_{CPG}' limits for the MPPT-CPG configured SCC's. Besides, various local dc loads are also connected to the dc bus via interfacing dc-dc converters. The maximum available power 'P_{avail}' is obtained from a MPPT detector. The ESS used in the dc MG is deployed to feed power to the local loads only during ac grid failures and under extremely low solar irradiance conditions when the PV sources cannot generate sufficient power. It is noteworthy that the discussion is limited to the hybrid CPG-PRRC control for one PV cluster.

4.6 Power ramp rate measurement

The concept of power ramp rate measurement (PRRM) as proposed in [125] plays a key role in the power ramp rate control (PRRC) operation. The ramp rate for a PV source is the difference in PV power 'ΔP_{PV}' within time period 'T_{RRM}', given by (4.1)- (4.2).

$$R_r(t) = \frac{dP_{PV}}{dt} = \frac{P_{PV}(t+T_{RRM}) - P_{PV}(t)}{T_{RRM}} \quad (4.1)$$

$$= \frac{P_{PV}(t+wT_S) - P_{PV}(t)}{wT_S} \quad (4.2)$$

Here, $R_r(t)$ is the estimated ramp-rate, '$P_{PV}(t)$' is the PV power, 'w' is the window size, 'T_S' and 'T_{RRM}' are the MPPT and the RRM sampling periods respectively. Based on the conclusions presented in [125], the most optimal performance is achieved with 'w' set to 25.

4.7 Hybrid constant power generation – power ramp rate control scheme

The proposed hybrid CPG-PRRC strategy is a modified MPPT control scheme that adjusts the individual operation set-points of each PV string in the PV cluster so as to limit the active power or extract deficit power. This ensures that the ramp-rate of the power fed by the PV cluster to the dc MG is maintained within the limit irrespective of irradiation fluctuations. Here, the incremental conductance based MPPT algorithm forms the basis for the proposed scheme [26]. In a PV cluster, each SCC is configured in either the maximum power point tracking - power ramp rate control (MPPT-PRRC) configuration or the maximum power point tracking - constant power generation (MPPT-CPG) configuration. The system operator decides the default configuration for each SCC. Accordingly, out of the total 'n' SCCs in a PV cluster, atleast 'm' strings are configured with the MPPT-PRRC configuration. The remaining '$n-m$' SCCs operate in the MPPT-CPG configuration. For attaining efficient PRRC operation, atleast one SCC has to operate in MPPT-PRRC configuration ($m \geq 1$). The selection of 'm' depends on the

intensity and frequency of the solar irradiance fluctuations experienced in the specific geographical area. A detailed description of the two PV string configurations is given below.

4.7.1 Maximum power point tracking-power ramp rate control configuration:

In this configuration, the SCC is regulated as per the PRRC rule demonstrated in Fig. 4.2 and formulated by the relation (4.3) below:

$$P^{*}_{PVp\_\text{limit}} = \begin{cases} P^{*}_{PV\_\text{MPP}} & \text{when} \quad R_r(t) \le R^{*}_r \\ P^{*}_{PV\_PRRC} & \text{when} \quad R_r(t) > R^{*}_r \end{cases} \tag{4.3}$$

As far as the estimated ramp-rate '$R_r(t)$' lies within the ramp-rate limit 'R^{*}_r', the SCC operate in the MPPT mode thereby tracking the respective MPP. This is accomplished by making the SCC to track the reference power '$P^{*}_{PVp\_limit}$' equal to the instantaneous maximum power '$P^{*}_{PV\_MPP}$'. Thus, in this mode the maximum available PV power is fed to the dc bus. Once the estimated ramp-rate exceeds the ramp-rate limit 'R^{*}_r', the SCC's switch to PRRC mode and the PV operation set point is moved away from the MPP; typically to the left of the MPP to

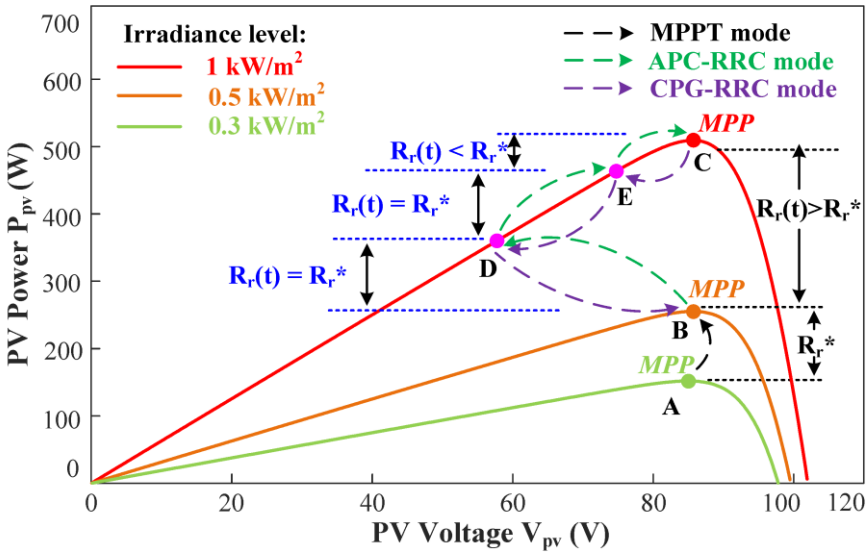

Fig. 4.2. Operation concept of hybrid CPG-PRRC algorithm based on incremental conductance MPPT technique

avoid PV source's open circuit operation. The PV power ramp-rate is regulated within 'R_r^*' by making the SCC track the new reference power '$P_{PV\_PRRC}^*$'. The value of '$P_{PV\_PRRC}^*$' is estimated based on the desired ramp-rate limit according to the relation given by (4.4). This limit is updated periodically by a differential power term 'ΔP', depending on the direction of variation of the solar irradiation 'J'.

$$P_{PV\_PRRC}^{*} = \begin{cases} P_{PV\_\text{limit\_old}} + \Delta P & \text{when } J \text{ increases} \\ P_{PV\_\text{limit\_old}} - \Delta P & \text{when } J \text{ decreases} \end{cases} \tag{4.4}$$

$$\Delta P = w R_r^* T_S \tag{4.5}$$

The differential power 'ΔP' given by (4.5) is the fractional power that needs to be added or deducted from the previous power reference; at every RRM sampling period. This periodic update in the PV power reference enables the SCC to regulate the estimated ramp-rate '$R_r(t)$' within the limit and attain efficient PRRC operation. For instance in the Fig. 4.2, while moving from point A (MPP at 0.3 kW/m^2) to point B (MPP at 0.5 kW/m^2), the ramp-rate is lower than the limit which is set to 150 W/s, hence MPP will be tracked during this transition. However, as the irradiation increases from 0.5 kW/m^2 to 1 kW/m^2, the rate of change of PV power exceeds the limit and hence the control will transition to point D and point E before finally reaching point C. This ensures that the ramp-rate is maintained within the limit.

During the solar irradiation steep ramp-up scenarios, the SCC can track this PRRC power reference provided by (4.3) by merely operating at non-MPP operation point. However, during the solar irradiation ramp-down scenarios, the instantaneous available PV power 'P_{avail}' is less than the PV power required to maintain the ramp-rate limit. This gives rise to a deficit power 'P_{def}' that cannot be compensated alone by the SCC of the MPPT-PRRC configured PV string. Under such conditions, the MPPT-PRRC configured SCCs switch to MPPT mode and harvest maximum available power. Thus, the output power from these PV strings declines following the

profile of the available power which can cause the entire PV cluster power's ramp rate to exceed the limit and the PRRC operation to fail [128]. However, the proposed hybrid CPG-PRRC control scheme leverages the benefits of the CPG functionality implemented for PV clusters in the previous chapter. It maintains the ramp-rate of the PV cluster output power by extracting additional power from the MPPT-CPG configured PV strings as discussed below.

4.7.2 Maximum power point tracking–constant power generation configuration:

As mentioned previously, the remaining '$n - m$' SCCs are configured for MPPT-CPG operation. A MPPT-CPG configured SCC is deployed to extract the excess PV power whenever needed; so as to maintain the ramp-rate of the PV cluster power within the limit and maintain PPRC operation. Under normal conditions, when the deficit power 'P_{def}' is zero, the MPPT-CPG configured SCCs operate in CPG mode. Here, they regulate the PV set-point to the left of the MPP and tracks the CPG power reference '$P^*_{PV\_CPG}$'. This power reference is decided by the operator based on various system and environmental parameters. In the event of a solar

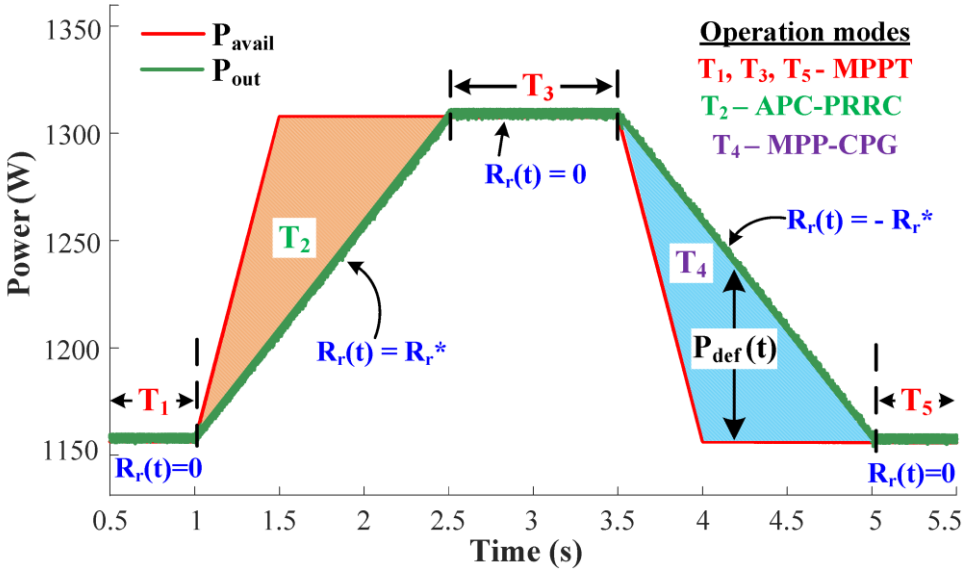

Fig. 4.3. Ramp rate of the PV power P_{out} is regulated within the limit R_r* as the available power changes steeply between 1150 W to 1350 W

irradiation ramp-down scenarios, the operation set-point of these SCC's is moved towards their respective MPP so as to harvest extra PV power. This set point adjustment is accomplished by dynamically appending the fractional power '$P_{def}/n-m$' to the CPG power reference '$P^{*}_{PV\_CPG}$' and making the SCC to track this updated power reference given by (4.6); shown by blue region in Fig. 4.3.

$$P^{*}_{PVc\_\text{limit}} = \begin{Bmatrix} P^{*}_{PV\_CPG} & \text{when } P_{def} = 0 \\ P^{*}_{PV\_CPG} + \dfrac{P_{def}}{(n-m)} & \text{when } P_{def} \neq 0 \end{Bmatrix} \tag{4.6}$$

The proposed hybrid CPG-PRRC algorithm for both configurations of the SCC controllers are summarized in Fig. 4.4 below. Based on the configuration of the PV string it will participate in ramp rate regulation during the ramp up scenario or during the ramp down scenario. In an MPPT-PRRC configured PV string, initially the PV string will operate in the MPPT mode to reach the MPP. This operation will continue until the rate of change of power injection is within the rate limit. As soon as the rate exceeds the ramp limit, the RRM block will start updating the power reference according to the relation (4.3) at each RRM interval. This process will continue until the ramp rate of available power exceeds the set limit. In this duration, the MPPT-CPG configured PV strings continue to operate in CPG mode, generating constant power.

In case, the available power on the MPPT-PRRC string is decreasing, the 'CPG_en' signal will be made high and the PV strings will now start increasing their harvested power by tracking the power reference generated by relation (4.6). The power reference for these strings will be increased or decreased until the ramp rate does not drop down within the specified rate limit. During this operation, the MPPT-PRRC configured PV string will operate in the MPPT mode so as to harvest maximum available power.

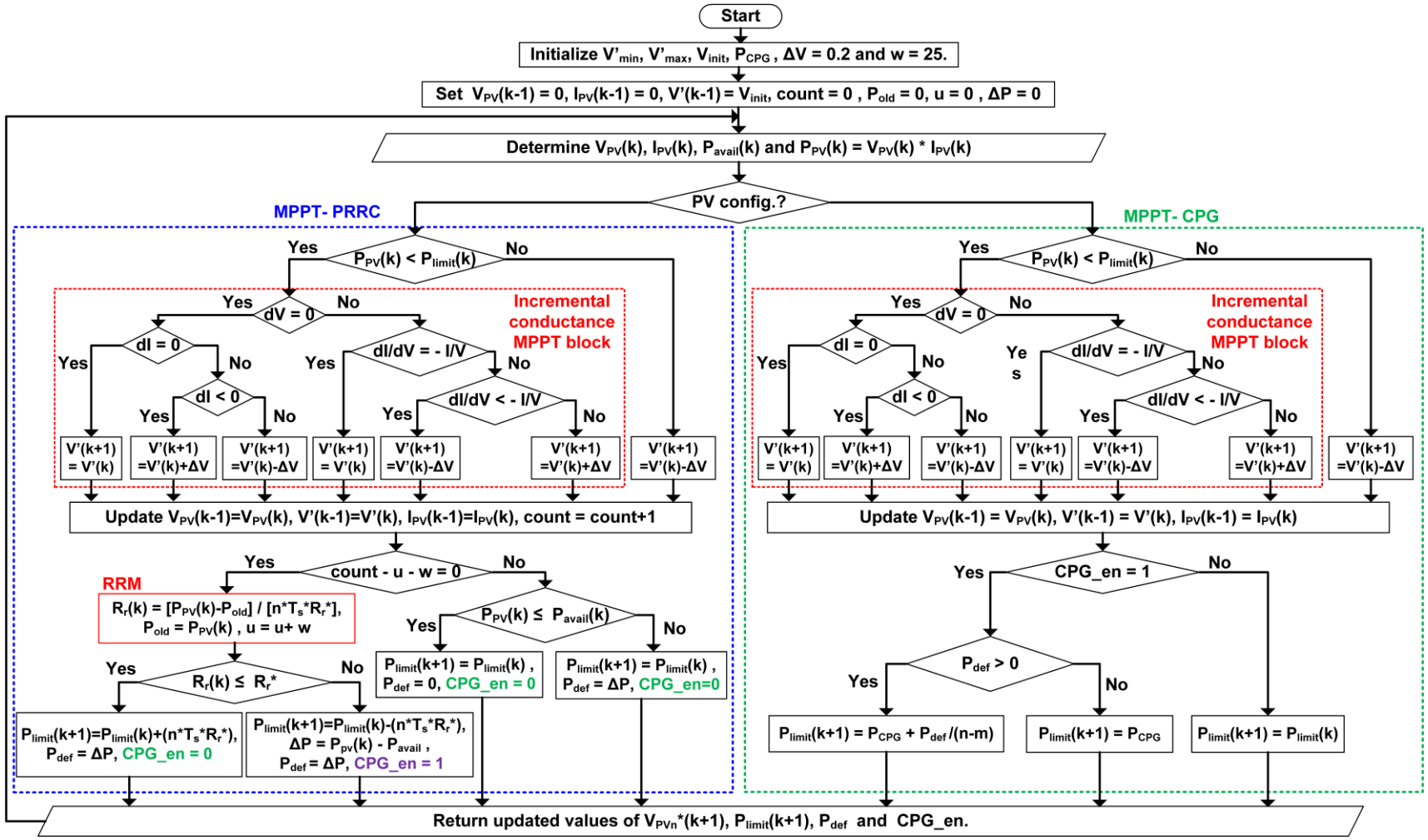

Fig. 4.4. Flowchart demonstrating the operation of the proposed hybrid CPG-PRRC algorithm

Table 4.1. CPG-PRRC governed PV cluster parameters

Symbol	Description	Value
$Z_{PV_{MPP}}$	Output impedance of each PV string at MPP	14.38 Ω
L_1, L_2	Input inductor of each converter	5 mH
C_1	SCC's output capacitor	960 µF
C_2	GCC's output capacitor	800 µF
f_{sw}	Switching frequency	20 kHz
$f_{s_{MPPT}}$	MPPT sampling frequency	10 kHz
V_{dc}	DC bus voltage	390 V
N_S	Number of strings in PV cluster	3
P_{MPP}	Maximum power per string	509.32 W
V_{OC}	Open-circuit voltage per string	102 V
V_{MPP}	MPP voltage for each PV string (STC)	85.6 V
I_{SC}	Short-circuit current for each PV string	6.3 A
I_{MPP}	MPP current for each PV string (STC)	5.95 A
P_{out}	Output power rating of each PV cluster	1.527 kW

4.8 Simulation results and discussion

In order to validate the performance of the proposed hybrid CPG-PRRC control, a PV cluster consisting of 3 strings namely 'PV_1', 'PV_2' and 'PV_3' are simulated in MATLAB Simulink environment. 'PV_1' operates in MPPT-PRRC configuration while 'PV_2' and 'PV_3' operate in MPPT-CPG configuration. Irrespective of their configuration, each PV string consists of two series connected SunPower SPR-X21-255 PV modules that collectively generate 509.32W P_{MPP} at 85.6 V V_{MPP} under STC ($1000W/m^2$, 25°C). The PV cluster parameters are listed in the Table 4.1. Since the proposed PV cluster has a maximum PV power rating of 1.5kW, the ramp-rate limit 'R_r^*' is chosen to be 150 W/s according to the specified norms. The distributed CPG-PRRC control scheme regulating the PV cluster feeds power to the dc bus within this preset ramp-rate.

To test the system performance, the control scheme is subjected to steep variations in the solar irradiation in Case Study 1 which represents shading from a fast-moving object. Next, the system is subjected to a gradually varying solar irradiation profile in Case Study 2 which represents a cloudy day scenario. Finally, Case Study 3 evaluates the system performance for highly fluctuating PV solar irradiation which represents a worst-case scenario of PV shading. For simplicity purposes, the solar irradiation on PV_2 and PV_3 is set constant at 1000 W/m^2 throughout the duration of all three case studies. Accordingly, the PV strings PV_2 and PV_3 configured in MPPT-CPG mode, generate a constant power of 400 W irrespective of the incident solar irradiation variations. To evaluate the system performance, PV_1 is subjected to steep ramp-rates. During a solar irradiation ramp-up scenario, PV_1 can single-handedly regulate the PV cluster power ramp-rate, while PV strings PV_2 and PV_3 continue to feed constant power. However, during ramp-down scenarios, PV_2 and PV_3 actively participate in regulating the PV cluster power ramp-rate, as evident from the following case studies.

4.8.1 Case Study 1:

In Case Study 1, the solar irradiance on PV_1 is initially maintained at 500 W/m^2 for which the PV cluster output power is a steady 1050 W for the entire time interval 'T_1'. Later at about t = 0.8 sec, the solar irradiance steeply increases to 1000 W/m^2 with a ramp-rate of 1000 W/sec. The Fig. 4.5 - Fig. 4.8 illustrates the complete scenario graphically. It is evident from Fig. 4.5 that the PV cluster output power 'P_{OUT}' initially increases with the set ramp-rate of 150 W/s until it reaches the new operating point. At about t = 2.4 sec, it reaches the new MPP and the PV cluster output power reaches to 1310 W at 1000 W/m^2; where it continues to operate until t = 3 sec. During the time interval from t = 2.4 sec to t = 3 sec, the SCC of PV_1 enters into PRRC mode and performs power curtailment to single-handedly regulate the ramp-up rate of the PV

cluster power within the limit of 150 W/sec. This ramp rate regulation is evident from the slowly rising output power of PV_1 indicated by the blue plot in Fig. 4.6. During the same time interval, the MPPT-CPG configured PV strings PV_2 and PV_3 operate in their CPG mode and continue to feed a constant power of 400 W to the dc MG.

Next, at t = 3 sec, the incident solar irradiation on PV_1 drops to 500 W/m^2 with a ramp down rate of 1000 W/sec. During this time, the SCC of PV_1 has no control over the ramp rate of the PV cluster output power and just follows the decreasing power profile. However, in this time interval 'T_4', the SCC's of PV strings PV_2 and PV_3 increase their harvested power by shifting their operation set-points towards the MPP and generating an additional power of 100 W each (indicated by purple and yellow plot in Fig. 4.6) to ensure the ramp-rate is maintained at the dc bus. The power harvested by PV_2 and PV_3 eventually drops back to 400 W following the desired ramp-rate of 150 W/s in time interval 'T_5'. After each PV string in the cluster has reached its new stable operation point, their SCCs switch back to MPPT mode and start tracking the power reference given by (4.4) and (4.6). The PV cluster output power returns to 1050 W with a ramp rate which is always less than or equal to the set limit of 150 W/sec.

The transition in operation modes of the PV strings and the shifts in the operation set-points of each PV string during the entire duration of Case Study 1 are also evident from the voltage and current dynamics shown in Fig. 4.7. Further, Fig. 4.8 also indicates that despite the large variations in PV_1 output current, the PV cluster current 'I_{bus}' fed to dc bus follows the set ramp-rate limit.

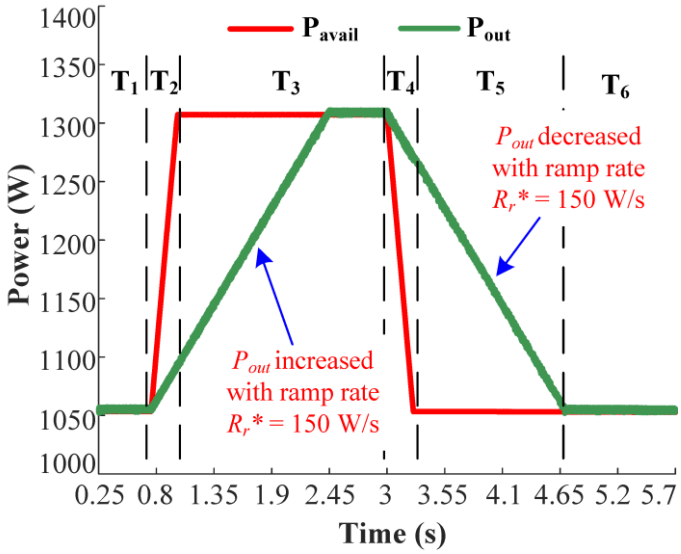

Fig. 4.5. P_{avail} rises steeply from 1050 W to 1310 W and goes back to 1050 W at ramp rate of 1000 W/sec, while P_{out} is regulated within the rate limit of 150 W/sec in Case Study 1

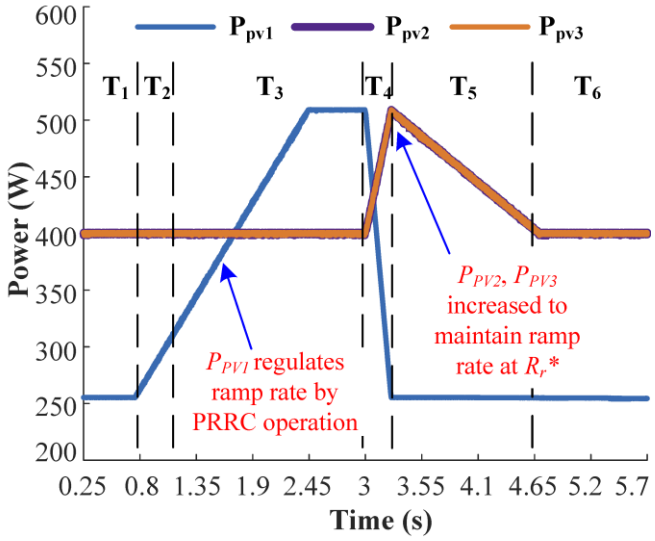

Fig. 4.6. P_{PV2}, P_{PV3} are increased to feed the deficit power and regulate the ramp rate within the set limit in Case Study 1

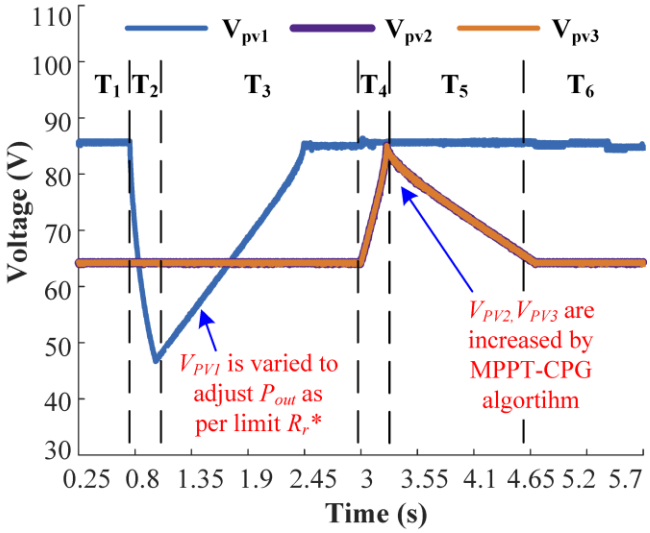

Fig. 4.7. V_{PV1} increases gradually during ramp-up scenario in T_3 to perform APC operation while V_{PV2} and V_{PV3} are increased during T_4 to regulate the ramp rate in Case Study 1

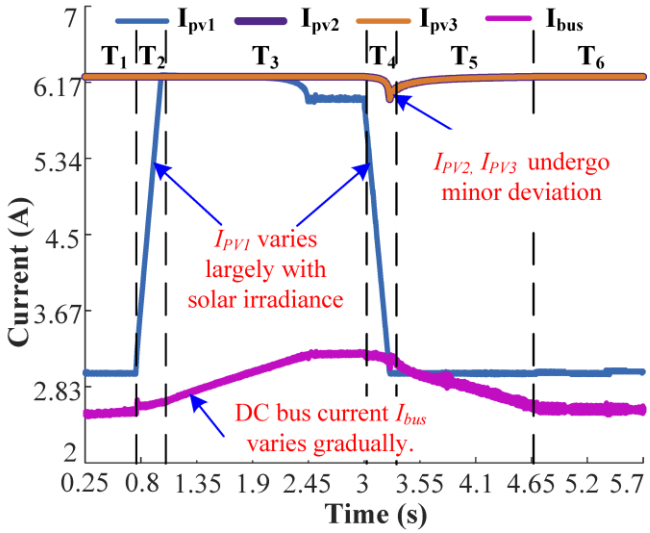

Fig. 4.8. PV cluster current I_{bus} injected into the dc bus changes gradually despite large variations in I_{PV1} in Case Study 1

4.8.2 Case Study 2:

In Case Study 2, the incident solar irradiance on PV_1 changes at various ramp-rates in different time intervals. The ramp rate limit 'R_r^*' is set to 150 W/sec. Initially during time interval 'T_1', with a constant incident solar irradiation of 500 W/m^2, the SCC's of each PV string operate in MPPT mode and regulate the PV cluster output power at 1050 W. From t = 0.53 sec to t = 1 sec (interval 'T_2'), the available power 'P_{avail}' denoted by red plot in Fig. 4.9, increases with a ramp-rate of 50 W/sec. Since this ramp-rate is less than the ramp-rate limit, the SCC's continue to operate in MPPT mode and follow the profile of the P_{avail}. Next, in time interval 'T_2' from t = 1 sec to t = 1.5 sec, the ramp-rate of 'P_{avail}' increases to 150 W/sec. Since the ramp-rate limit has not yet exceeded, no power curtailment is performed, and all SCC's in the PV cluster continue to operate in MPPT mode.

Furthermore, during time interval 'T_3' from t = 1.5 sec to t = 2.1 sec, 'P_{avail}' increases at a ramp-rate of 250 W/sec. Here since the ramp-rate limit is exceeded, PV_1 enters into PRRC mode and curtails the available power to regulate the ramp-rate within 150 W/sec, illustrated by blue plot in Fig. 4.10. This APC operation continues until about t = 2.45 sec, when the PV system reaches its new MPP and the solar irradiation is constant at 1000 W/m^2. Now during time interval 'T_4', all the SCC's operate in the MPPT mode until t = 3.25 sec. At t = 3.25 sec, 'P_{avail}' drops sharply to 35 W with irradiance level of 700 W/m^2. As shown in Fig. 4.10, during time interval 'T_5', PV_1 follows the decreasing profile of 'P_{avail}' while PV_2 and PV_3 increase their power generation by 50 W each to ensure the ramp-rate of the PV cluster power is retained within 150 W/sec. Towards the end of interval 'T_6' at about t = 4.1 sec, the dictated reference power overlaps with 'P_{avail}' and hence PV_2 and PV_3 return their power generation to

400W. Furthermore, the ramp-rate of 'P_{avail}' drops down to 150 W/sec and so the PV system follows the profile of 'P_{avail}' during interval 'T_7'.

At t = 4.65 sec, the ramp-rate of P_{avail} further drops to 50 W/sec. Thus during the time interval 'T_8', the PV cluster continues operating in MPPT mode and following the profile of P_{avail} with the reduced ramp-rate of 50 W/sec until t = 5.2 sec. Beyond, t = 5.2 sec, the solar irradiation drops and stays constant at 500 W/m^2 and hence the PV cluster feeds a constant power of 1050 W to the dc bus. The voltage and current dynamics of each PV string shown in Fig. 4.11 and Fig. 4.12 depict the operation modes and the respective shifts in the operation set-points of each SCC during the various time instances.

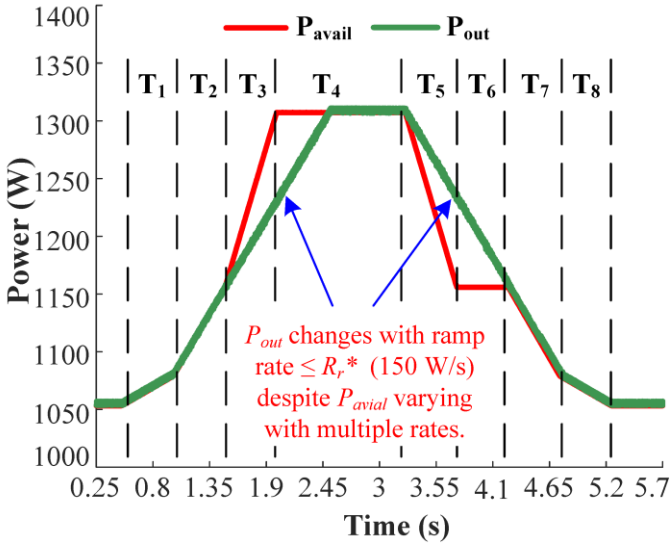

Fig. 4.9. P_{avail} changes with multiple rates (T_1, T_8: at 50 W/sec; T_2, T_7: at 150 W/sec; T_3, T_5: at 300 W/sec) while P_{OUT} is regulated at 150 W/sec in Case Study 2

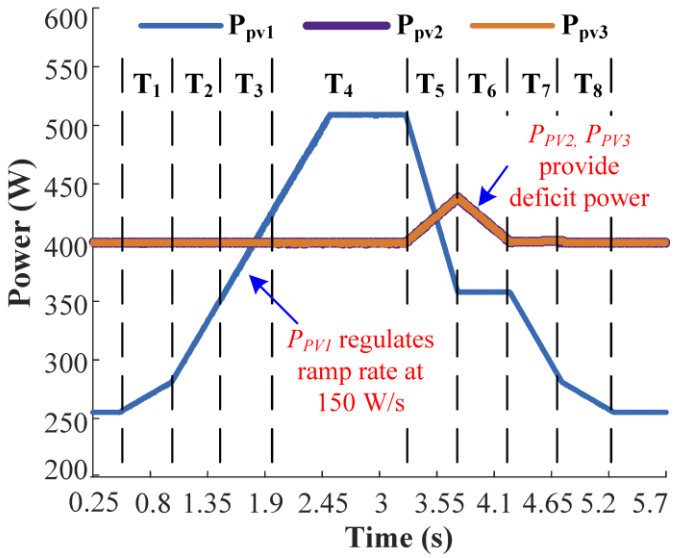

Fig. 4.10. PV_1 regulates the ramp rate by APC during ramp-up; P_{PV2} and P_{PV3} increase their powers to regulate ramp rate during ramp-down cases in Case Study 2

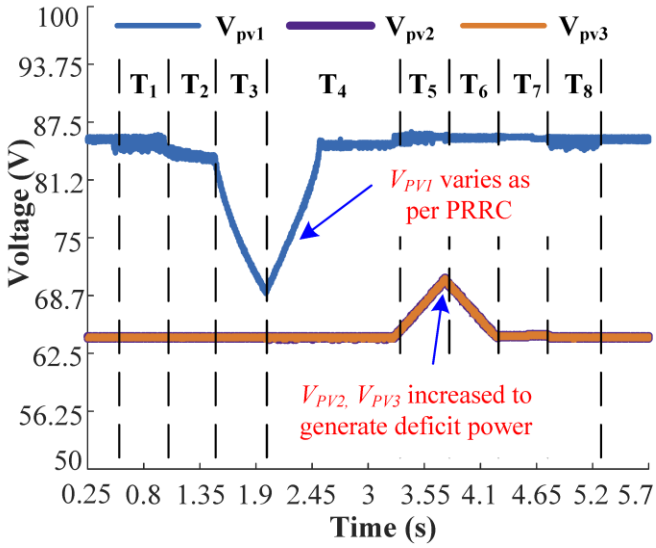

Fig. 4.11. V_{PV1} increases according to PRRC operation during ramp-up scenario in T_4; V_{PV2} and V_{PV3} increase during ramp-down scenario in T_5 and decrease during T_6 in Case Study 2

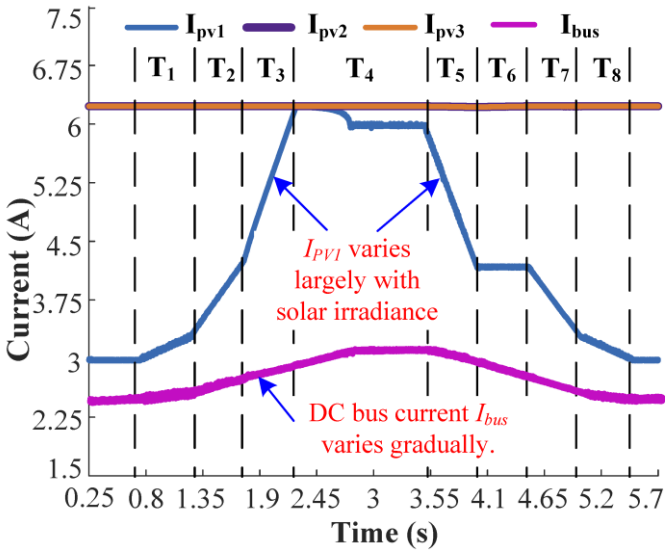

Fig. 4.12. Dynamics of I_{PV1}, I_{PV2}, I_{PV3}, I_{bus} when P_{avail} varies with multiple ramp rates in Case Study 2.

4.8.3 Case Study 3:

Finally, in Case Study 3, we evaluate the dynamic response of the proposed hybrid CPG-PRRC scheme to highly fluctuating PV irradiation conditions. Besides, here the ramp-rate limit for the PV system is changed to 50 W/sec; to validate the system compatibility to extremely low ramp-rates. Initially, the incident solar irradiance is held at 1000 W/m^2 and the PV cluster feeds a constant power of 1310 W to the dc bus. In time interval 'T_1' from t = 0.53 sec to t = 1.53 sec, the available PV power P_{avail} represented by red plot in Fig. 4.13 starts declining at a ramp-rate of 300 W/sec. In response, PV_2 and PV_3 increase their output powers proportionately until t = 1.53 sec, to regulate the ramp-rate within the set limit of 50 W/sec; as shown by purple and yellow plots in Fig. 4.14. Now, from t = 1.53 sec to t = 1.75 sec, P_{avail} remains constant at 1050 W and hence PV_2 and PV_3 decrease their generations; proportionate to the ramp-rate limit. From t = 1.75 sec to t = 1.97 sec, P_{avail} increases steeply at a rate of 800 W/sec. Here, PV_1 will

transition into the PRRC mode and start extracting power with a ramp-rate within the set limit of 50 W/sec (T_3 in Fig. 4.13), while PV_2 and PV_3 return their power generation to 400 W. After the new MPP limit is attained at t = 2 sec, all the units move into MPPT mode and track the available constant power until t = 2.7 sec. During this duration, PV_2 and PV_3 are operating in the CPG mode and are generating a constant power of 400 W.

Next, in time interval 'T_4' from t = 2.7 sec to t = 3.12 sec, P_{avail} again drops down to 1100 W with a ramp-rate of 600 W/sec. To regulate the ramp-rate of the PV cluster power fed to the dc bus, at t = 3.12 sec PV_2 and PV_3 increase their harvested power by 175 W each. Since the available power remains constant at 1100 W until t = 3.5 sec, the power generation from PV_2 and PV_3 again decreases back to 400 W as per the rate of 150/2 = 75 W/sec given by relation (4.6). Finally, P_{avail} increases form 1100 W at t = 3.5 sec to 1310 W at t = 4 sec with a steep ramp-rate of 400 W/sec. The PV cluster again starts increasing its dc bus injected power at the preset ramp-rate limit of 50 W/s as PV_1 transitions into PRRC mode while PV_2 and PV_3 return to CPG operation mode from t = 4 sec to t = 5.75 sec (time interval 'T_7' in Fig. 4.13). Beyond t = 5.75 sec, the PV system has already reached its steady state and now starts feeding constant power of 1310 W to the dc bus with PV_2 and PV_3 generating constant power of 400 W in the CPG mode and PV_1 operating in the MPPT mode.

The transitions in the operation modes of each PV string along with the adjustments in the PV operation set-points are evident from the voltage profiles of the PV strings shown in Fig. 4.15. Besides, the Fig. 4.16 shows that the dc MG current 'I_{bus}' does not face significant fluctuations despite the large variations seen in the plot of I_{PV1}. Throughout the duration of Case Study 3, the ramp rate of the PV power fed to the dc MG is regulated within the ramp-rate limit of 50 W/sec, thereby ensuring successful PRRC operation.

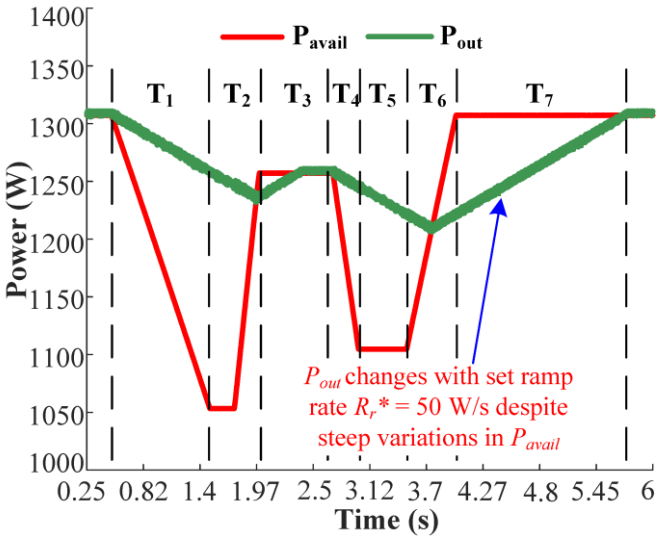

Fig. 4.13. Ramp rate of P_{OUT} regulated at 50 W/sec under highly fluctuating available power P_{avail} (with large ramp rates) in Case Study 3

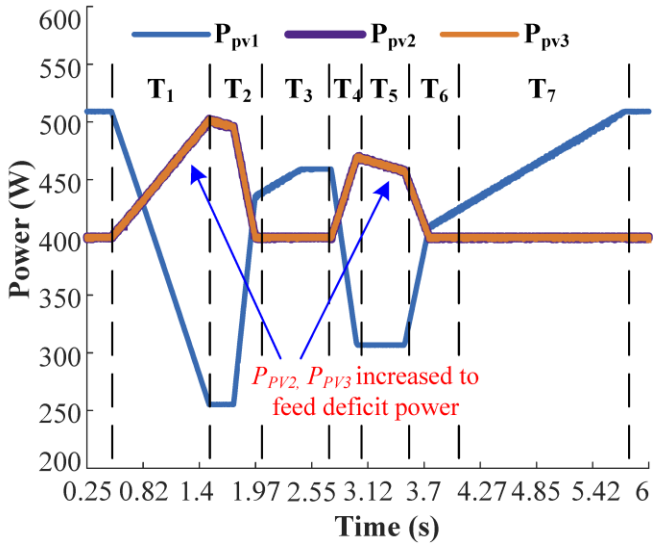

Fig. 4.14. MPPT-CPG configured P_{PV2} and P_{PV3} increase their powers to regulate the ramp rate each time a ramp-down condition occurs in Case Study 3

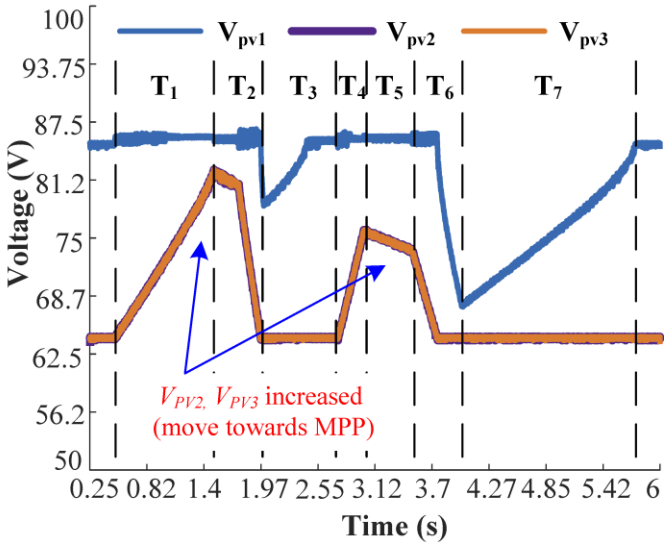

Fig. 4.15. Output voltage profiles of PV_1, PV_2 and PV_3 during highly fluctuating incident solar irradiance on PV_1 in Case Study 3

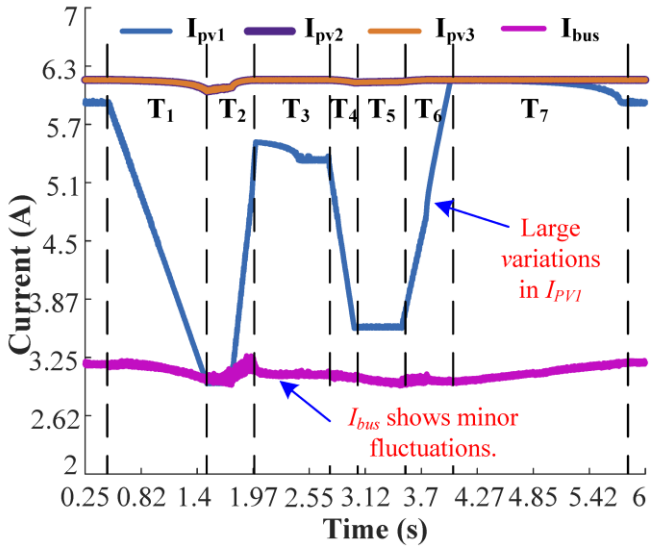

Fig. 4.16. Low variations I_{bus} despite the large deviations in I_{PV1} in Case Study 3

4.9 Conclusion and remarks

In this chapter, a hybrid CPG-PRRC control scheme to regulate the ramp-rate of PV cluster power injected to the MG/grid is proposed. The proposed scheme is capable of tracking extremely low ramp-rates under highly fluctuating solar irradiation pattern and does so without the need of an ESS as far as the system power reserve limits are maintained. It thus provides a cost-effective solution to mitigate the voltage fluctuations and grid instabilities experienced due to source side fluctuations in a highly PV penetrated grid. The proposed control can be deployed on existing PV architecture and does not require any additional hardware. This makes its deployment in existing grid tied PV plants convenient and facilitates the smooth transition of the conventional power grid into a highly renewable generation based clean and green grid of the future. The next chapter will leverage all the control strategies proposed so far to develop the architecture of the grid friendly PV system which is the aim of this thesis.

Chapter 5 - Conclusion and Future Work

This chapter proposes a summary of the work done in this thesis. This chapter also includes suggestions for the future utilization of the proposed control for multi-tiered autonomous voltage-frequency control for a fleet of inverters into the grid/MG. Section 5.1 presents a summary of the thesis and Section 5.2 presents the future work suggestions.

5.1 Summary

The major contribution of this thesis is the development of a grid friendly PV system using autonomous power reserve functionality. The experimental results verify the deployment of a MPC based inverter control scheme that enables seamless connection /disconnection of a PV cluster to the ac grid along with adjustable active and reactive power injection capabilities.

Furthermore, an adjustable PV power reserve functionality for a PV cluster architecture has been proposed to mitigate the short-term power transients in the PV output power. The proposed power reserve scheme is further adapted to provide regulated injection of PV power within a specified ramp rate. This regulated PV power injection ensures voltage and frequency balance in the MG/grid and helps maintain the system stability.

Moreover, the adjustable PV power reserve in the PV clusters enables the grid operator to autonomously adjust the PV clusters power generation in response to an event. This facilitates the evolution of the conventional grid towards a more resilient grid considering high penetration of PV sources with limited requirement of costly energy storage.

5.2 Future work

The adjustable power reserve for PV clusters will be further extended to implement a multi-tiered autonomous voltage-frequency control for a fleet of inverters in a power electronics dominated grid. The proposed PV cluster dominated MG architecture is as illustrated in the Fig. 5.1. Here, a hierarchical control architecture is utilized in the proposed system. The MPC based inverter control (discussed in Chapter 2) and the hybrid CPG-PRRC based PV cluster control (discussed in Chapter 3 and Chapter 4) will be deployed as the primary layer controllers. The MPC operated inverter will integrate the PV cluster to the MG with seamless connection/ disconnection abilities. Furthermore, this inverter will also be capable of regulating its active and reactive power injection into the grid, in response to the supervisory controller's command. Similarly, the hybrid CPG-PRRC controller will ensure the implementation of adjustable PV power reserve in the PV strings in response to the reserve ratios dictated by the supervisory controller.

An artificial neural network (ANN) based supervisory controller will be deployed as the upper layer control and will act as an optimizer for the MG. It shall determine the optimum set-point of each PV cluster and its interfacing inverter. The main objectives of the ANN based supervisory controller shall include minimizing the power loss, optimizing the power reserve in the CPG configured PV strings. Besides, it will determine the operation configuration of each PV string and optimize the reactive power flow according to the inverters' physical capabilities. The supervisory controller shall thus optimize the PV utilization, loading on the grid, and minimize the distribution losses. Using the historical weather data and the frequency deviations observed in the MG, the supervisory controller will determine the operation configuration of each PV string and forecasts the power reserve needed to handle event-triggered attacks. Thus, the

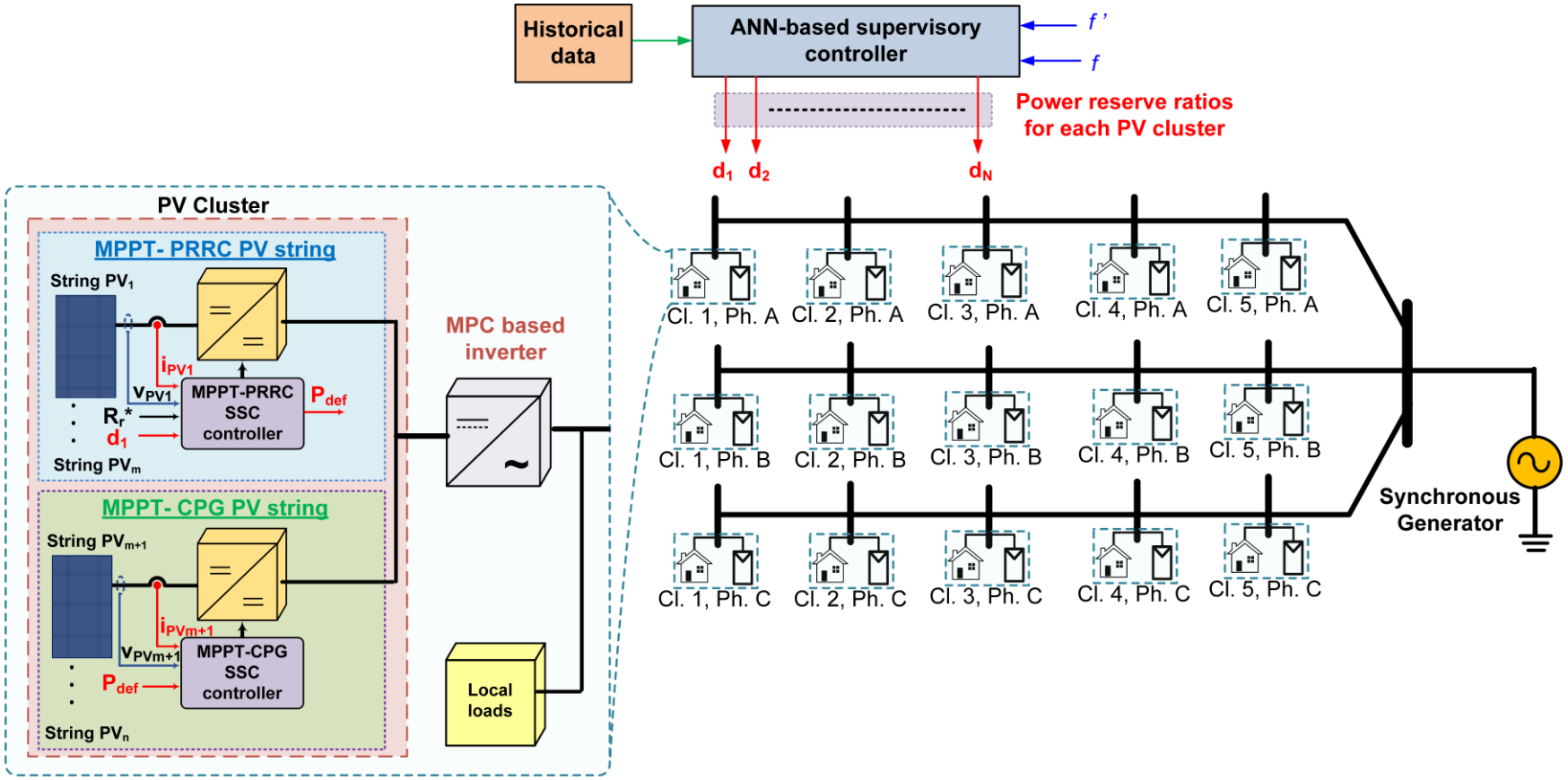

Fig. 5.1. A PV cluster dominated MG

proposed control architecture will provide the grid with the required PV power for grid support functions during failures and cyber-attack scenarios.

The proposed PV cluster dominated MG architecture will enhance the resiliency of the system to instabilities arising from source side and grid side power fluctuations as well as to intended cyber-attacks while limiting the need of costly ESSs. The above discussed multi-tiered autonomous voltage-frequency control for a fleet of inverters in a power electronics dominated grid will be implemented and validated experimentally by the author as part of his future work.

References

[1] A. Smith, "2010–2019: A landmark decade of US. billion-dollar weather and climate disasters," *National Oceanic and Atmospheric Administration*, 2020.

[2] S. D'silva, P. Nanduri, S. Jain, F. Fateh, M. B. Shadmand, and B. Mirafzal, "Autonomous Power Reserve Control for Cluster of Photovoltaic Sources in Microgrids," in *IEEE Applied Power Electronics Conference and Exposition (APEC)*, 2019.

[3] A. Kwasinski, W. Weaver, and R. S. Balog, *Microgrids and other local area power and energy systems*. Cambridge University Press, 2016.

[4] H. A. Sher, A. F. Murtaza, A. Noman, K. E. Addoweesh, K. Al-Haddad, and M. Chiaberge, "A new sensorless hybrid MPPT algorithm based on fractional short-circuit current measurement and P&O MPPT," *IEEE Transactions on Sustainable Energy*, vol. 6, no. 4, pp. 1426-1434, 2015.

[5] M. Metry, M. B. Shadmand, R. S. Balog, and H. A. Rub, "A variable step-size MPPT for sensorless current model predictive control for photovoltaic systems," in *IEEE Energy Conversion Congress and Exposition (ECCE)* 2016.

[6] A. Khan, M. Hosseinzadehtaher, M. B. Shadmand, S. Bayhan, and H. Abu-Rub, "On Stability of Power Electronics Dominated Grid," *IEEE Industrial Electronics Magazine*, 2020, doi: 10.1109/MIE.2020.3002523.

[7] H. S. A. Poon, "Clustered power generator architecture," ed: Google Patents, 2020.

[8] S. D'silva, M. Shadmand, S. Bayhan, and H. Abu-Rub, "Towards Grid of Microgrids: Seamless Transition between Grid-Connected and Islanded Modes of Operation," *IEEE Open Journal of the Industrial Electronics Society*, 2020.

[9] M. B. Shadmand, R. S. Balog, and M. D. Johnson, "Predicting Variability of High-Penetration Photovoltaic Systems in a Community Microgrid by Analyzing High-Temporal Rate Data," *IEEE Transactions on Sustainable Energy*, vol. 5, no. 4, pp. 1434-1442, 2014, doi: 10.1109/TSTE.2014.2345745.

[10] M. B. Shadmand and R. S. Balog, "Multi-Objective Optimization and Design of Photovoltaic-Wind Hybrid System for Community Smart DC Microgrid," *IEEE Transactions on Smart Grid*, vol. 5, no. 5, pp. 2635-2643, 2014, doi: 10.1109/TSG.2014.2315043.

[11] M. N. Arafat, A. Elrayyah, and Y. Sozer, "An effective smooth transition control strategy using droop-based synchronization for parallel inverters," *IEEE Transactions on Industry Applications*, vol. 51, no. 3, pp. 2443-2454, 2014.

[12] T. Dragičević, X. Lu, J. C. Vasquez, and J. M. Guerrero, "DC microgrids—Part II: A review of power architectures, applications, and standardization issues," *IEEE transactions on power electronics*, vol. 31, no. 5, pp. 3528-3549, 2015.

[13] X. Liu, M. Shahidehpour, Z. Li, X. Liu, Y. Cao, and Z. Bie, "Microgrids for enhancing the power grid resilience in extreme conditions," *IEEE Transactions on Smart Grid*, vol. 8, no. 2, pp. 589-597, 2016.

[14] M. Smith and D. Ton, "Key connections: The us department of energy? s microgrid initiative," *IEEE Power and Energy magazine*, vol. 11, no. 4, pp. 22-27, 2013.

[15] M. B. Shadmand, R. S. Balog, and H. Abu-Rub, "Model predictive control of PV sources in a smart DC distribution system: Maximum power point tracking and droop control," *IEEE Transactions on Energy Conversion*, vol. 29, no. 4, pp. 913-921, 2014.

[16] S. D'silva, A. Khan, M. F. Umar, M. B. Shadmand, and H. Abu-Rub, "On Stability of Hybrid Power Ramp Rate Control for High Photovoltaic Penetrated Grid," in *IEEE Energy Conversion Congress and Exposition (ECCE)*, 2020, pp. 2806-2813.
[17] A. Y. Fard and M. B. Shadmand, "Cooperative Model Predictive Control Scheme for Dispersed Smart Inverters at the Grid Edge," in *IEEE Texas Power and Energy Conference (TPEC)*, 2020.
[18] A. Y. Fard, M. B. Shadmand, and S. K. Mazumder, "Holistic Multi-timescale Attack Resilient Control Framework for Power Electronics Dominated Grid," in *2020 Resilience Week (RWS)*, 19-23 Oct. 2020 2020, pp. 167-173, doi: 10.1109/RWS50334.2020.9241270.
[19] M. Easley, S. Jain, M. B. Shadmand, and H. A. Abu-Rub, "Autonomous Model Predictive Controlled Smart Inverter with Proactive Grid Fault Ride-Through Capability," *IEEE Transactions on Energy Conversion*, 2020.
[20] M. S. Pilehvar, M. B. Shadmand, and B. Mirafzal, "Analysis of smart loads in nanogrids," *IEEE Access*, vol. 7, pp. 548-562, 2018.
[21] A. Barzkar and S. M. H. Hosseini, "A novel peak load shaving algorithm via real-time battery scheduling for residential distributed energy storage systems," *International Journal of Energy Research*, vol. 42, no. 7, pp. 2400-2416, 2018.
[22] A. Mohammed, S. S. Refaat, S. Bayhan, and H. Abu-Rub, "AC Microgrid Control and Management Strategies: Evaluation and Review," *IEEE Power Electronics Magazine*, vol. 6, no. 2, pp. 18-31, 2019.
[23] T. Dragičević, X. Lu, J. C. Vasquez, and J. M. Guerrero, "DC microgrids—Part I: A review of control strategies and stabilization techniques," *IEEE Transactions on power electronics*, vol. 31, no. 7, pp. 4876-4891, 2015.
[24] S. Liu, P. X. Liu, and X. Wang, "Stability analysis of grid-interfacing inverter control in distribution systems with multiple photovoltaic-based distributed generators," *IEEE Transactions on Industrial Electronics*, vol. 63, no. 12, pp. 7339-7348, 2016.
[25] S. Liu, P. X. Liu, and X. Wang, "Stochastic small-signal stability analysis of grid-connected photovoltaic systems," *IEEE Transactions on Industrial Electronics*, vol. 63, no. 2, pp. 1027-1038, 2015.
[26] A. Khan, S. D'silva, A. Y. Fard, M. B. Shadmand, and H. A. Abu-Rub, "On Stability of PV Clusters with Distributed Power Reserve Capability," *IEEE Transactions on Industrial Electronics*, 2020.
[27] A. Khan, M. B. Shadmand, S. Bayhan, and H. Abu-Rub, "A Power Ripple Compensator for DC Nanogrids via a Solid- State Converter," *IEEE Open Journal of the Industrial Electronics Society*, 2020, doi: 10.1109/OJIES.2020.3035073.
[28] I. J. Balaguer, Q. Lei, S. Yang, U. Supatti, and F. Z. Peng, "Control for grid-connected and intentional islanding operations of distributed power generation," *IEEE transactions on industrial electronics*, vol. 58, no. 1, pp. 147-157, 2010.
[29] S. Jain, M. B. Shadmand, and R. S. Balog, "Decoupled active and reactive power predictive control for PV applications using a grid-tied quasi-Z-source inverter," *IEEE Journal of Emerging and Selected Topics in Power Electronics*, vol. 6, no. 4, pp. 1769-1782, 2018.
[30] M. Easley, S. Jain, M. B. Shadmand, and H. Abu-Rub, "Computationally efficient distributed predictive controller for cascaded multilevel impedance source inverter with LVRT capability," *IEEE Access*, vol. 7, pp. 35731-35742, 2019.

[31] C.-L. Chen, Y. Wang, J.-S. Lai, Y.-S. Lee, and D. Martin, "Design of parallel inverters for smooth mode transfer microgrid applications," *IEEE Transactions on Power Electronics*, vol. 25, no. 1, pp. 6-15, 2009.
[32] R. S. Balog, M. Metry, and M. Shadmand, "The load as a controllable energy asset in dc microgrids," in *Energy Engineering, DC Distribution Systems and Microgrids*: Institution of Engineering and Technology, 2018, pp. 153-187. [Online]. Available: http://digital-library.theiet.org/content/books/10.1049/pbpo115e_ch7
[33] M. Hosseinzadehtaher, A. Khan, M. Easley, M. B. Shadmand, and P. Fajri, "Self-healing Predictive Control of Battery System in Naval Power System with Pulsed Power Loads," *IEEE Transactions on Energy Conversion*, 2020.
[34] M. Hosseinzadehtaher, A. Khan, M. W. Baker, and M. B. Shadmand, "Model Predictive Self-healing Control Scheme for Dual Active Bridge Converter," in *2nd International Conference on Smart Grid and Renewable Energy (SGRE)*, 2019.
[35] Y. Sun, X. Hou, J. Yang, H. Han, M. Su, and J. M. Guerrero, "New perspectives on droop control in AC microgrid," *IEEE Transactions on Industrial Electronics*, vol. 64, no. 7, 2017.
[36] S. M. Ashabani and Y. A.-r. I. Mohamed, "New family of microgrid control and management strategies in smart distribution grids—analysis, comparison and testing," *IEEE Transactions on Power Systems*, vol. 29, no. 5, pp. 2257-2269, 2014.
[37] S. Kumar and B. Singh, "Seamless Operation and Control of Single-Phase Hybrid PV-BES-Utility Synchronized System," *IEEE Transactions on Industry Applications*, vol. 55, no. 2, pp. 1072-1082, 2018.
[38] D. E. Olivares *et al.*, "Trends in microgrid control," *IEEE Transactions on smart grid*, vol. 5, no. 4, pp. 1905-1919, 2014.
[39] Y. Han, H. Li, P. Shen, E. A. A. Coelho, and J. M. Guerrero, "Review of active and reactive power sharing strategies in hierarchical controlled microgrids," *IEEE Transactions on Power Electronics*, vol. 32, no. 3, pp. 2427-2451, 2016.
[40] J. M. Guerrero, J. C. Vasquez, J. Matas, L. G. De Vicuña, and M. Castilla, "Hierarchical control of droop-controlled AC and DC microgrids—A general approach toward standardization," *IEEE Transactions on industrial electronics*, vol. 58, no. 1, pp. 158-172, 2010.
[41] J. Wang, N. C. P. Chang, X. Feng, and A. Monti, "Design of a generalized control algorithm for parallel inverters for smooth microgrid transition operation," *IEEE Transactions on Industrial Electronics*, vol. 62, no. 8, pp. 4900-4914, 2015.
[42] A. Khan, M. Hosseinzadehtaher, M. B. Shadmand, D. Saleem, and H. Abu-Rub, "Intrusion Detection for Cybersecurity of Power Electronics Dominated Grids: Inverters PQ Set-Points Manipulation," in *IEEE CyberPELS*, 2020.
[43] A. Khan, M. Hosseinzadehtaher, and M. B. Shadmand, "Single Stage PLL-less Decoupled Active and Reactive Power Control for Weak Grid Interactive Inverters," in *IFAC World Congress*, Berlin, Germany, 2020.
[44] A. Khan, M. Easley, M. Hosseinzadehtaher, M. B. Shadmand, H. Abu-Rub, and P. Fajri, "PLL-less Active and Reactive Power Controller for Grid-Following Inverter," in *IEEE Energy Conversion Congress and Exposition (ECCE)*, 2020, pp. 4322-4328.
[45] M. F. Umar, A. Khan, M. Easley, S. D'Silva, B. Nun, and M. B. Shadmand, "Resonance Suppression based on Predictive Control of Grid-following Inverters with LCL Filter in

Weak Grid Condition," in *IEEE Energy Conversion Congress and Exposition (ECCE)*, 2020, pp. 4742-4748.

[46] S. Harshbarger, M. Hosseinzadehtaher, B. Natarajan, E. Vasserman, M. Shadmand, and G. Amariucai, "(A Little) Ignorance is Bliss: The Effect of Imperfect Model Information on Stealthy Attacks in Power Grids," in *2020 IEEE Kansas Power and Energy Conference (KPEC)*, 13-14 July 2020 2020, pp. 1-6, doi: 10.1109/KPEC47870.2020.9167599.

[47] M. Hosseinzadehtaher, A. Khan, M. B. Shadmand, and H. Abu-rub, "Anomaly Detection in Distribution Power System based on a Condition Monitoring Vector and Ultra-short Demand Forecasting," presented at the 2020 IEEE CyberPELS (CyberPELS), Miami, FL, USA, 2020.

[48] A. Khan, M. Hosseinzadehtaher, M. Easley, M. B. Shadmand, and H. Abu-Rub, "Decoupled Active and Reactive Power Control without PLL Requirement for Differential Buck Converter," in *2020 IEEE Energy Conversion Congress and Exposition (ECCE)*, 11-15 Oct. 2020 2020, pp. 4994-4999, doi: 10.1109/ECCE44975.2020.9235663.

[49] M. Easley, M. Hosseinzadehtaher, A. Y. Fard, M. B. Shadmand, and H. Abu-Rub, "Computationally-efficient Hierarchical Optimal Controller for Grid-tied Cascaded Multilevel Inverters," in *2019 IEEE Energy Conversion Congress and Exposition (ECCE)*, 29 Sept.-3 Oct. 2019 2019, pp. 219-224, doi: 10.1109/ECCE.2019.8912866.

[50] Z. Zhang, M. Easley, M. Hosseinzadehtaher, G. Amariucai, M. B. Shadmand, and H. Abu-Rub, "An Observer Based Intrusion Detection Framework for Smart Inverters at the Grid-Edge," in *2020 IEEE Energy Conversion Congress and Exposition (ECCE)*, 11-15 Oct. 2020 2020, pp. 1957-1962, doi: 10.1109/ECCE44975.2020.9235863.

[51] Z. Zhang, A. W. Oluwafemi, M. Hosseinzadehtaher, and M. B. Shadmand, "Current Observer Based Predictive Decoupled Power Control Grid-Interactive Inverter," in *2020 IEEE Texas Power and Energy Conference (TPEC)*, 6-7 Feb. 2020 2020, pp. 1-6, doi: 10.1109/TPEC48276.2020.9042581.

[52] M. Easley, A. Y. Fard, F. Fateh, M. B. Shadmand, and H. Abu-Rub, "Auto-tuned Model Parameters in Predictive Control of Power Electronics Converters," in *2019 IEEE Energy Conversion Congress and Exposition (ECCE)*, 29 Sept.-3 Oct. 2019 2019, pp. 3703-3709, doi: 10.1109/ECCE.2019.8912881.

[53] Q. Shafiee, J. M. Guerrero, and J. C. Vasquez, "Distributed secondary control for islanded microgrids—A novel approach," *IEEE Transactions on power electronics*, vol. 29, no. 2, pp. 1018-1031, 2013.

[54] A. Khan, M. Hosseinzadahtaher, M. B. Shadmand, S. Bayhan, and H. Abu-Rub, "On the Stability of the Power Electronics-Dominated Grid," *IEEE Industrial Electronics Magazine*, 2020, doi: 10.1109/MIE.2020.3002523.

[55] Q. Shafiee, Č. Stefanović, T. Dragičević, P. Popovski, J. C. Vasquez, and J. M. Guerrero, "Robust networked control scheme for distributed secondary control of islanded microgrids," *IEEE Transactions on Industrial Electronics*, vol. 61, no. 10, pp. 5363-5374, 2013.

[56] A. Y. Fard, M. Easley, G. T. Amariucai, M. B. Shadmand, and H. Abu-Rub, "Cybersecurity Analytics using Smart Inverters in Power Distribution System: Proactive Intrusion Detection and Corrective Control Framework," in *2019 IEEE International Symposium on Technologies for Homeland Security (HST)*, 5-6 Nov. 2019 2019, pp. 1-6, doi: 10.1109/HST47167.2019.9032978.

[57] M. Awal, H. Yu, H. Tu, S. Lukic, and I. Husain, "Hierarchical Control for Virtual Oscillator Based Grid-Connected and Islanded Microgrids," *IEEE Transactions on Power Electronics*, 2019.
[58] X. Hou *et al.*, "Distributed hierarchical control of AC microgrid operating in grid-connected, islanded and their transition modes," *Ieee Access*, vol. 6, pp. 77388-77401, 2018.
[59] A. Y. Fard and M. B. Shadmand, "Multi-timescale Three-tiered Voltage Control Framework for Dispersed Smart Inverters at the Grid Edge," *IEEE Transactions on Industry Applications*, 2021.
[60] M. B. Shadmand and R. S. Balog, "Design considerations for long-term remote photovoltaic-based power supply using non-planar photovoltaic surfaces," in *IEEE International Conference on Technologies for Homeland Security (HST)*, 2013.
[61] M. B. Shadmand and R. S. Balog, "Optimization of photovoltaic-wind hybrid system for apartment complexes and other community living environments by minimizing excess capacity," in *IEEE Photovoltaic Specialists Conference*, 2012.
[62] H. Beltran, E. Bilbao, E. Belenguer, I. Etxeberria-Otadui, and P. Rodriguez, "Evaluation of storage energy requirements for constant production in PV power plants," *IEEE transactions on industrial electronics*, vol. 60, no. 3, 2012.
[63] M. P. Raj and A. M. Joshua, "Modeling and performance analysis of perturb & observe, incremental conductance and fuzzy logic MPPT controllers," in *2017 International Conference on Advances in Electrical Technology for Green Energy (ICAETGT)*, 2017.
[64] Q. Xiao, H. Jia, B. Liang, and J. He, "Current balancing control for multi-port hybrid AC/DC microgrid," in *IEEE Power & Energy Society General Meeting*, 2017.
[65] H. A. Catherino, F. F. Feres, and F. Trinidad, "Sulfation in lead–acid batteries," *Journal of Power Sources*, vol. 129, no. 1, pp. 113-120, 2004.
[66] D. Wu, R. Todd, and A. J. Forsyth, "Adaptive rate-limit control for energy storage systems," *IEEE Transactions on Industrial Electronics*, vol. 62, no. 7, pp. 4231-4240, 2015.
[67] R. R. Jha, S. C. Srivastava, and M. Kumar, "Development of control schemes for a cluster of PV-integrated houses in islanded mode," *IET Renewable Power Generation*, vol. 11, no. 7, pp. 903-911, 2017.
[68] B. Mirafzal and A. Adib, "On grid-interactive smart inverters: Features and advancements," *IEEE Access*, vol. 8, pp. 160526-160536, 2020.
[69] A. Micallef, M. Apap, C. Spiteri-Staines, and J. M. Guerrero, "Single-phase microgrid with seamless transition capabilities between modes of operation," *IEEE Transactions on Smart Grid*, vol. 6, no. 6, pp. 2736-2745, 2015.
[70] T. L. Vandoorn, B. Meersman, J. D. De Kooning, and L. Vandevelde, "Transition from islanded to grid-connected mode of microgrids with voltage-based droop control," *IEEE transactions on power systems*, vol. 28, no. 3, pp. 2545-2553, 2013.
[71] D. G. Photovoltaics and E. Storage, "IEEE Application Guide for IEEE Std 1547™, IEEE Standard for Interconnecting Distributed Resources with Electric Power Systems," 2009.
[72] S. IEC 61727, "Photovoltaic (PV) systems characteristics of the utility interface," ed: ed, 2004.
[73] D. Ghotra, H. Nguyen, R. J. Morash, and K. W. Johnston, "Seamless transitions between control modes," ed: Google Patents, 2017.

[74] J. Rocabert, A. Luna, F. Blaabjerg, and P. Rodriguez, "Control of power converters in AC microgrids," *IEEE transactions on power electronics,* vol. 27, no. 11, pp. 4734-4749, 2012.
[75] D. S. Ochs, P. Sotoodeh, and B. Mirafzal, "A technique for voltage-source inverter seamless transitions between grid-connected and standalone modes," in *Twenty-Eighth Annual IEEE Applied Power Electronics Conference and Exposition (APEC)*, 2013, pp. 952-959.
[76] T.-V. Tran, T.-W. Chun, H.-H. Lee, H.-G. Kim, and E.-C. Nho, "PLL-based seamless transfer control between grid-connected and islanding modes in grid-connected inverters," *IEEE Transactions on Power Electronics,* vol. 29, no. 10, 2013.
[77] G. G. Talapur, H. M. Suryawanshi, L. Xu, and A. B. Shitole, "A reliable microgrid with seamless transition between grid connected and islanded mode for residential community with enhanced power quality," *IEEE Transactions on Industry Applications,* vol. 54, no. 5, 2018.
[78] Y. Okui, S. Ohta, N. Nakamura, H. Hirata, and M. Yanagisawa, "Development of line interactive type UPS using a novel control system," in *The 25th International Telecommunications Energy Conference, 2003. INTELEC'03.*, 2003, pp. 796-801.
[79] M. A. Abusara, J. M. Guerrero, and S. M. Sharkh, "Line-interactive UPS for microgrids," *IEEE Transactions on Industrial Electronics,* vol. 61, no. 3, pp. 1292-1300, 2013.
[80] Y. Deng, Y. Tao, G. Chen, G. Li, and X. He, "Enhanced power flow control for grid-connected droop-controlled inverters with improved stability," *IEEE Transactions on Industrial Electronics,* vol. 64, no. 7, 2016.
[81] J. Kim, J. M. Guerrero, P. Rodriguez, R. Teodorescu, and K. Nam, "Mode adaptive droop control with virtual output impedances for an inverter-based flexible AC microgrid," *IEEE Transactions on power electronics,* vol. 26, no. 3, 2010.
[82] Y. Jia, D. Liu, and J. Liu, "A novel seamless transfer method for a microgrid based on droop characteristic adjustment," in *Proc. International Power Electronics and Motion Control Conference*, 2012.
[83] M. Sinha, F. Dörfler, B. B. Johnson, and S. V. Dhople, "Uncovering droop control laws embedded within the nonlinear dynamics of van der pol oscillators," *IEEE Transactions on Control of Network Systems,* vol. 4, no. 2, 2015.
[84] F. Gao and M. R. Iravani, "A control strategy for a distributed generation unit in grid-connected and autonomous modes of operation," *IEEE Transactions on power delivery,* vol. 23, no. 2, 2008.
[85] R. Tirumala, N. Mohan, and C. Henze, "Seamless transfer of grid-connected PWM inverters between utility-interactive and stand-alone modes," in *APEC. Seventeenth Annual IEEE Applied Power Electronics Conference and Exposition*, 2002, vol. 2.
[86] M. A. P. de Azpeitia, A. Fernández, D. G. Lamar, M. Rodriguez, and M. M. Hernando, "Simplified voltage-sag filler for line-interactive uninterruptible power supplies," *IEEE Transactions on Industrial Electronics,* vol. 55, no. 8, pp. 3005-3011, 2008.
[87] H. Kim, T. Yu, and S. Choi, "Indirect current control algorithm for utility interactive inverters in distributed generation systems," *IEEE Transactions on Power Electronics,* vol. 23, no. 3, pp. 1342-1347, 2008.
[88] Y. Li, D. M. Vilathgamuwa, and P. C. Loh, "Design, analysis, and real-time testing of a controller for multibus microgrid system," *IEEE Transactions on power electronics,* vol. 19, no. 5, pp. 1195-1204, 2004.

[89] Q.-C. Zhong, P.-L. Nguyen, Z. Ma, and W. Sheng, "Self-synchronized synchronverters: Inverters without a dedicated synchronization unit," *IEEE Transactions on power electronics,* vol. 29, no. 2, pp. 617-630, 2013.
[90] M. Ramezani, S. Li, F. Musavi, and S. Golestan, "Seamless transition of synchronous inverters using synchronizing virtual torque and flux linkage," *IEEE Transactions on Industrial Electronics,* vol. 67, no. 1, pp. 319-328, 2019.
[91] J. M. Guerrero, J. C. Vasquez, J. Matas, M. Castilla, and L. G. de Vicuña, "Control strategy for flexible microgrid based on parallel line-interactive UPS systems," *IEEE Transactions on industrial Electronics,* vol. 56, no. 3, pp. 726-736, 2008.
[92] C. Cho, J.-H. Jeon, J.-Y. Kim, S. Kwon, K. Park, and S. Kim, "Active synchronizing control of a microgrid," *IEEE Transactions on Power Electronics,* vol. 26, no. 12, pp. 3707-3719, 2011.
[93] M. Ganjian-Aboukheili, M. Shahabi, Q. Shafiee, and J. M. Guerrero, "Seamless Transition of Microgrids Operation from Grid-Connected to Islanded Mode," *IEEE Transactions on Smart Grid,* 2019.
[94] M. B. Delghavi and A. Yazdani, "A unified control strategy for electronically interfaced distributed energy resources," *IEEE Transactions on Power Delivery,* vol. 27, no. 2, 2012.
[95] X. Li and R. S. Balog, "PLL-less robust active and reactive power controller for single phase grid-connected inverter with LCL filter," in *2015 IEEE Applied Power Electronics Conference and Exposition (APEC)*, 2015.
[96] Y. Yang, H. Wang, and F. Blaabjerg, "Reactive power injection strategies for single-phase photovoltaic systems considering grid requirements," *IEEE Transactions on Industry Applications,* vol. 50, no. 6, pp. 4065-4076, 2014.
[97] J. Shen and A. Khaligh, "A supervisory energy management control strategy in a battery/ultracapacitor hybrid energy storage system," *IEEE Transactions on Transportation Electrification,* vol. 1, no. 3, pp. 223-231, 2015.
[98] Y. Yang, Q. Ye, L. J. Tung, M. Greenleaf, and H. Li, "Integrated size and energy management design of battery storage to enhance grid integration of large-scale PV power plants," *IEEE Transactions on industrial electronics,* vol. 65, no. 1, pp. 394-402, 2017.
[99] B.-I. Crăciun, T. Kerekes, D. Séra, and R. Teodorescu, "Frequency support functions in large PV power plants with active power reserves," *IEEE Journal of Emerging and Selected Topics in Power Electronics,* vol. 2, no. 4, 2014.
[100] A. Hoke, E. Muljadi, and D. Maksimovic, "Real-time photovoltaic plant maximum power point estimation for use in grid frequency stabilization," in *IEEE 16th workshop on Control and Modeling for Power Electronics (COMPEL)*, 2015.
[101] C.-L. Nguyen, H.-H. Lee, and T.-W. Chun, "Cost-optimized battery capacity and short-term power dispatch control for wind farm," *IEEE Transactions on Industry Applications,* vol. 51, no. 1, pp. 595-606, 2014.
[102] A. Sangwongwanich, Y. Yang, and F. Blaabjerg, "High-performance constant power generation in grid-connected PV systems," *IEEE Transactions on Power Electronics,* vol. 31, no. 3, pp. 1822-1825, 2015.
[103] A. Sangwongwanich, Y. Yang, F. Blaabjerg, and D. Sera, "Delta power control strategy for multistring grid-connected PV inverters," *IEEE Transactions on Industry Applications,* vol. 53, no. 4, pp. 3862-3870, 2017.

[104] H. D. Tafti, A. Sangwongwanich, Y. Yang, J. Pou, G. Konstantinou, and F. Blaabjerg, "An adaptive control scheme for flexible power point tracking in photovoltaic systems," *IEEE Transactions on Power Electronics*, 2018.
[105] H. D. Tafti, A. I. Maswood, G. Konstantinou, J. Pou, and F. Blaabjerg, "A general constant power generation algorithm for photovoltaic systems," *IEEE Transactions on Power Electronics*, vol. 33, no. 5, pp. 4088-4101, 2017.
[106] A. Sangwongwanich, Y. Yang, and F. Blaabjerg, "A sensorless power reserve control strategy for two-stage grid-connected PV systems," *IEEE Transactions on Power Electronics*, vol. 32, no. 11, pp. 8559-8569, 2017.
[107] B.-I. Crăciun, T. Kerekes, D. Séra, R. Teodorescu, and U. D. Annakkage, "Power ramp limitation capabilities of large PV power plants with active power reserves," *IEEE Transactions on Sustainable Energy*, vol. 8, no. 2, pp. 573-581, 2016.
[108] V. Gevorgian and B. O'Neill, "Advanced grid-friendly controls demonstration project for utility-scale PV power plants," National Renewable Energy Lab.(NREL), Golden, CO (United States), 2016.
[109] H. D. Tafti, C. D. Townsend, G. Konstantinou, and J. Pou, "A multi-mode flexible power point tracking algorithm for photovoltaic power plants," *IEEE Transactions on Power Electronics*, vol. 34, no. 6, pp. 5038-5042, 2018.
[110] L. Bird, J. Cochran, and X. Wang, "Wind and solar energy curtailment: Experience and practices in the United States," National Renewable Energy Lab.(NREL), Golden, CO (United States), 2014.
[111] G. F. Law, "Renewable Energy Sources Act (Gesetz fur den Vorrang Erneuerbarer Energien)," *BGBl Std., Document No.: BGBl. I S*, vol. 1066, 2014.
[112] D. Energinet, "Technical regulation 3.2. 2 for PV power plants with a power output above 11 kW," *Energinet, Fredericia, Denmark, Tech. Rep*, 2015.
[113] N. Ahrens, P. Arni, S. Battles, S. Clò, P. Zoppoli, and E. Baum, "BDEW–Bundesverband der Energie-und Wasserwirtschaft eV (2012): Erneuerbare Energien und das EEG: Zahlen," *Fakten, Grafiken*.
[114] Y. Yang, H. Wang, F. Blaabjerg, and T. Kerekes, "A hybrid power control concept for PV inverters with reduced thermal loading," *IEEE Transactions on Power Electronics*, vol. 29, no. 12, 2014.
[115] Y. Yang, F. Blaabjerg, and H. Wang, "Constant power generation of photovoltaic systems considering the distributed grid capacity," in *IEEE Applied Power Electronics Conference and Exposition-APEC 2014*, 2014.
[116] A. Urtasun, P. Sanchis, and L. Marroyo, "Limiting the power generated by a photovoltaic system," in *10th International Multi-Conferences on Systems, Signals & Devices 2013 (SSD13)*, 2013.
[117] C. Rosa, D. Vinikov, E. Romero-Cadaval, V. Pires, and J. Martins, "Low-power home PV systems with MPPT and PC control modes," in *International Conference-Workshop Compatibility And Power Electronics*, 2013.
[118] A. Hoke and D. Maksimović, "Active power control of photovoltaic power systems," in *IEEE Conference on Technologies for Sustainability (SusTech)*, 2013.
[119] H. Xin, Z. Lu, Y. Liu, and D. Gan, "A center-free control strategy for the coordination of multiple photovoltaic generators," *IEEE Transactions on Smart Grid*, vol. 5, no. 3, pp. 1262-1269, 2014.

[120] A. Sangwongwanich, Y. Yang, and F. Blaabjerg, "Sensorless reserved power control strategy for two-stage grid-connected photovoltaic systems," in *IEEE 7th international symposium on power electronics for distributed generation systems (PEDG)*, 2016.
[121] E. I. Batzelis, S. A. Papathanassiou, and B. C. Pal, "PV system control to provide active power reserves under partial shading conditions," *IEEE Transactions on Power Electronics*, vol. 33, no. 11, pp. 9163-9175, 2018.
[122] E. I. Batzelis, G. E. Kampitsis, and S. A. Papathanassiou, "Power reserves control for PV systems with real-time MPP estimation via curve fitting," *IEEE Transactions on Sustainable Energy*, vol. 8, no. 3, pp. 1269-1280, 2017.
[123] X. Li, H. Wen, Y. Zhu, L. Jiang, Y. Hu, and W. Xiao, "A novel sensorless photovoltaic power reserve control with simple real-time MPP estimation," *IEEE Transactions on Power Electronics*, vol. 34, no. 8, pp. 7521-7531, 2018.
[124] S. Luo, "A review of distributed power systems part I: DC distributed power system," *IEEE Aerospace and Electronic Systems Magazine*, vol. 20, no. 8, 2005.
[125] A. Sangwongwanich, Y. Yang, and F. Blaabjerg, "A cost-effective power ramp-rate control strategy for single-phase two-stage grid-connected photovoltaic systems," in *2016 IEEE Energy Conversion Congress and Exposition (ECCE)*, 2016.
[126] Q. Peng, A. Sangwongwanich, Y. Yang, and F. Blaabjerg, "Grid-friendly power control for smart photovoltaic systems," *Solar Energy*, 2020.
[127] N. Kakimoto, H. Satoh, S. Takayama, and K. Nakamura, "Ramp-rate control of photovoltaic generator with electric double-layer capacitor," *IEEE Transactions on Energy Conversion*, vol. 24, no. 2, pp. 465-473, 2009.
[128] X. Chen, Y. Du, H. Wen, L. Jiang, and W. Xiao, "Forecasting-based power ramp-rate control strategies for utility-scale PV systems," *IEEE Transactions on Industrial Electronics*, vol. 66, no. 3, pp. 1862-1871, 2018.
[129] M. Alam, K. Muttaqi, and D. Sutanto, "A novel approach for ramp-rate control of solar PV using energy storage to mitigate output fluctuations caused by cloud passing," *IEEE Transactions on Energy Conversion*, vol. 29, no. 2, pp. 507-518, 2014.
[130] R. Shah, N. Mithulananthan, R. Bansal, and V. Ramachandaramurthy, "A review of key power system stability challenges for large-scale PV integration," *Renewable and Sustainable Energy Reviews*, vol. 41, pp. 1423-1436, 2015.
[131] Y. Du, D. D.-C. Lu, D. Cornforth, and G. James, "A study on the harmonic issues at CSIRO microgrid," in *IEEE Ninth International Conference on Power Electronics and Drive Systems*, 2011.
[132] E. Troester, "New German grid codes for connecting PV systems to the medium voltage power grid," in *2nd International workshop on concentrating photovoltaic power plants: optical design, production, grid connection*, 2009.
[133] V. Gevorgian and S. Booth, "Review of PREPA technical requirements for interconnecting wind and solar generation," National Renewable Energy Lab.(NREL), Golden, CO (United States), 2013.
[134] D. G. Photovoltaics and E. Storage, "IEEE Guide for Design, Operation, and Integration of Distributed Resource Island Systems with Electric Power Systems," 2011.
[135] K.-S. Tam, P. Kumar, and M. Foreman, "Enhancing the utilization of photovoltaic power generation by superconductive magnetic energy storage," *IEEE Transactions on Energy Conversion*, vol. 4, no. 3, pp. 314-321, 1989.

[136] S. Rahman and K.-s. Tam, "A feasibility study of photovoltaic-fuel cell hybrid energy system," *IEEE Transactions on Energy Conversion,* vol. 3, no. 1, pp. 50-55, 1988.
[137] J. Traube *et al.,* "Mitigation of solar irradiance intermittency in photovoltaic power systems with integrated electric-vehicle charging functionality," *IEEE Transactions on Power Electronics,* vol. 28, no. 6, pp. 3058-3067, 2012.
[138] C. Zhang, Y. Du, X. Chen, and D. D.-C. Lu, "Cloud motion tracking system using low-cost sky imager for PV power ramp-rate control," in *IEEE International Conference on Industrial Electronics for Sustainable Energy Systems (IESES)*, 2018.
[139] V. Fung, J. Bosch, S. Roberts, and J. Kleissl, "Cloud shadow speed sensor," *Atmospheric Measurement Techniques,* vol. 7, no. 6, pp. 1693-1700, 2014.
[140] M. Saleh, L. Meek, M. A. Masoum, and M. Abshar, "Battery-less short-term smoothing of photovoltaic generation using sky camera," *IEEE Transactions on Industrial Informatics,* vol. 14, no. 2, 2017.
[141] L. Hinkelman, R. George, S. Wilcox, and M. Sengupta, "Spatial and temporal variability of incoming solar irradiance at a measurement site in Hawaii," in *American Meteorological Society Annual Meeting*, 2011.
[142] N. Ina, S. Yanagawa, T. Kato, and Y. Suzuoki, "Smoothing of PV system output by tuning MPPT control," *Electrical Engineering in Japan,* vol. 152, no. 2, pp. 10-17, 2005.
[143] H. Chen, T. N. Cong, W. Yang, C. Tan, Y. Li, and Y. Ding, "Progress in electrical energy storage system: A critical review," *Progress in natural science*, vol. 19, no. 3, pp. 291-312, 2009.